Exploring instabilities of bad metals with optical spectroscopy

Tytarenko, A.

Publication date
2017
Document Version
Final published version
License
Other

Exploring instabilities of bad metals with optical spectroscopy

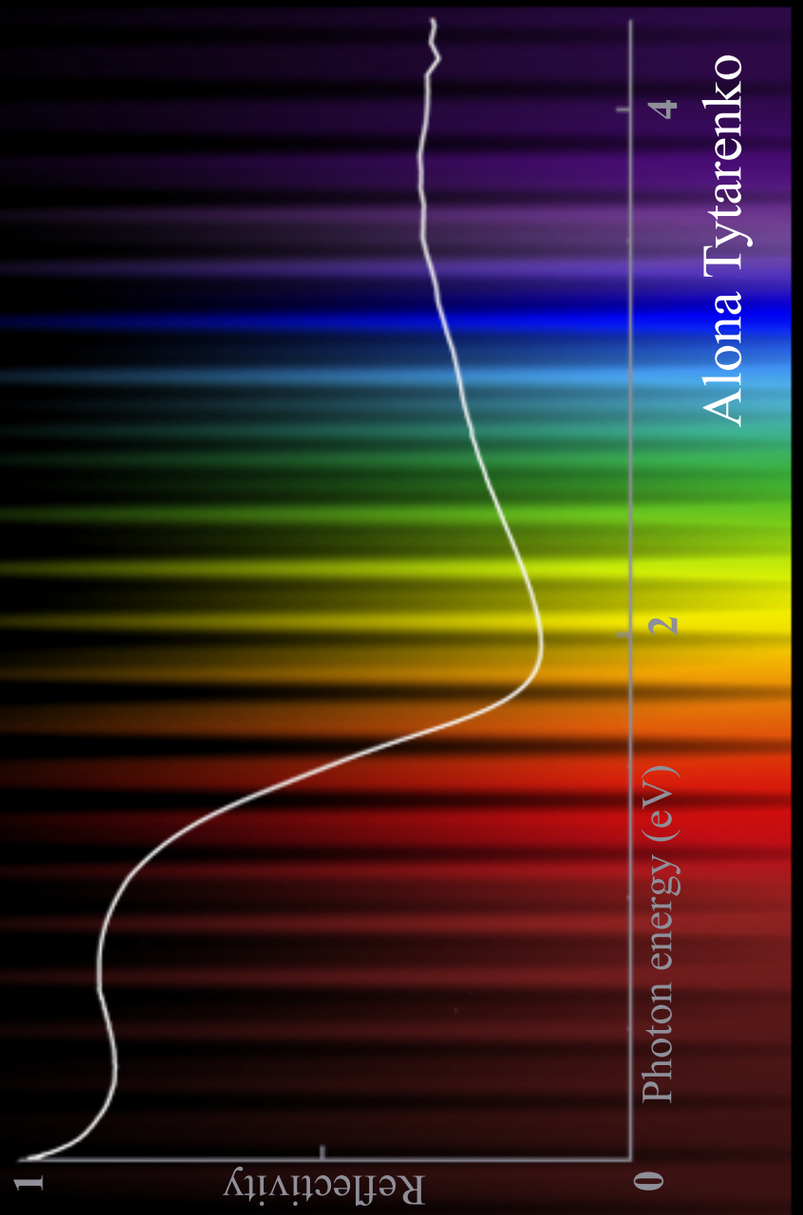

Exploring instabilities of bad metals with optical spectroscopy.

Alona Tytarenko

ISBN: 978-94-6233-798-5
Cover: Alone Tytarenko.

Exploring instabilities of bad metals with optical spectroscopy.

ACADEMISCH PROEFSCHRIFT

ter verkrijging van de graad van doctor
aan de Universiteit van Amsterdam
op gezag van de Rector Magnificus
prof. dr. ir. K.I.J. Maex
ten overstaan van een door het College voor Promoties ingestelde commissie,
in het openbaar te verdedigen in de Agnietenkapel
op dinsdag 28 november 2017, te 10.00 uur

door

Alona Tytarenko

geboren te Kiev, Oekraïne

Promotiecommissie:

Promotor:	Prof. Dr. M.S. Golden, Universiteit van Amsterdam
Copromotor:	Dr. E. van Heumen, Universiteit van Amsterdam
Overige leden:	Prof. Dr. D. Bonn, Universiteit van Amsterdam
	Prof. Dr. F.E. Schreck, Universiteit van Amsterdam
	Prof. Dr. B. Büchner, Technische Universität Dresden
	Prof. Dr. P. Rudolf, Rijksuniversiteit Groningen
	Dr. A. de Visser, Universiteit van Amsterdam
	Dr. S. Johnston, University of Tennessee

Faculteit der Natuurwetenschappen, Wiskunde en Informatica

The research reported in this thesis was performed in the Quantum Matter group at the Van der Waals – Zeeman Institute, part of the Institute of Physics, University of Amsterdam.

Exploring instabilities of bad metals with optical spectroscopy.

What happens when a near infinity of electrons is confined to a periodic potential, interacting with each other under the influence of the Coulomb interaction? This question has captivated generations of condensed matter physicists, from both the experimental and theoretical persuasion, and the answer appears to be 'unpredictable'. In the past century, the condensed matter community has discovered that many different 'ordered' states can emerge out of the quantum soup made from interacting electrons.

Famous examples of such ordered quantum states are magnets and superconductors. Magnets are probably most easily imagined by the human mind and are microscopically often represented as a pattern of small magnets, all lined up periodically in space. Quantum mechanically, this description is already not completely correct as the 'ordering' often really takes place in momentum space. In non-magnetic metals there is an equal fraction of electrons with spin-up and spin-down. In magnets such as iron, a small fraction of the electrons preferentially occupy momentum states with one particular spin direction under the influence of the Coulomb repulsion. This results in a net magnetic moment for the crystal as a whole, but the key point is that the electrons are in fact completely delocalized over the entire crystal. The order of a superconductor is even more difficult to describe. In this case the electrons form so-called Cooper pairs (bound states of two electrons) and the ordering takes place in the quantum mechanical phase of the macroscopic wavefunction describing the whole ensemble of Cooper pairs.

In the first decade of the twenty-first century we have witnessed a remarkable turn in our understanding of 'order' and have possibly found a new method to classify electronic states of matter in general. Borrowing concepts from the mathematical theory of topology (a framework to describe knots and twists using the abstract language of mathematics), we have learned that macroscopic wavefunctions can be distinguished using so-called topological invariants. In this language, variations of ordered states are distinguished by different values of such invariants. The most famous example of this is the quantum Hall state, where abrupt changes in the topological invariant with magnetic field result in sudden jumps in the conductivity.

The importance of topological order and the role it plays in the formation of new ground states of interacting electron systems is not exactly known, but is an active topic of research and underlies the research presented in this thesis. In the past four years, I have used optical spectroscopy to investigate two classes of materials that display phase changes as function of temperature. Chapter 4 describes the optical properties of Co-doped $BaFe_2As_2$, a member of a family of high temperature superconductors, known as the iron-pnictide high T_c's, while chapter 5 concerns the correlated, and possibly topological, Kondo insulator: SmB_6.

The (low temperature) groundstate of these two materials is completely different, but at high temperature they are in some sense similar: both materials feature a strongly temperature and frequency dependent optical response that has become known as a 'bad metal'. In 'clean' metals one would expect a so-called Drude response for the optical conductivity at low energy. The Drude response can be characterized by a frequency and temperature independent scattering rate; an average time between collisions that does not depend on temperature, indicating that the electrons behave as a gas of freely moving particles. Instead, bad metals feature a strong temperature and frequency dependent scattering rate indicative of residual interactions between the electrons. In such materials, a careful analysis of the optical response not only provides fingerprints of the interactions responsible for the bad metal behavior, but also of the key driving forces behind the instabilities that lead to the ordered electronic states at low temperature.

In this thesis I discuss how optical spectroscopy (Chapter 2) can be effectively used (Chapter 3) in the study of instabilities of interacting electron systems. For the study of the iron-pnictides (Chapter 4), I developed a new method to visualize the complex optical response of the normal state. This allows me to demonstrate that the metallic state is in fact very close to being a Fermi liquid. In the final chapter (Chapter 5), I discuss a careful reexamination of the changes that take place in the optical response of SmB_6 as it changes from a bad metal to a Kondo insulator. This analysis provides new evidence that the Kondo insulating state is formed under the influence of the Coulomb interaction and that the Kondo state is therefore adiabatically connected to a simple hybridized band insulator.

Exploring instabilities of bad metals with optical spectroscopy.

Wat gebeurt er als een praktisch oneindig aantal, met elkaar wisselwerkende elektronen opgesloten wordt in een periodieke potentiaal? Deze vraag heeft generaties experimenteel en theoretisch georiënteerde vaste stof fysici gefascineerd en het antwoord lijkt 'onvoorspelbaar' te zijn. In de afgelopen eeuw heeft de gecondenseerde materie gemeenschap ontdekt dat vele verschillende 'geordende' toestanden kunnen ontstaan uit een quantum soep getrokken uit wisselwerkende electronen.

Beroemde voorbeelden van zulke geordende toestanden zijn magneten en supergeleiders. Magneten spreken waarschijnlijk het meest gemakkelijk tot de verbeelding en worden op microscopische schaal vaak voorgesteld als een patroon van kleine magneetjes die allemaal dezelfde richting op wijzen. Quantum mechanisch gaat deze beschrijving al vrij snel mank, aangezien de orde meestal in de impuls ruimte plaatsvindt. In niet-magnetische metalen is het aantal elektronen met spin omhoog in balans met het aantal elektronen met spin omlaag, waardoor er geen netto magnetisatie is. In bekende magnetische materialen, zoals ijzer, ontstaat onder invloed van de Coulomb wisselwerking een kleine onbalans in bezetting van impuls toestanden waardoor een netto magnetisatie optreedt. Een belangrijk punt hierbij is dat deze elektronen zich in quantum toestanden bevinden die volledig uitgesmeerd zijn over het kristal en dat er dus geen sprake is van kleine 'lokale' magneetjes. De orde waaraan supergeleiders onderhevig zijn laat zich nog moeilijker beschrijven. In dit geval vormen de elektronen zogenoemde Cooper paren (gebonden toestanden van twee elektronen) en treedt de orde op in de quantum mechanische fase van de macroscopische golffunctie die het hele ensemble van deze Cooper paren beschrijft.

In het eerste decennium van de eenentwintigste eeuw hebben we een belangrijke omkeer meegemaakt in ons begrip van 'orde' en wellicht een manier ontdekt om elektronische toestanden in het algemeen te classificeren. Met concepten geleend uit de mathematische theorie van de topologie (een raamwerk dat knopen en wendingen beschrijft in de abstracte taal van de wiskunde) hebben we geleerd dat macroscopische golffuncties onderscheiden kunnen worden met behulp van zogeheten topologische invarianten. In

deze taal reflecteren variaties in de orde van elektronische toestanden zich door discrete veranderingen in de waarden van de topologische invarianten. Een beroemd voorbeeld hiervan is de quantum Hall toestand, waarin abrupte variaties van de topologische invarianten als functie van aangelegd magnetisch veld zich manifesteren in plotselinge sprongen in de geleiding.

Hoe belangrijk topologische orde is en de rol die het speelt in de formatie van nieuwe grondtoestanden van wisselwerkende elektronen systemen is niet precies bekend, maar het is een actief nieuw onderzoeksgebied en vormt de basis voor het werk beschreven in dit proefschrift. In de afgelopen vier jaar heb ik met behulp van optische spectroscopie twee klassen van materialen onderzocht waarin fase veranderingen als functie van temperatuur plaats vinden. Hoofdstuk 4 beschrijft de optische eigenschappen van Co gedoteerd $BaFe_2As_2$, een lid van een familie van hoge temperatuur supergeleiders die bekend staan als de ijzer-pnictiden, terwijl hoofdstuk 5 de gecorreleerde, en mogelijk topologische, Kondo isolator SmB_6 behandelt.

De (lage temperatuur) grondtoestand van beide materialen is compleet verschillend, maar bij hoge temperatuur vertonen ze overeenkomsten. In beide gevallen is de optische respons sterk temperatuur en frequentie afhankelijk; een effect dat bekend is komen te staan als karakteristiek voor een 'slecht' metaal. In 'schone' metalen zou men bij lage frequenties een zogeheten Drude response verwachten in de optische geleiding. The Drude response wordt gekarakteriseerd door een frequentie en temperatuur onafhankelijke verstrooïngs-tijd; een vaste, gemiddelde verstrooings-tijd die niet van temperatuur afhangt is een teken dat de elektronen zich als een gas van vrije elektronen gedragen. Slechte metalen daarentegen laten vaak een verstrooïngs-tijd zien die sterk van energie en temperatuur afhangt en dit duidt op wisselwerkingen tussen de elektronen. In dit soort materialen leidt een nauwkeurige analyse van de optische eigenschappen niet alleen tot de vingerafdrukken van de wisselwerkingen tussen de elektronen, maar ook tot een beter begrip van de drijvende krachten achter de instabiliteiten die leiden tot de geordende toestanden bij lage temperatuur.

In dit proefschrift laat ik zien hoe optische spectroscopie (Hoofdstuk 2) effectief gebruikt kan worden (Hoofdstuk 3) in de studie van instabiliteiten van wisselwerkende elektronen systemen. Voor de studie van de ijzer-pnictiden (Hoofdstuk 4) heb ik een nieuwe manier ontwikkeld om de complexe optische response van de normale toestand weer te geven. Dit stelt mij in staat om te laten zien dat de normale toestand in feite heel veel weg heeft van een Fermi vloeistof toestand. In het laatste hoofdstuk (Hoofdstuk 5) geef ik een gedetailleerde beschrijving van de temperatuur afhankelijke veranderingen in de optische response van SmB_6, die plaats vinden in de overgang van slecht metaal naar Kondo isolator. Deze analyse laat zien dat de Kondo toestand gevormd wordt onder invloed van de Coulomb wisselwerking en dat de Kondo toestand dien ten gevolge gezien moet worden als een adiabatsch gerelateerde versie van een band isolator.

Contents

List of Figures

Chapter 1

Introduction

1.1 Bad metals and their instabilities.

The physics of strongly correlated systems is one of the most prominent areas of condensed matter physics. It deals with materials where the total kinetic energy (or bandwidth) of the relevant electronic degrees of freedom is smaller than the Coulomb interaction. As a result, the latter plays an intricate role in defining the macroscopic properties of the system. This is believed to be the source for the exotic properties of heavy-fermion compounds, Kondo insulators, high-T_c superconductors and many of the transition metal oxide materials. The difficulty presented by these materials rests in the lack of a complete theoretical framework to describe and understand their behavior, while at the same time they continue to surprise us with novel electronic states that could potentially be relevant for applications. This makes the field of strongly correlated electron physics of fundamental importance and at the same time challenging and exciting.

In this thesis, the focus is on the iron-pnictide high-T_c superconductor $BaFe_{2-x}$ Co_xAs_2 (BFCO) and the proposed topological Kondo insulator SmB_6. Fig. 1.1 summarizes some of the similarities and differences between the two materials. As indicated, the high temperature electronic state of these materials is a so-called "bad metal" state; a seemingly normal metal where correlation effects are mostly washed out by thermal fluctuations and only an enhanced resistivity remains. However, for a material to be called a bad metal one needs more than just an enhanced resistivity. The resistivity itself is determined by the carrier density and the scattering rate (or equivalently the mean free path length). Bad metals are characterized by a mean free path length that apparently becomes smaller than the smallest typical length scales in the crystal, e.g. the lattice spacing. This characterization does not provide a rigorous condition, but it

	Unconventional SC $BaFe_{2-x}Co_xAs_2$	Kondo insulator SmB_6
	• Are of fundamental interest. • "Bad metal" at high temperature.	
Role played by correlations	Interaction between different Fermi surface sheets results in various types of electronic order	Itinerant *d*-electrons interact more strongly through indirect exchange interaction via *f*-electrons
Key changes in electronic properties	Transition from bad metal to superconductor, anti-ferromagnet or nematically ordered state	Transition from bad metal to topological Kondo insulator
Relevant degrees of freedom	Mostly Fe 3*d* orbitals; possibly A*s* 4*p* orbitals.	Sm 5*d* and 4*f* orbitals
Open questions	• Is the electron-electron interaction responsible for the superconducting instability? • Is the metallic state a correlated "bad metal"?	• Are there topological surface states in the Kondo gap? • Is the Coulomb interaction involved in the formation of the Kondo groundstate?
Link to:	• High-T_c cuprate superconductors • Heavy-fermion superconductors	• Heavy fermion compounds • Topological insulators • Dirac semimetals

FIGURE 1.1: Comparison between some of the relevant features of the two materials studied in this thesis.

does result in a generally accepted criterion for a material to be called a bad metal. This criterion is known as the Mott-Ioffe-Regel condition [1, 2]. In most metals the resistivity will increase with temperature and eventually saturate when the mean-free path becomes of order of the lattice spacing. However, in the correlated materials considered in this thesis, the mean-free path seemingly becomes smaller than the lattice spacing, signaling a breakdown of the free electron picture. The bad metal state is therefore intimately tied to enhanced electron-electron correlations. Although the resistivity is often used as a clear signature of the bad metallic state, spectroscopic techniques provide much more insight in the origins of correlation effects. For example, the breakdown of the free electron picture is accompanied by energy (or frequency) dependent renormalizations of the electronic structure of the material that can be directly observed with optical spectroscopy, angle resolved photoemission spectroscopy (ARPES) or scanning tunneling spectroscopy (STS).

In optical spectroscopy, correlation effects display themselves as changes in the frequency dependence of the free charge response. For free electrons one expects a so-called Drude peak in the optical conductivitywith a ω^{-2} dependence, while this exponent can be significantly different for correlated materials. At higher energy it is also possible to observe new structures or backgrounds [3] in the optical response, although it is not always clear how such features can be disentangled from the 'normal' interband transitions that can also be present. These spectroscopic probes allow us to more clearly compare the role played by correlations in BFCO and SmB_6, as listed in Fig. 1.1. For example, in

BFCO one observes a somewhat narrower bandwidth in ARPES as compared to the one predicted by DFT calculations. One expects this to be a consequence of additional correlation effects that are not captured in the current approximations to band theory. The effects of interactions on the optical response will be discussed in more detail in chapter 3.

Although both BFCO and SmB_6 are bad metals at elevated temperatures (and therefore in some sense similar), their low temperature groundstates are fundamentally different. This points to a sensitivity of the bad metallic state to the nature of the electronic states that dominate near the Fermi level. As indicated in Fig. 1.1, the relevant electronic degrees of freedom for SmB_6 are derived from the Sm $5d$ and $4f$ orbitals [4], while for BFCO they derive mostly from the Fe $3d$ orbitals [5], with the As $4p$ orbitals playing a minor role. As temperature is decreased, thermal fluctuations diminish and quantum fluctuations take over. In this low temperature regime the effects of correlations become more prominent, eventually resulting in an instability of the bad metal state. The new order that forms is however completely different for the two materials studied in this thesis: in BFCO a phase transition to an ordered electronic state takes place, while in SmB_6 a crossover to a correlated Kondo insulating phase takes place. As will be discussed in chapter 4, the nature of the low temperature phase in the iron-pnictides sensitively depends on the filling of the Fe $3d$ orbitals and can change from anti-ferromagnetic to superconducting order or even a previously unknown (and currently not completely understood) order dubbed "nematic order". The Kondo insulating state that forms in SmB_6 is theoretically much better understood. The spectacular new feature here is the prediction of so-called topological surface states that are expected to appear in the gap that opens when the d- and f-bands hybridize. As will be discussed in chapter 5, there are contradicting reports on whether these states have been observed.

In this thesis I will use optical spectroscopy as an experimental tool to answer some of the open questions indicated in Fig. 1.1. The advantage of this technique over other spectroscopies is its bulk sensitivity and its very high spectral resolution. Moreover, optical spectroscopy is a powerful tool that can be used to obtain a global overview of the electronic structure, but also provides access to the charge dynamics. This latter aspect provides the window on the impact of correlations on the electronic structure. The optical conductivity or, equivalently, the dielectric function serves as a good platform from which one can test theoretical models. A crucial aspect that sets the work presented in this thesis apart from other optical groups is that our experimental setup allows us to perform optical measurements not only with high frequency resolution, but also an equivalent resolution in temperature.

In the study of the iron-pnictide related in this thesis I will mainly focus on the properties of the normal state. The interactions responsible for the instability of the bad metal phase are perhaps more easily studied starting from the framework of an interacting Fermi liquid. In chapter 4 I will show that an analysis of the optical conductivity, measured on carefully annealed single crystals, clearly demonstrates deviations from the Drude law expected for non-interacting electrons. The usual "extended Drude" model that is used to establish these deviations cannot be used in complicated multiband systems [6, 7] and I will therefore introduce a new method to demonstrate these deviations. The method relies on the high temperature resolution available in our experiments and enables me to compare directly to calculations of the optical conductivity where electron-electron interactions are taken into account.

Despite the fact that SmB_6 has been thoroughly investigated in the past (see Chapter 5 for a detailed discussion), the recent improvements in crystal quality have motivated new optical measurements. Using a high-quality crystal combined with our high frequency and temperature resolution, our optical measurements provides new insight into the formation of the Kondo insulating state. Our optical data provide clear signatures of the mixed valence nature of this material. More importantly, I will present a detailed analysis of the optical spectral weight and will show that the spectral weight lost at low energy due to the opening of the hybridization gap, is not recovered over the entire energy range of our optical data. This is an indication that the formation of the Kondo state is accompanied by a reshuffling of the electronic structure over an energy range comparable to the Coulomb interaction, confirming an old idea that SmB_6 can be understood as a strongly correlated cousin of a band insulator [8].

1.2 Scope of this thesis

- Chapter 2 describes some aspects of the experimental techniques used. I start with a description of the experimental setup and provide a brief explanation of the physical principles underlying Fourier transform spectroscopy. I will also describe some of the key components of the cryostat, the sample preparation and I will provide a detailed description of the experimental procedures used. I will conclude with a brief discussion of how the optical response functions (e.g. the conductivity or dielectric function) are related to measured quantities (i.e. the reflectivity) and I will explain the methodology of the data analysis.

- Chapter 3 presents a general theoretical description of the optical properties of solids. I will first briefly discuss the "classical" Drude-Lorentz model, followed by a quantum mechanical interpretation of the optical processes in a material. Since

response functions are intimately tied to excitations starting from the groundstate, electronic band structure, I will briefly discuss the basis for density functional theory and how it determines the optical response of a solid. I will then provide a general introduction to the relatively new field of topological order and conclude with a brief discussion of the signatures of electron-electron correlations in optical response functions.

- Chapter 4 describes my results on the iron-pnictide superconductor BFCO. After a limited overview of some general features of iron-pnictide superconductivity, I will discuss how the optical conductivity demonstrates that the normal state can be characterized as approximately Fermi liquid. The original results presented in this chapter were published in Ref.[9].

- Chapter 5 describes the experiments performed on the Kondo insulator SmB_6. Here I will describe the theory of the many-body Kondo insulating state and how topological states emerge in the Kondo gap. I will subsequently discuss some of the experimental results related to the possible observation of topological surface states. This will be followed by a detailed discussion of the frequency and temperature dependence of the optical response. I will describe in detail the changes that take place as the Kondo insulating state is formed and will demonstrate how the Coulomb interaction is involved in these changes. The results presented in this chapter were published in Ref.[10].

Chapter 2

Nuts and bolts of optical spectroscopy.

The experiments presented in this thesis were performed using a Bruker VERTEX 80V, Fourier transform infrared (FTIR) spectrometer. In this chapter, I will first describe the basic components of the FTIR spectrometer (section 2.1), followed by a description of the physical principles by which the spectrometer works (section 2.2). Section 2.3 contains a description of the construction of the cryostat. In section 2.4 the procedure for sample preparation is described. The key steps for a typical experiment is presented in section 2.5. The last section, 2.6, discusses globally the steps in the data analysis which were used in this thesis.

2.1 Components of the Bruker VERTEX 80V spectrometer

A schematic of the FTIR spectrometer is shown in figure 2.1. The spectrometer covers the electromagnetic spectrum from the far-infrared (2 meV) up to the ultraviolet (5 eV). In this thesis, I will refer to the units wavenumbers (ω in [cm^{-1}]) or photon energy ($\hbar\omega$ in [eV]), which can be converted from one to another using the conversion factor: 1 eV = 8065 cm^{-1}. In the following I will briefly describe the individual components indicated in Fig. 2.1.

Light sources
To enable the reflectivity to be measured across the entire range from far-infrared (FIR) to ultraviolet (UV), the spectrometer includes different light sources. These are: Hg-arc

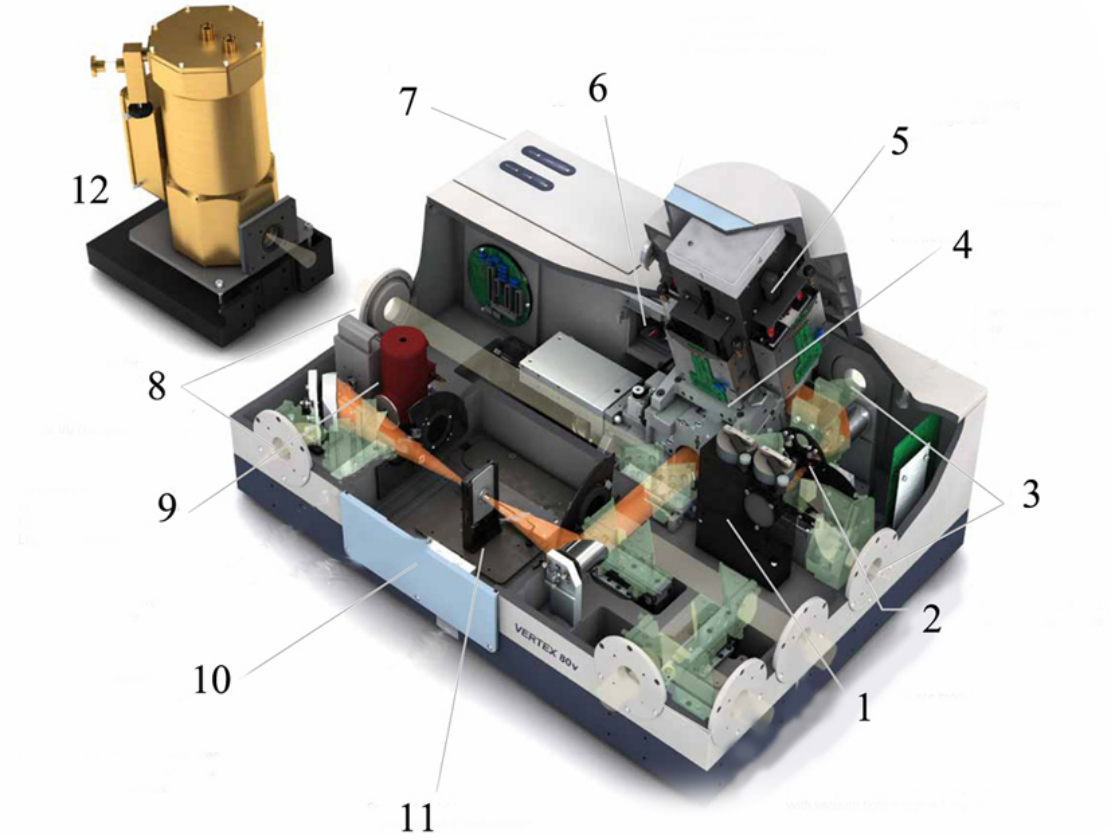

FIGURE 2.1: 1 - Internal source, 2 - the aperture wheel, 3 - external ports for light beam, 4 - interferometer, 5 - automatic beamsplitter changer, 6 - HeNe laser, 7 - electronics compartment, 8 - possible positions for liquid He cooled bolometer, 9 - detector compartment, 10 - removable compartment (position for the connection to the cryostat), 11 - sample position for transmitting measurement, 12 - the liquid He cooled bolometer (picture adapted from the Bruker manual [11]).

(FIR), a Globar source for the mid-infrared (MIR) energy range, tungsten for the near-infrared (NIR) and the visible (VIS) photon energy ranges and a deuterium source for the UV photon energy ranges. All light sources are unpolarized and non-coherent and produce a spectrum of photon frequencies. The light sources are indicated in Fig. 2.1 with label 1 and 3.

Beamsplitters

Each beamsplitter is optimized for a specific photon energy range. Four beamsplitters are used and listed below together with an indication of the spectral range in which they can be used:

- A $50\mu m$ Mylar is used in the FIR region from 3 meV to 10 meV. Mylar is a trademark for a polyethylene terephthalate (PET) film and for this beamspitter its thickness is 50μm.

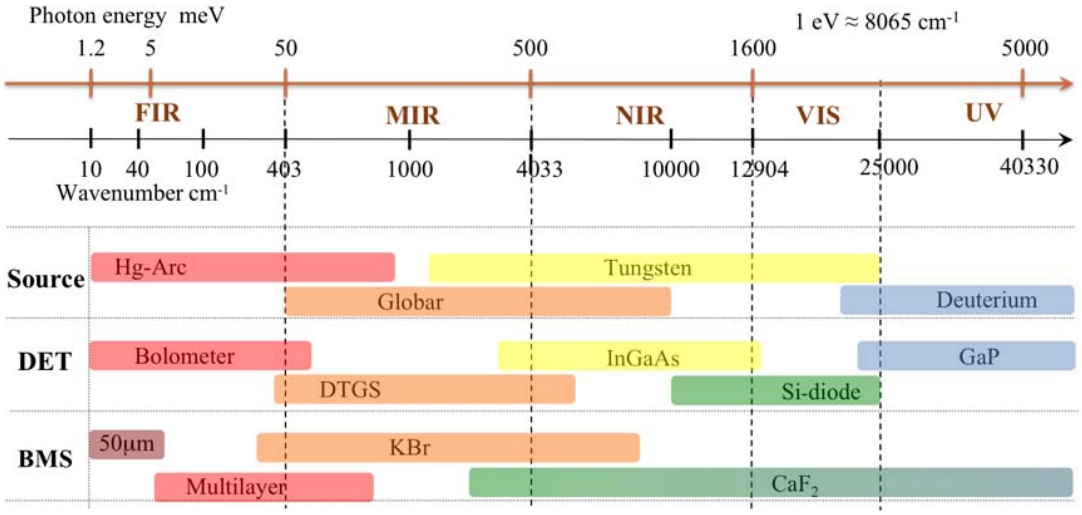

FIGURE 2.2: Table with the combination of light source, beamsplitter (BMS) and detector (DET).

- A polymer-based multilayer made from a 6μm Mylar layer supporting a Ge metal thin film is used in the FIR region from 6 meV to 80 meV.
- A KBr beamsplitter is used in the 50 meV - 800 meV spectral range.
- A CaF_2 beamsplitter is suitable for 300 meV - 5 eV, thus is used for the NIR, VIS, UV regions.

Detectors

For the FIR region, a bolometer is used to measure the infrared radiation. The bolometer is labelled as (12) in Fig. 2.1. It consists of a thermistor (detection element), which is cooled to liquid He temperatures, in order to increase its sensitivity. Incoming thermal radiation changes the temperature, which causes a change of the thermistor resistance. The resistance of the thermistor is amplified and measured as a voltage difference. The bolometer consists of two thermistors and two cut-on type filters. One filter cuts the incoming light at 800 cm^{-1} and another at 100 cm^{-1}.

A DLaTGS (Deuterated Lanthanum TriGlycine Sulphate) detector is used for measurements in the MIR energy range. The detector element is a pyroelectric crystal, which responds to temperature changes in the form of an alteration of its electrical polarization, which is measured as a voltage change by electric contacts placed on the detector element surface. The major disadvantage of the DLaTGS detector is that it is less sensitive than the other detector types covering different energy regions.

InGaAs and mercury cadmium telluride (MCT) detectors are used for the experiments in the NIR energy range. The major advantage of this detector type is higher sensitivity.

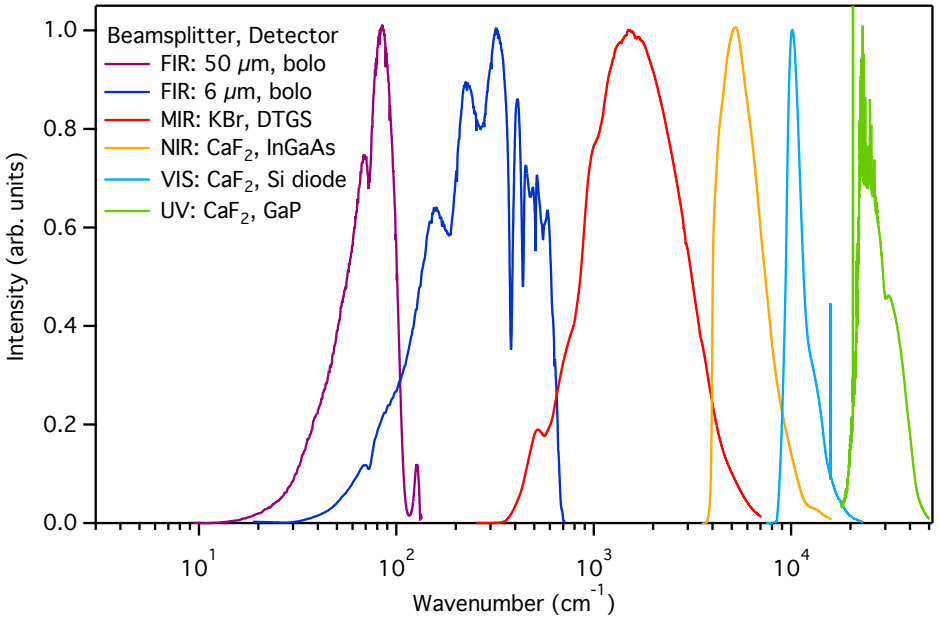

FIGURE 2.3: Black body spectra for the different energy regions measured with various detectors and beam splitters. All spectra are normalized to unity for ease of comparison.

The MCT detector must be cooled to low temperatures with liquid nitrogen and the coolant has to be refilled every eight hours.

In the visible and UV energy ranges, silicon and GaP diodes are used to detect the signal. These detectors (including the InGaAs and the MCT detectors described above) are of the semiconductor type. The working principle of these detectors relies on the excitation of electron - hole pairs from the valence band to the conduction band following absorption of the incoming radiation. Absorbed radiation produces electron-hole pairs, whose number is proportional to the radiation intensity. Excited electrons travel to the electrodes resulting in a pulse that is measured in an outer circuit.

In Fig. 2.2 all possible combinations of light sources, beamsplitters and detectors are summarized with respect to the energy range where they are used.

Computer

The spectrometer has a fast analogue to digital converter (ADC) which sends digitized detector output to the computer. This output is then processed using OPUS, a software package supplied together with the Bruker VERTEX 80V spectrometer. This software allows the user to control the spectrometer parameters, calculate the Fourier transform of the signal and store the data. The final spectrum $I(\omega)$ is then presented for interpretation and further analysis as described in section 2.5.

Apertures
The spectrometer includes an aperture wheel with 12 positions. The aperture can be chosen from 0.25 to 8 mm so that the light spot can be adapted to the sample size.

Other aspects of the spectrometer include a vacuum system (3 mbar), necessary to record spectra free from the absorption lines of atmospheric water vapor (with absorption bands between 1350 - 1850 cm^{-1} and 3400 - 3900 cm^{-1}) and carbon dioxide (667 cm^{-1} and 2350 cm^{-1}). The vacuum environment is also important for some optical elements. For example, the KBr beamsplitter is hygroscopic, meaning that it easily reacts with water from the atmosphere. Over time the oxidized layer will start to absorb part of the incoming light [12] and this process is slowed down significantly in vacuum.

To find optimal setup parameters for the detector/beamsplitter combination, test measurements were performed for each photon energy range. For this purpose, an evaporated film (Au or Al) was used as a test sample. Figure 2.3 depicts normalized spectra for all frequency ranges with the intensity normalized to unity. Figure 2.3 shows the spectral overlap of the different beamsplitter/detector combinations, which allows the user to accurately stitch together different reflectivity measurements into a single reflectivity spectrum over the entire range.

2.2 The Fourier transform spectrometer

The Bruker spectrometer is basically a Michelson interferometer. A schematic diagram of such an interferometer is shown in Fig. 2.4. The central element of the Michelson interferometer is a semi-reflecting beamsplitter (2), which divides an incident light beam (1) into reflected and transmitted beams of approximately equal intensity. One beam hits a mirror (M_1) which has a fixed position, while the other beam hits a movable mirror (M_2). The distance between the beamsplitter and mirror (d_1 and d_2) is referred to as an arm length of the interferometer. The beams reflect back from the mirrors and recombine again on the beamsplitter and then follow the same path to the sample (3) and to the detector (4) [12].

2.2.1 Monochromatic light source

The derivation in this section is taken from the book of Tkachenko [13] (Eq. (2.1)-Eq. (2.5)) and the notes by Homes [14] (Eq. (2.6)-Eq. (2.12)). To understand the principle behind FTIR spectroscopy, we first show how the output intensity of the interferometer can be found. This intensity is proportional to the square of the electric field

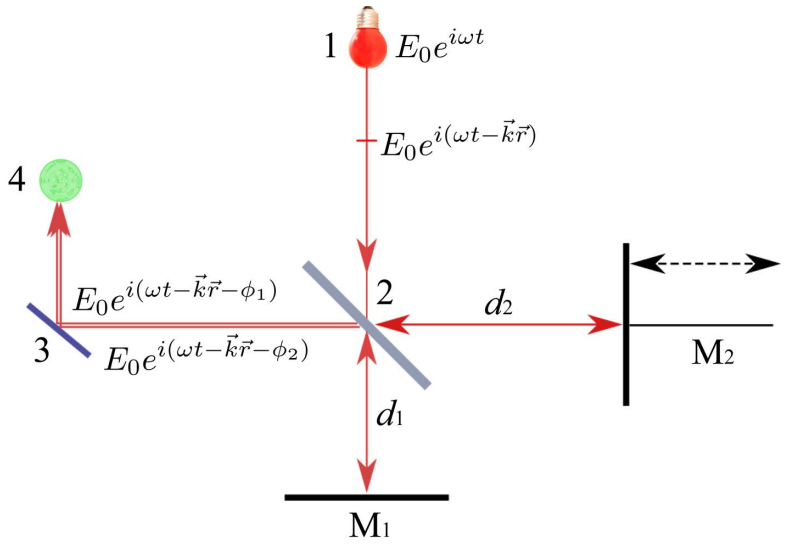

FIGURE 2.4: Schematic layout of a Michelson interferometer that forms the heart of a FTIR spectrometer. 1 - light source, 2 - beamsplitter, 3 - sample position, 4 - detector position, M_1 - fixed mirror, M_2 - movable mirror, d_1 and d_2 - arms of the interferometer.

generated by two light beams reflected from the mirrors M_1 and M_2 (see Fig. 2.4). The incoming monochromatic electromagnetic wave has an angular frequency ω or wavenumber $\vec{k}$, where $|\vec{k}| = \frac{2\pi}{\lambda} = \frac{\omega}{c}$, where λ is the wavelength and c is the speed of light. The beamsplitter divides incident light in two beams in the ideal case with equivalent intensity. Considering that both light beams are following the same direction to the detector, the electric fields of each of these beams can be written as [13]:

$$\vec{E}_1 = \vec{E}_0(\omega)e^{i(\omega t-\vec{k}\cdot\vec{r}-\phi_1)} \tag{2.1}$$

$$\vec{E}_2 = \vec{E}_0(\omega)e^{i(\omega t-\vec{k}\cdot\vec{r}-\phi_2)} \tag{2.2}$$

where E_0 is the amplitude of the electric field, ϕ_1 and ϕ_2 are the phases, that depend on the propagation distance between the beamsplitter and the two mirrors. The phases can be written as $\phi_1 = \vec{k}d_1 = 2\pi d_1/\lambda$ and $\phi_2 = \vec{k}d_2 = 2\pi d_2/\lambda$, where d_1 and d_2 are distances from the beamsplitter to the mirrors. After recombination of the two light beams, the amplitude of the interferometer output can be expressed as:

$$\vec{E} = \vec{E}_1 + \vec{E}_2 = \vec{E}_0(\omega)e^{i(\omega t-\vec{k}\cdot\vec{r})}(e^{-i2\pi d_1/\lambda} + e^{-i2\pi d_2/\lambda}) \tag{2.3}$$

The light intensity is proportional to $E \cdot E^*$, where E^* is the complex conjugate. Thus, the resulting intensity at the position of the detector is:

$$I = 2I(\omega)\left(1 + \cos\frac{2\pi(d_1 - d_2)}{\lambda}\right) \tag{2.4}$$

where $I(\omega)$ is proportional to $E_0^2(\omega)$ and $(d_1 - d_2)$ is called the optical path difference (OPD).

By putting $x = (d_1 - d_2)$ the detector output takes the form:

$$I(x) = 2I(\omega)[1 + \cos(2\pi x/\lambda)] \qquad (2.5)$$

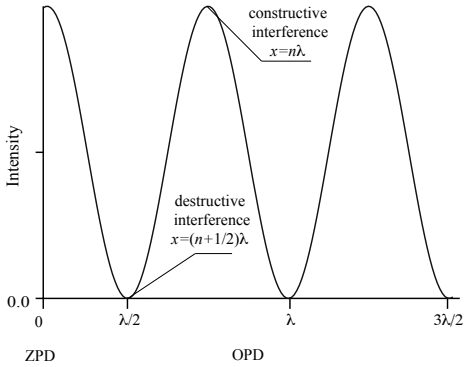

FIGURE 2.5: Interferogram of a monochromatic wave. ZPD stands for zero path difference, while OPD stands for optical path difference. At ZPD the two arms of the interferometer are of equal length. As the length of the arms is changed a periodic oscillation of the output intensity results from destructive and constructive interference. Figure adapted from [12].

At zero optical path difference, one has a maximum in intensity resulting from constructive interference. As the mirror M_2 starts to move, a phase difference develops between the two arms and the intensity is reduced. When the optical path difference reaches $x = \lambda/2$ the intensity reaches a minimum. As the mirror moves beyond $x = \lambda/2$ the intensity increase until it reaches a maximum at $x = \lambda$. The movement of M_2, results in a sequence of minima and maxima. Figure 2.5 shows the output intensity plotted against the optical path difference for a monochromatic wave. The resulting intensity vs. path difference plot is called an interferogram.

2.2.2 Polychromatic light source

So far we have considered a monochromatic light source, which produces an interferogram as shown in Fig. 2.6a. When the light source contains more than one wavelength, the intensity at the detector for each wavelength follows a relation like Eq. 2.5, but with a wavelength dependent period. Thus, the resulting interferogram can be described as as sum of cosine functions for all wavelengths in the spectrum. For example, for a light source that contains two wavelengths the interferogram shows a beating between two frequencies as shown in Fig. 2.6b. A Fourier transform of this interferogram would reveal two delta function peak located at the frequencies ω_1 and ω_2. The Fourier transform of the interferogram corresponding to a polychromatic source would therefore resemble the amplitude of each frequency present in the interferogram. In the case of a continuous spectrum, constructive interference occurs simultaneously for all wavelengths only at zero path difference, where both mirrors are equal distances from the beamsplitter. At any other OPD, some wavelengths interfere constructively while others do not, leading to the interferogram shown in Fig. 2.6c (right-hand panel).

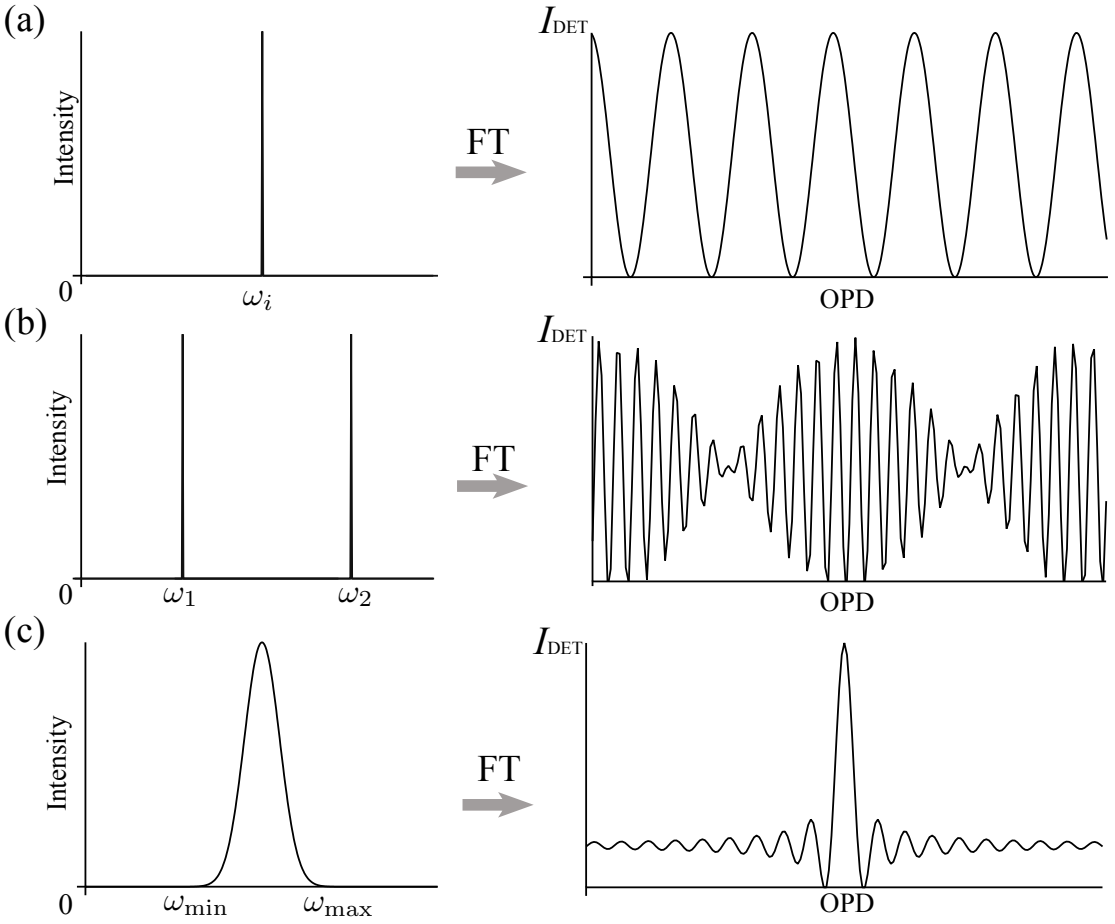

FIGURE 2.6: Simple spectra and interferograms. (a): A single wavelength; (b): two wavelength; (c): broad wavelength spectrum. FT - denotes Fourier transform.

The following section is taken from Ref. [14]. Assuming that the polychromatic source is a continuous source with frequencies from 0 to some maximum frequency ω_m, the intensity as a function of the OPD can be obtained from Eq. (2.5) by integrating over ω:

$$I(x) = 2\int_0^{\omega_m} I(\omega)[1+\cos(2\pi\omega x)]d\omega = 2\int_0^{\omega_m} I(\omega)d\omega + 2\int_0^{\omega_m} I(\omega)\cos(2\pi\omega x)d\omega \quad (2.6)$$

By setting $x = 0$, one gets:

$$\frac{I(0)}{2} = \int_0^{\omega_m} I(\omega)d\omega \quad (2.7)$$

By combining equations (2.6) and (2.7), an expression for the interferogram obtained on the detector can be found as:

$$I(x) - \frac{1}{2}I(0) = \int_0^{\omega_m} I(\omega)\cos(2\pi\omega x)d\omega \quad (2.8)$$

The interferogram of a source consisting of many wavelengths is shown in the right-hand panel of Fig. 2.6c. This interferogram has maximum constructive interference

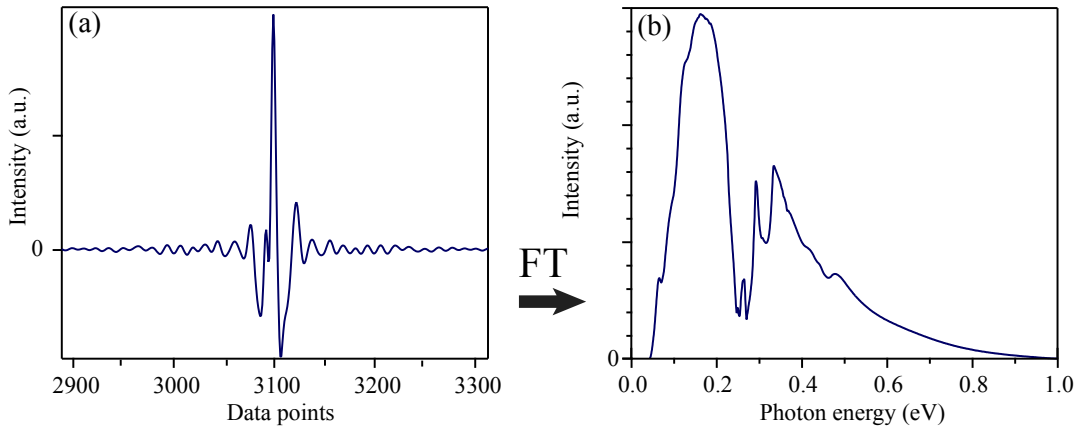

FIGURE 2.7: (a): An example of an interferogram; (b): the Fourier transformed resulting spectrum.

at zero path difference, which results in the central peak. For large OPD's ($x \to \infty$), contributions of constructive and destructive interference completely cancel and Eq. (2.8) integrates to zero. This leads to the relation $I(\infty) = \frac{1}{2}I(0)$ [14].

Equation (2.8) shows how the interferogram measured by a spectrometer is related to the input spectrum. When experiments are done we record interferograms and we would like to know the spectrum. Therefore we need the inverse transformation of Eq. (2.8):

$$I(\omega) = \int_{-\infty}^{\infty} [I(x) - I(\infty)] e^{2\pi i \omega x} dx \tag{2.9}$$

Here we have made use of the fact that $\frac{1}{2}I(0) = I(\infty)$ and we have taken the complex Fourier transform instead. Also, note that we took the integral from $-\infty$ to ∞. The movement of the scanner is continuous, but the measured intensity has to be digitised before the Fourier transform can be performed. We are therefore unlikely to sample the maximum in intensity $I(0)$ at zero optical path difference. Eq. (2.9) prevents this problem by replacing $I(0)$ with $I(\infty)$. By taking the complex Fourier transform integral from $-\infty$ to ∞ we also circumvent problems introduced by a phase shift resulting from not accurately determine zero path difference (see also section 2.2.3).

An example of a Fourier transform of an interferogram is shown in Fig. 2.7.

2.2.3 Determination of the optical path difference

The FTIR spectrometer contains a helium-neon (HeNe) laser as an internal reference source (label 6 in Fig. 2.1). The laser beam follows the same light path through the interferometer. Due to the fact that the laser has a single wavelength of light, it produces an oscillating intensity similar to that shown in Fig. 2.6a. A small diode records the

HeNe laser intensity at the exit side of the interferometer. The intensity of the diode oscillates in time, reaching a maximum when the mirror moves 652 nm. When the diode reaches a voltage larger than some threshold value, a counter increases (with a forward movement of the scanner) or decreases (with backwards movement). In this way, the position of the scanning mirror can be determined with very high accuracy.

When the spectrometer is powered on, a first initialization takes place. During this initialization, the mirror is moved over its full mechanical range and the intensity is recorded. At the same time, the counter value is recorded. The value of the counter for maximum intensity is recorded and provides the best measure of zero optical path difference. This procedure is repeated whenever the beamsplitter is changed.

2.2.4 Integration limits and apodization

The Fourier transform integral Eq. (2.9) is over a distance from minus infinity to plus infinity, but in practice, it is limited by the finite length of the interferometer arms. The mirror M_2 moves over a range $2L$ centred around the zero optical path difference. The integral is, therefore:

$$I(\omega) = \int_{-L}^{L} [I(x) - I(\infty)] e^{2\pi i \omega x} dx \tag{2.10}$$

where the integration limits are imposed by the armlength of the interferometer. The finite range of the scanner introduces a serious problem and results in a strongly modified spectrum. To see the effect of a finite arm length, it is convenient to write Eq. (2.10) as [14]:

$$I(\omega) = \int_{-\infty}^{\infty} [I(x) - I(\infty)] e^{2\pi i \omega x} A(x) dx \tag{2.11}$$

with

$$A(x) = \begin{cases} 0 & |x| > L \\ 1 & |x| < L \end{cases} \tag{2.12}$$

The function (2.12) is known as a boxcar function. We can isolate the effect of $A(x)$ by making use of the convolution theorem for Fourier transforms (e.g. FT$[f \cdot g]$=FT$[f]\cdot$FT$[g]$). Figure 2.8a shows the boxcar function (2.12). Its Fourier transform $I(\omega)$ is shown in Fig. 2.8b. The function $I(\omega)$ turns out to be a strongly oscillating function of frequency. Moreover, it extends over a wide range of frequencies. The problem introduced by a finite arm length then becomes clear when we imagine a monochromatic source. In this case, the interferogram will look like that in Fig. 2.6a, while its spectrum is a delta function. If we measure the interferogram over a finite range and then Fourier transform we obtain the spectrum of Fig. 2.8b instead of a single frequency it appears as if we have a whole range of frequencies.

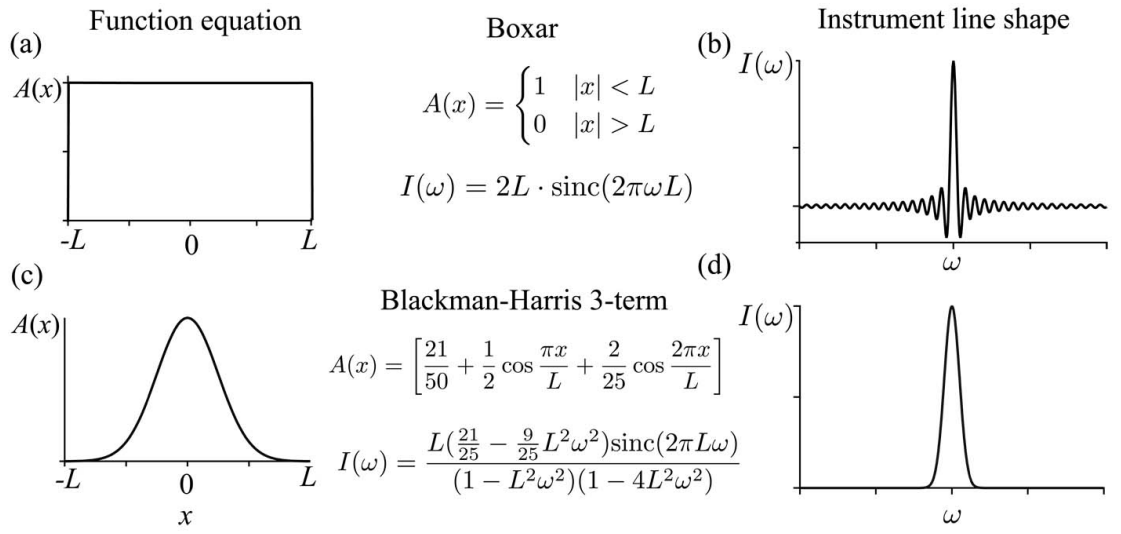

FIGURE 2.8: (a): The plot of the boxcar function; (b): resulting Fourier transform of the boxcar function; (c): the Blackman-Harris 3-term function [15]; (d): the resulting Fourier transform of Blackman-Harris 3-term function.

The introduction of the boxcar function is unavoidable. However, Eq. (2.11) suggests a possible solution: suppose we multiply the measured spectrum with another function $A(x)$ before taking the Fourier transform. The origin of the oscillations in the spectrum of the boxcar function comes from the sharp cutoff at $|x| = L$ (remember, it takes an infinite sum of cosines and sines to reproduced a step function). The idea is, therefore, to multiply the measured interferogram with a function $A(x)$ before Fourier transforming such that the cutoff effect is reduced. Such a cutoff function, $A(x)$, is known as an apodization function.

There are various apodization functions used in the literature [16–19]. These functions have been extensively compared. From these works, one comes to the conclusion that a function known as the Blackman-Harris 3-term apodization function provides the optimal solution between reducing the side-bands of the spectrum while maintaining spectral resolution. This function is displayed in panel 2.8c.

We can again calculate its Fourier transform and compare its effect to that of the boxcar function (Fig. 2.8d). The Blackman-Harris 3-term spectrum looks somewhat like a simple gaussian distribution. It has a central peak that is somewhat broader than the boxcar function and has a lower maximum. On the other hand, the side lobes seen in panel 2.8b are completely suppressed. The effect of the Blackman-Harris 3-term on the FT of a monochromatic wave interferogram is that the delta-function spectrum is broadened and its intensity somewhat reduced. The improved apodization, therefore, comes at the cost of spectrometer resolution. Nevertheless, this disadvantage outweighs the unphysical spectral features introduced by the boxcar function.

2.3 The construction of the cryostat

The spectrometer is coupled to a purpose-build, ultra-high vacuum (UHV) cryostat. The spectrometer-cryostat connection includes a chemical vapor deposition (CVD) grown diamond window, which is transparent over the entire energy range. The cryostat was constructed based on a design pioneered by the optical spectroscopy group of Dirk van der Marel at the University of Geneva and further improved upon in Amsterdam. The cryostat is constructed such that the sample position is stable as a function of temperature. This enables quantitatively accurate optical experiments to be performed as a function of temperature, during which the sample position in the beam remains fixed across the whole temperature range. The cryostat is cooled with liquid helium, which is transported from a dewar to the cryostat through a transfer tube. The lowest temperature that can be reached in the cryostat is 8 K.

To confirm the sample stability versus temperature, a HeNe laser was reflected from a mirror mounted on the sample holder in the cryostat to a screen positioned at 5 meters distance. The movement of the reflected beam on the screen was measured upon cooling down and warming up the cryostat. This test showed that the main sample movement on changing temperature was a tilt-like rotation around a horizontal axis and that this was smaller than 0.01 degrees while going from a sample temperature of 300 K to 8 K.

2.4 Sample preparation

The investigated samples are required to have a flat and smooth surface because, in the case of a bent, defect-rich or textured surface, the light beam would scatter in different directions. In order to obtain a flat surface, the samples were cut along a crystal axis. To properly orient the sample, Laue diffraction is used before cutting the sample. Another method to obtain a mirror-like surface for hard samples is to polish using diamond lapping films. In other cases, a shiny surface could be obtained by cleaving the sample using sticky tape.

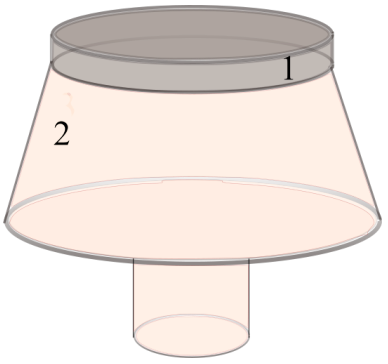

FIGURE 2.9: Schematic of sample holders used in our cryostat. 1 - sample, 2 - sample holder.

The samples are mounted on a sample holder, which is shaped like a cone, to prevent unwanted reflections from the sample holder. An example of the sample holder is shown in 2.9. Its flat surface is adapted to match the shape of the sample. This ensures that the part of the

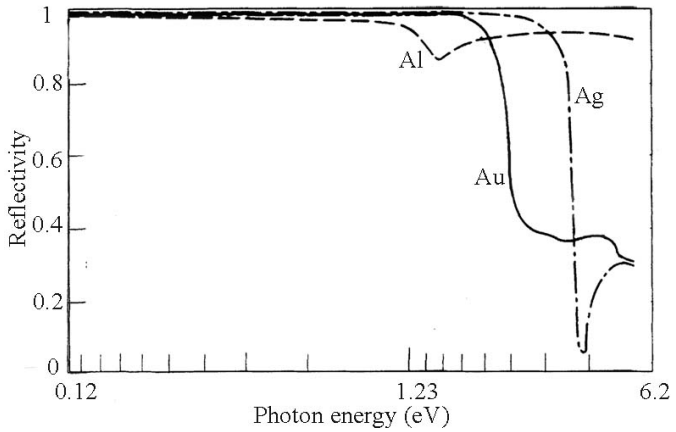

FIGURE 2.10: The reflectivity spectra of the reference metals. Figure is taken from [20]

light beam that does not impinge on the sample surface will be reflected away from the detector. The size of the tapered copper cone is adapted to each sample individually, and, afterwards, the cone has to be cleaned in ethanol and acetone to avoid contamination of the cryostat.

2.5 Reflectivity experiments

In order to obtain the reflectivity spectra of the investigated samples, experimental data are collected in two steps. In the first step, the intensity spectrum $I_S(\omega)$ of the sample is measured. In order to obtain the absolute value of the reflectivity, one also needs a reference spectrum $I_R(\omega)$. The reflectivity can then be calculated as:

$$R(\omega) = I_S(\omega)/I_R(\omega) \tag{2.13}$$

The reference intensity can be obtained by placing a mirror on the sample position. However, this approach can give large experimental errors, because sample and mirror might have different size and shape. Moreover, it is difficult to place the mirror in exactly the same position and orientation as the sample, resulting in large errors. The second approach is an in-situ evaporation of reference materials. A thin film of a reference metal is then evaporated on the sample surface and acts as a "perfect" replacement mirror for the sample.

As a reference material, several metals such as gold (Au), silver (Ag) and aluminium (Al) are used. The reflectivity spectra of these materials are shown in Fig. 2.10. In the infrared (IR) range these three metals each give $> 99.9\%$ reflectivity, even in thin film form. However, both Al and Ag have a tendency to slowly oxidise and this may introduce a time-dependent decrease of the reference spectra. Therefore Au is the most widely used

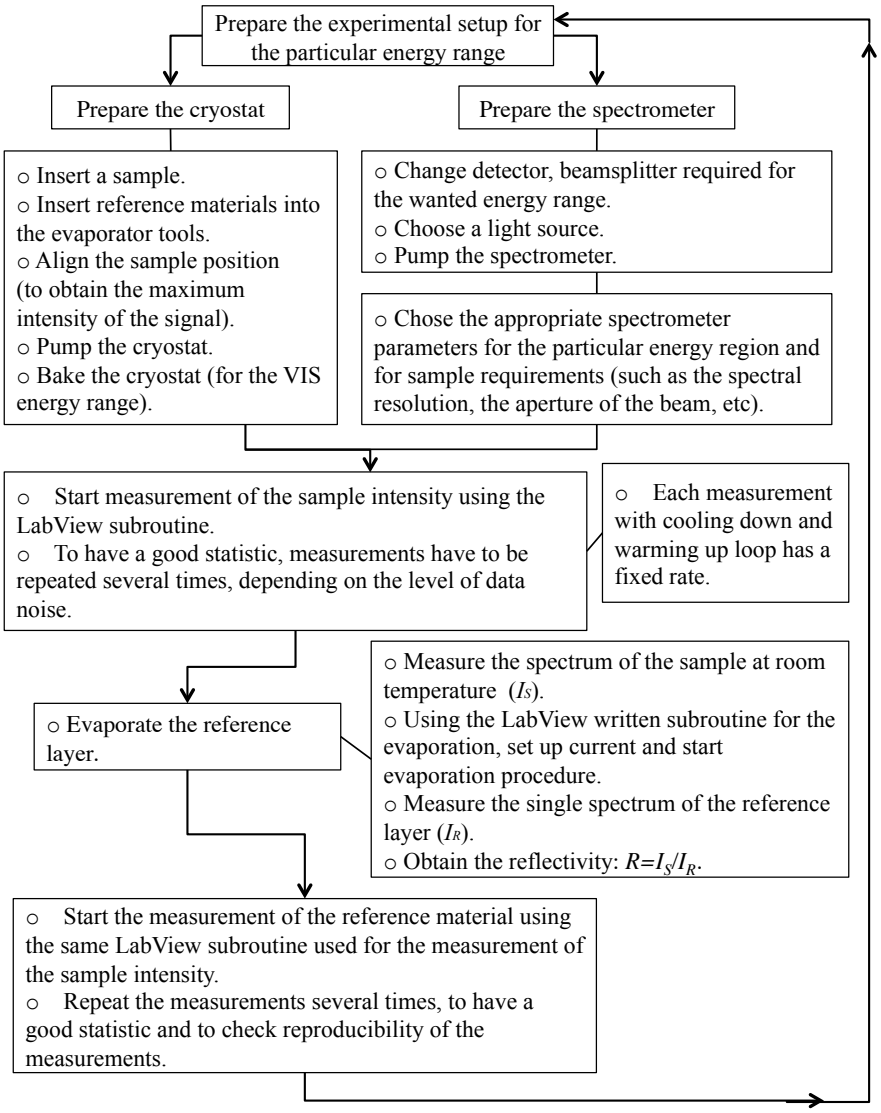

FIGURE 2.11: Schematic block diagram of a typical experiment.

reference material in the IR. On the other hand, Au has a series of interband transitions in the visible range of the spectrum, resulting in a plasma edge around 1 eV. This results in a suppression of the reflectivity starting already around 0.75 eV (see Fig. 2.10). This makes Au unusable as reference material at higher energies. A good alternative would be aluminium with a plasma edge in the UV energy range. Unfortunately, Al also has an interband transition around 1.4 eV (see Fig. 2.10). This brings us to the third reference, namely Ag. Ag has a higher plasma edge compared to gold extending roughly to the UV energy range. In the energy range between approximately 0.75 eV and 1.7 eV Ag provides the best reference material. Above 1.7 eV Al is used. A final important remark is that the reflectivity of Al above 1.7 eV is frequency independent, but only has a reflectivity of 90%. Therefore, in order to calculate $R(\omega)$ according to Eq. (2.13) we need to multiply by 0.9. We can obtain a good estimate for the error introduced in this

way by comparing the resulting reflectivity spectra in the range around 0.8 eV where both Al and Ag have been measured and should give equal reflectivity.

2.5.1 Basic experimental procedures

For each energy range, the temperature dependence of $I_S(\omega, T)$ and $I_R(\omega, T)$ is measured. For this purpose, a subroutine running in a LabView is used to record simultaneously the sample temperature, the pressure in the cryostat and to collect the spectra. A series of such measurements is then carried out while the sample is being cooled at a fixed rate followed by a similar warming up cycle.

After each warming and cooling cycle, we compare the temperature dependence to previous runs. In principle, this should result in a series of identical curves for a given frequency. After each measurement, we can average the data to obtain a feeling for the signal-to-noise in the experimental data. This is particularly important at the lowest and highest frequencies for a given set of detector and beamsplitter. As figure 2.3 shows, the source intensity is low in the range of overlap between the spectra, we need to achieve a sufficient spectral/noise ratio also in this range to be able to properly match the reflectivity spectra in these ranges. Once we are certain that these factors are sufficient, we can prepare the evaporation of the reference material. Figure 2.11 describes the steps taken to obtain a complete reflectivity spectrum as function of temperature.

2.5.2 Evaporation of reference materials

The cryostat includes two evaporators allowing the deposition of layers of different reference materials, for a given combination of beamsplitter and detector. The schematic picture of the evaporator is shown in Fig. 2.12. In particular, two evaporators are required for the VIS energy range when both Ag and Al reference layers are used. The necessity of both materials is discussed above in section 2.5.

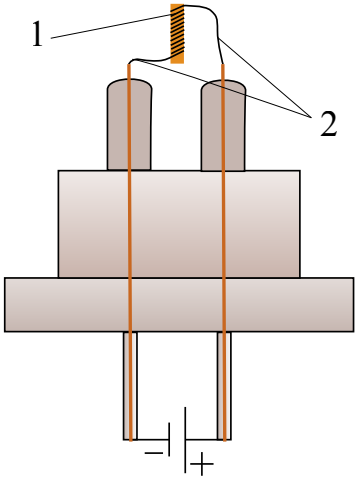

FIGURE 2.12: Schematic picture of the evaporator. 1 - reference material, 2 - tungsten wires.

The sources of the reference materials are in the form of a thin wire in the order of a millimeter in diameter. A 4 mm long Au, Ag or Al wire is cut off for each evaporation procedure. Afterwards, the piece of the reference material is wrapped in tungsten wire and

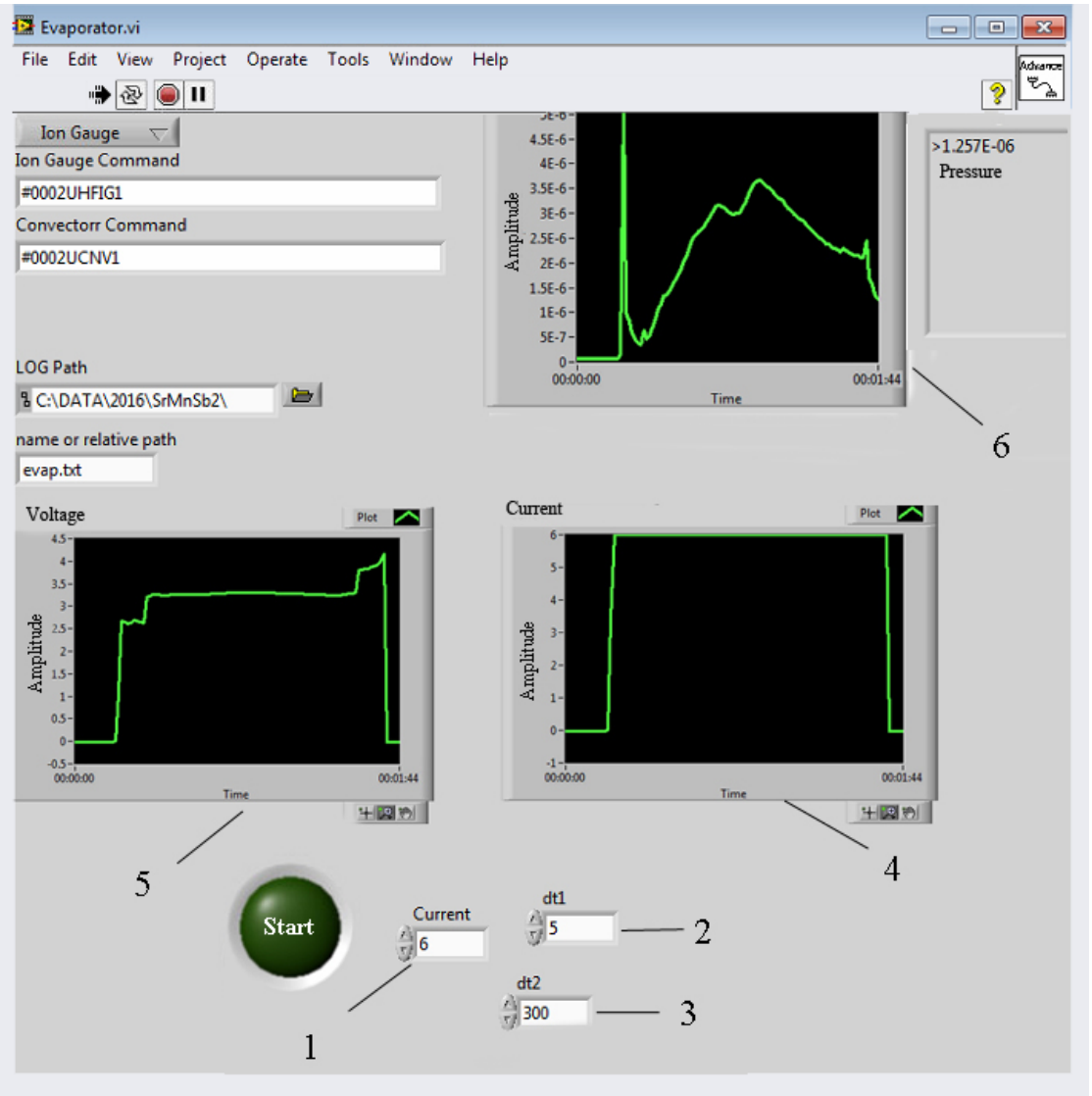

FIGURE 2.13: The interface of LabView subroutine written to perform an evaporation procedure. 1 - current in Ampere; 2 - current ramp time in second; 3 - time interval of current flow in seconds; 4, 5, 6 - are the time dependence graphs of current, voltage and pressure respectively.

installed into the evaporator (see Fig. 2.12). To make a thin-film deposition, a voltage is applied across the two ends of the tungsten wire; the current flows through the wire and this warms the reference metal sufficiently that it is evaporated and deposited onto the sample. Evaporation of the reference layer is normally done at room temperature. A LabView subroutine has been written to perform an evaporation. This routine allows to control the current, a current ramp rate and check the change of pressure. The interface of this routine is shown in Fig. 2.13. The current is ramped up to 6 A in a few seconds (labels 1 and 2 in Fig. 2.13)and then kept constant until the measured spectrum stops changing due to the deposition of the reference layer. In the case of a similar reflectivity of the investigated sample and reference material, the evaporation is conducted until the evaporator is empty. This is signaled by a change in the resistance of the tungsten coil

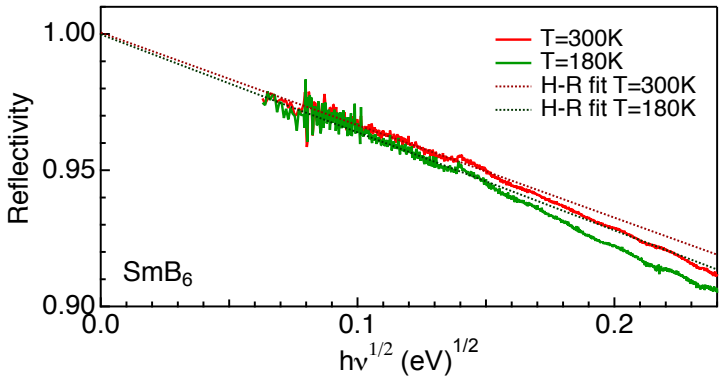

FIGURE 2.14: An example of Hagen-Rubens extrapolation of investigated SmB_6 compound.

and can be viewed as a sharp increase of the voltage. Before and after evaporation of the reference material a single spectrum is measured in order to get the most reliable measure of the reflectivity, which is used further in the data analysis.

2.5.3 Accurate determination of reflectivity spectra

After the reference layer is deposited, the whole measurement procedure is repeated. At the end of this first set of measurements, we can use Eq. (2.13) to finally obtain the reflectivity of the sample. This whole series of experiments needs to be repeated for each of the different ranges shown in Fig. 2.3. In principle, these different reflectivity spectra should match perfectly in the range of overlap. In practice, this does not always work, for example as a result of changes in environmental conditions (e.g. temperature of the laboratory). Another source for mismatches arises when ranges with different reference materials are compared. Typical error bars introduced in this way are on the order of $\pm 0.5\%$. Once the spectra are merged together, we have obtained the full temperature dependent reflectivity in the photon energy range from 5 meV to 4.6 eV. After we have obtained the reflectivity in the entire frequency range, we can check the calibration of our reflectivity data. To do this we make use of the so-called Hagen-Rubens relation (see chapter 5), which is valid for metals only:

$$R(\omega) \approx 1 - \sqrt{\frac{2\omega}{\pi \sigma_{DC}}} \tag{2.14}$$

As (2.14) shows, for a metal, the reflectivity extrapolates to one for $\omega \to 0$. If we plot our experimental data against $\sqrt{\omega}$, we should find a straight line that extrapolates to one. Fig. 2.14 shows, as an example, reflectivity data for SmB_6 in the metallic state (see chapter 5). The dashed lines are linear fits and demonstrate the good calibration of

our data. Note that the data deviates from the HR relation at higher energy, indicating the breakdown of this approximation.

2.6 From reflectivity data to optical properties

As will be discussed in chapter 5, the ultimate goal of any optical experiment is to determine the dielectric function $\hat{\epsilon}(\omega) = \epsilon_1(\omega) + i\epsilon_2(\omega)$. Our reflectivity experiments only provide limited access to this complex function, as can be seen by considering the Fresnel equations.

The Fresnel equations provide the relation between an incoming electromagnetic wave, $E_i(\omega)$, and the reflected and transmitted waves ($E_r(\omega)$ and $E_t(\omega)$ respectively) at an interface between two media (see Fig. 2.15). Here we only consider the relation between $E_r(\omega)$ and $E_i(\omega)$:

$$\frac{E_i(\omega)}{E_r(\omega)} = \frac{\hat{n}_1(\omega) - \hat{n}_2(\omega)}{\hat{n}_1(\omega) + \hat{n}_2(\omega)} \tag{2.15}$$

with $\hat{n}_i(\omega)$ the complex refractive index for medium i.

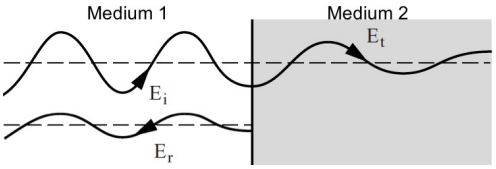

FIGURE 2.15: Schematic picture of the incident (E_i), reflected (E_r) and transmitted (E_t) electromagnetic waves traveling from medium 1 to medium 2. The change in amplitude as the wave travels away from the interface in medium 2 indicates a strongly absorptive medium. Figure taken from ref. [21].

The left-hand side of Eq. (2.15) is called the reflectance $\hat{r}(\omega)$ and since electromagnetic waves are complex, $\hat{r}(\omega)$ is also a complex function. Eq. (2.15) allows us to determine the complex refractive index, provided we know $\hat{r}(\omega)$. Assuming the incoming wave travels through vacuum $n_1(\omega) = 1$. Therefore ($\hat{n}_2(\omega) = \hat{n}(\omega)$):

$$\hat{n}(\omega) = \frac{1 - \hat{r}(\omega)}{1 + \hat{r}(\omega)} \tag{2.16}$$

The main problem that prohibits us from using Eq. (2.16) is that our detectors measure an intensity, $I(\omega) = |E(\omega)|^2$. This means that we only have access to the magnitude of the reflectance, i.e. $R(\omega) = \sqrt{|r_1|^2 + |r_2|^2}$, where r_1 and r_2 are the real and imaginary parts of the complex reflectance.

The most commonly used solution to this problem is by making use of the so-called Kramers-Kronig relations. These relations state that the real and imaginary parts of complex response functions are related by an integral transformation (see also chapter 3). Although the reflectance is not formally a response function, Eq. (2.16) imposes a

form of the KK relations on it (since $\hat{n}(\omega)$ is a response function). One can show that if $\hat{r}(\omega)$ is written as,

$$\hat{r}(\omega) = |\hat{r}(\omega)|e^{i\Theta(\omega)} \tag{2.17}$$

the phase $\Theta(\omega)$ can be obtained from $|r(\omega)|$ according to,

$$\Theta(\omega) = -\frac{\omega}{\pi} P \int_0^\infty \frac{\ln R(\omega')}{\omega'^2 - \omega^2} d\omega' \tag{2.18}$$

Therefore, if we measure $R(\omega)$ over a wide enough energy range, we can reconstruct $\Theta(\omega)$. One problem is that formally we need to measure from $\omega = 0$ to $\omega \to \infty$ and practically this is impossible. To reconstruct the phase $\Theta(\omega)$ we need low and high-frequency extrapolations. For metals, one can use the Hagen-Rubens extrapolation (see chapter 5) to extrapolate to $\omega = 0$, but for insulators, no good approximation exists. The high energy extrapolation of (2.18) is even more complicated since there can (and typically are) many unknown interband transitions outside our experimental range. Fortunately (2.18) depends on $(\omega^2 - \omega'^2)^{-1}$ so that the contribution of high energy interband transitions is small at low energy ω (for which $\omega << \omega'$).

Given these issues, many people have developed different methods to obtain the dielectric function. This can be done by doing additional experiments. For example, one could measure the transmission (in the case of insulators) and combine the results or resort to completely different techniques such as ellipsometry. We follow a different approach, which was developed by A.B. Kuzmenko [22].

2.6.1 KK-constrained variational dielectric functions

A better method to obtain the optical conductivity from the measured reflectivity is introduced in Ref. [22]. The method consists of two steps, both of which are implemented in the freeware package *RefFit* [23]. In the first step, a Drude-Lorentz model is used to fit the measured reflectivity with a set of oscillators:

$$\epsilon(\omega) = \epsilon_\infty + \sum_{k=1}^{N} \frac{\omega_{p,k}^2}{\omega_{0,k}^2 - \omega^2 - i\omega\gamma_k} \tag{2.19}$$

where $\omega_{0,k}$ is the resonance frequency, $\omega_{p,k}$ is the oscillator strength, γ_k is the scattering rate and ϵ_∞ is the contribution from high-frequency oscillators outside the experimental range. The Lorentz oscillator with $\omega_0 = 0$ reproduces the Drude term. An example of the Drude-Lorentz model, obtained for SmB_6 (see chapter 5), is shown in Fig. 2.16. Figure 2.16a depicts both the measured reflectivity of SmB_6 (blue dots) as well as calculated reflectivity using Eq. (2.19) with parameters indicated in Fig. 2.16b. The extrapolation

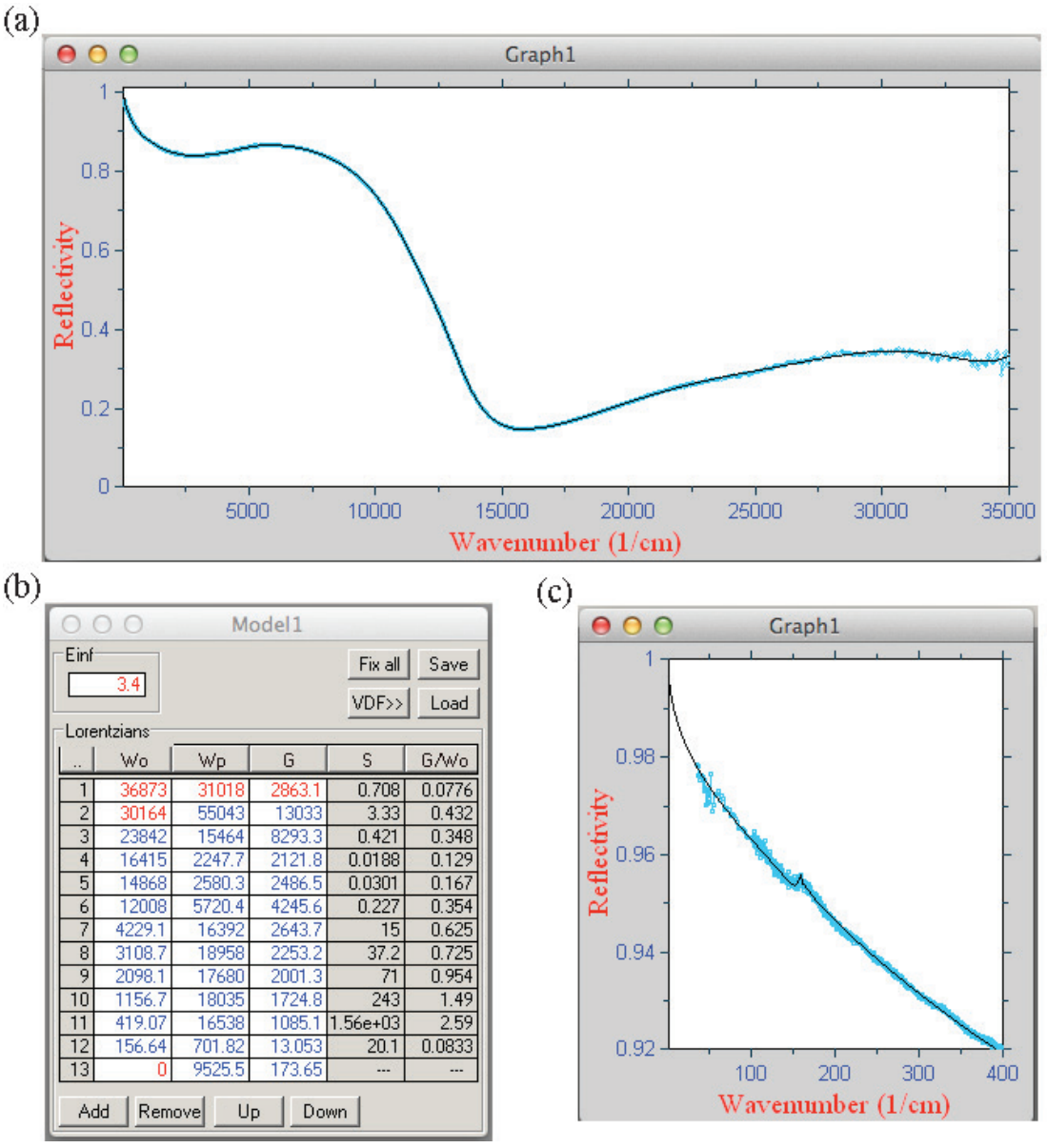

..	Wo	Wp	G	S	G/Wo
1	36873	31018	2863.1	0.708	0.0776
2	30164	55043	13033	3.33	0.432
3	23842	15464	8293.3	0.421	0.348
4	16415	2247.7	2121.8	0.0188	0.129
5	14868	2580.3	2486.5	0.0301	0.167
6	12008	5720.4	4245.6	0.227	0.354
7	4229.1	16392	2643.7	15	0.625
8	3108.7	18958	2253.2	37.2	0.725
9	2098.1	17680	2001.3	71	0.954
10	1156.7	18035	1724.8	243	1.49
11	419.07	16538	1085.1	1.56e+03	2.59
12	156.64	701.82	13.053	20.1	0.0833
13	0	9525.5	173.65	---	---

FIGURE 2.16: (a): the measured reflectivity data (blue dots) and model curve of the reflectivity (black line); (b): an example of the model window in RefFit software; (c): the low frequency reflectivity.

to the low-frequency range is shown in Fig. 2.16c. This extrapolation is calculated using the analytical form of the Drude-Lorentz model and is, therefore, different from Hagen-Rubens. Thus, if the calculated reflectivity well reproduces the experimental data we can assume that the model gives approximately correct extrapolations outside of the experimental frequency range [22]. The same holds for the high-frequency extrapolation. Once a set of oscillators is found that describes the experimental data, in the second step a variational dielectric function can be added on top of the Drude-Lorentz model, such that $\epsilon_{tot}(\omega) = \epsilon_{mod}(\omega) + \epsilon_{var}(\omega)$. This $\epsilon_{var}(\omega)$ should reproduce all detailed features of the reflectivity spectrum, including noise.

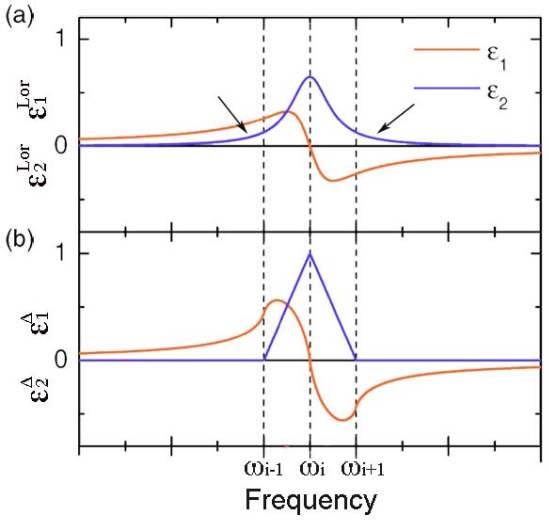

FIGURE 2.17: The real and imaginary part of the dielectric function with Lorentz (a) and triangular (b) line shape. Figure is taken from [22]

A detailed mathematical representation of the variational dielectric functions is given in Ref. [22]. The starting point is a reflectivity spectrum $R(\omega)$ in the frequency range $[\omega_{min}, \omega_{max}]$, with a set of datapoints given by $\{\omega_i^{exp}, R_i^{exp}\}$, $(i = 1, ..., N_{exp})$, where $\omega_1^{exp} = \omega_{min}$ and $\omega_N^{exp} = \omega_{max}$.

The reflectivity can be obtained from the real $\epsilon_1(\omega)$ and the imaginary $\epsilon_2(\omega)$ part of the dielectric function of a material as:

$$R(\omega) = \left| \frac{1 - \sqrt{\hat{\epsilon}(\omega)}}{1 + \sqrt{\hat{\epsilon}(\omega)}} \right|^2 \tag{2.20}$$

Therefore, in order to calculate the reflectivity, one needs to define the dielectric function. One of the possible ways is to set Lorentz oscillators $\epsilon_{1,i}^{Lor}$, $\epsilon_{2,i}^{Lor}$, shown in Fig. 2.17a, centred at each experimental frequency ω_i^{exp}. The linewidths of the oscillators γ_i is fixed being $\gamma_i = (\omega_{i+1} - \omega_{i-1})/2$ on the order of the interval between neighbours frequency points. However, as can be seen, the Lorentzian line shape has slowly decaying low and high-frequency tails (indicated by arrows in Fig. 2.17a), which can lead to bad quality fitting. The problem reveals itself if one considers a material with an energy gap at ω_g (thus, $\epsilon_2(\omega) = 0$ for frequency $\omega < \omega_g$). Each oscillator which is introduced above ω_g will provide non-zero value of ϵ_2 below ω_g due to low-frequency tails of Lorentzians. Kuzmenko [22] proposed to use a more "local" function, such as the triangular function, in order to have non-zero value only in close vicinity of ω_i. Figure 2.17b shows the real and imaginary part of the dielectric function with the triangular line shape, where a triangular function has a finite value only inside the narrow region $[\omega_{i-1}, \omega_{i+1}]$. In this case, the variational dielectric function can be calculated as a linear superposition of

triangular functions $\epsilon_i^{\Delta}(\omega)$ at frequencies ω_i [22]:

$$\epsilon_{var}(\omega) = \sum_{i=1}^{N} A_i \epsilon_i^{\Delta}(\omega) \tag{2.21}$$

where the coefficients A_i are free parameters of the variational function. An analytical expression for $\epsilon_i^{\Delta}(\omega)$ can be found in Ref. [22]. The free parameters of the imaginary part of $\epsilon_{var}(\omega)$ have straightforward physical meaning: they represent the values of ϵ_2 at every frequency point ω_i. The real part of $\epsilon_{var}(\omega)$ is obtained by using the KK relation, similar to the one introduced above for a phase (2.18).

$$\epsilon_1(\omega) - 1 = \frac{2}{\pi} P \int_0^{\infty} \frac{\omega' \epsilon_2(\omega')}{\omega'^2 - \omega^2} d\omega' \tag{2.22}$$

In the final fitting procedure the set of the oscillators of the $\epsilon_{mod}(\omega)$ are fixed, in order to reproduce the features of the experimental data, only the parameter A_i is kept free.

Chapter 3

A window on topological and correlated electrons.

This chapter presents the theoretical background of optical processes in solids. We start in section 3.1 from the classical electromagnetic theory of the interaction of light and matter and show how this can be used to derive the so-called Drude-Lorentz model. In section 3.2 we discuss aspects of the calculation of the electronic band structure, focusing on density functional theory. This discussion forms the basis for the discussion of the microscopic description of optical properties of solids in section 3.3. Finally, in section 3.4 we briefly discuss correlation driven phase transitions and the relation with topological classifications. This section is concluded with a discussion of the signatures of electron-electron correlations in experiments.

3.1 The classical description of the interaction of light and matter.

3.1.1 The polariton wave equation.

Maxwell's equations provide a description of all classical electromagnetic phenomena, including the interaction between light and matter. Maxwell's equations are given by:

$$\vec{\nabla} \cdot \vec{E}(\vec{r},t) = 4\pi\rho(\vec{r},t) \tag{3.1}$$

$$\vec{\nabla} \times \vec{E}(\vec{r},t) = -\frac{1}{c}\frac{\partial \vec{B}(\vec{r},t)}{\partial t} \tag{3.2}$$

$$\vec{\nabla} \cdot \vec{B}(\vec{r},t) = 0 \tag{3.3}$$

$$\vec{\nabla} \times \vec{B}(\vec{r},t) = \frac{1}{c}\frac{\partial \vec{E}(\vec{r},t)}{\partial t} + \frac{4\pi}{c}\vec{J}(\vec{r},t) \tag{3.4}$$

where $\vec{E}$ and $\vec{B}$ are the electric and magnetic fields. The electric charge and current density are denoted by ρ and $\vec{J}$ respectively and c represents the speed of light.

We will assume that an electromagnetic field is generated well outside the solid and that its source is not relevant to the response of the solid. This external field is typically assumed to be a plane wave field of the form,

$$\vec{E}(\vec{r},t) = E_0 e^{i(\vec{k}\cdot\vec{r}-\omega t)} \tag{3.5}$$

where $\vec{k}$ is the wave vector along the direction of propagation and ω is the angular frequency of the field. To describe the interaction of this external field with charged particles inside the solid requires us to properly identify additional sources (i.e. $\rho(\vec{r},t)$ and $J(\vec{r},t)$) of electromagnetic fields. The sources for the current density in a solid derive from the response of electrons to the time varying electromagnetic field. Typically three contributions are distinguished. The first is the response of nearly free electrons. This response is equivalent to Ohm's law describing the flow of current when one applies a voltage over a metal wire. However, a second contribution should be considered and is associated with the changes of the polarization induced by the time variation of the electric field. Finally, there is a third contribution to the current density deriving from the magnetization induced by the magnetic field component. If we assume that the solid does not charge under the influence of the external field, we can make use of charge conservation and the continuity equation to eliminate the charge density from Maxwell's equation. Furthermore we assume that the applied electromagnetic field is sufficiently weak so that we can make use of the assumption of linear response. Under this assumption we have that the induced free charge current $\vec{J}$, polarization $\vec{P}$ and magnetization $\vec{M}$ can be expressed in terms of the applied field as:

$$4\pi\vec{P}(\vec{r},t) = (\epsilon - 1)\vec{E}(\vec{r},t) \tag{3.6}$$

$$4\pi\vec{M}(\vec{r},t) = (\mu^{-1} - 1)\vec{B}(\vec{r},t) \tag{3.7}$$

$$\vec{J}(\vec{r},t) = \sigma\vec{E}(\vec{r},t) \tag{3.8}$$

ϵ and μ in these expressions are the dielectric permittivity and magnetic permeability, respectively and σ is the conductivity. The proportionality constants are chosen such that the final wave equations are simplified somewhat. A second point that should be made is that we have implicitly assumed that the solid is homogeneous and isotropic. This is evident from the fact that the proportionality constants are given by a simple

scalar value as opposed to a position and time dependent tensor that they could, in principle, be.

By combining Maxwell's equations Eq. (3.2) and Eq. (3.4) and making use of the linear response equations Eq. (3.6)-Eq. (3.8), one can eliminate all sources and derive a so-called wave equation for the electromagnetic fields. For electric fields we have:

$$\nabla^2 \vec{E}(\vec{r},t) = \frac{\epsilon\mu}{c^2}\frac{\partial^2 \vec{E}(\vec{r},t)}{\partial t^2} + \frac{4\pi\sigma\mu}{c^2}\frac{\partial \vec{E}(\vec{r},t)}{\partial t} \tag{3.9}$$

This differential equation describes the propagation of electric fields through solids where the material dependence is captured by the values of the permeability, permittivity and conductance. A similar wave equation for the propagation of the magnetic field can be derived.

For an infinite solid we don't have to worry about boundary effects and we can assume that the electric field component is equally well described by Eq. (3.5). Taking this as the solution, we obtain from Eq. (3.9) the so-called 'polariton' dispersion relation:

$$\omega = \frac{c|k|}{\sqrt{\mu(\epsilon(\omega) + \frac{i4\pi\sigma(\omega)}{\omega})}} \tag{3.10}$$

This dispersion relation describes the total set of solutions to Eq. (3.9). In vacuum ($\sigma = 0$; $\mu, \epsilon = 1$), this equation reduces to $\omega = c|k|$ as expected. In a medium where $\sigma(\omega), \mu(\omega)$ and $\epsilon(\omega)$ are finite, Eq. (3.10) shows that the speed of light, c, effectively is reduced due to the coupling to collective excitations of the solid. Another way of saying this is that the photons inside the solid get 'dressed' by polarization clouds. The effective quasi-particle is also called a *polariton*. The next step in the description of the interaction of light and matter requires a description of the material dependent optical constants.

3.1.2 Dielectric function or optical conductivity?

So far, we have not specified $\epsilon(\omega)$ and $\sigma(\omega)$ introduced in the equations above (in most solids the magnetic permeability is very small compared to the dielectric response, so we will set μ=1). These two quantities were introduced above as the proportionality constants of the different responses to applied fields (e.g. Eq. (3.6) - Eq. (3.8)), but in modern linear response theory are considered to be two sides of the same coin. We redefine these quantities as $\epsilon_1(\omega)$ and $\sigma_1(\omega)$ and consider them to be the real parts of a complex function. We now note that the square root in the denominator of Eq. (3.10)

can be written as a single complex number according to:

$$\hat{\epsilon}(\omega) \equiv \epsilon_1(\omega) + \frac{4\pi i}{\omega}\sigma_1(\omega) \tag{3.11}$$

This allows us to identify the imaginary part of a complex dielectric function, $\hat{\epsilon}(\omega) = \epsilon_1(\omega) + i\epsilon_2(\omega)$ with $\epsilon_2(\omega) = \frac{4\pi}{\omega}\sigma_1(\omega)$. The real part of the dielectric function describes the reactive response of the solid to an external perturbation and the imaginary part the dissipative response. Note that we could have equally introduced a complex optical conductivity function. Indeed, it is easy to show that these two complex functions are related according to:

$$\hat{\epsilon}(\omega) = 1 + i\hat{\sigma}(\omega)\frac{4\pi}{\omega} \tag{3.12}$$

The dispersion relation can now be compactly written as:

$$\omega = \frac{ck}{\sqrt{\hat{\epsilon}(\omega)}} \tag{3.13}$$

To fully describe the optical response of a solid we need to calculate the complex dielectric function of the material. Simple semi-classical models were developed at the turn of the 20th century as we will discuss in the next section.

3.1.3 The Drude-Lorentz model

A phenomenological description of the optical response of solids was given by Drude at the same time as when the first hints of quantum mechanics were discovered. Drude had knowledge of the existence of electrons and atoms, but could obviously not oversee the implications of the 'quanta' that were discovered by Planck in the same year (1900). Drude imagined that the electrons in a solid would move under the influence of an applied electric field. The model is nowadays still used as an approximate description of the response of free charge carriers in a metal or semiconductor. However, as we will show later, interactions and quantum mechanical effects can alter the frequency dependence of the optical response predicted by the Drude model. Drude considered a gas of charged particles moving under the influence of a time-varying electric field. He realized that as the particles moved, they would collide with atoms resulting in an effective frictional or damping force. This led to a Newtonian equation of motion for the charged particles that was easily solved and provided an expression for the (optical) conductivity. H.A. Lorentz realized that there could be an additional restoring force acting on the electrons, resulting in a combined model now known as the Drude-Lorentz model (it is not clear when Lorentz introduced this idea: wikipedia mentions 1905

without reference, but Lorentz already mentions this model in his 1902 Nobel lecture [24]).

There are different derivations of the Drude-Lorentz model possible (see for example, [21]). We follow the equation of motion approach for a single particle with charge e and mass m, moving under the influence of an applied electric field $\vec{E}$. Drude assumed that the effect of collisions experienced by the electron could be captured by a phenomenological force, $F = -\Gamma m\vec{v}$, that describes a damping force. Here $\Gamma = 1/\tau$ is known as the scattering rate. The τ in Drude's model describes the average time between collisions of the particle with atoms. The extension to the model proposed by Lorentz involves adding an additional restoring force $F = -K\vec{x}$, acting on the electrons. This force describes the approximate spring like force experienced by electrons as they move away from the oppositely charged nucleus. The equation of motion is completed by adding the force resulting from the electric field, $F = -e\vec{E}(t)$ (note that we ignore the Lorentz force; the prefactor of this force is proportional to $1/c$ and can be ignored). Newton's law, $F = ma$ thus gives us:

$$m\frac{d^2\vec{x}(t)}{dt^2} = -m\Gamma\frac{d\vec{x}(t)}{dt} - K\vec{x}(t) - e\vec{E}(t) \tag{3.14}$$

The differential equation is easily solved by introducing the Fourier expansion of $\vec{E}(t)$ and $\vec{x}(t)$, resulting in a relation between the Fourier components:

$$\vec{x}(\omega) = \frac{-e\vec{E}(\omega)}{m(\omega_0^2 - \omega^2 - i\omega\Gamma)} \tag{3.15}$$

where $\omega_0^2 \equiv K/m$ is known as the resonance frequency. Next we consider an ensemble of such charges with density n. The current density is given by $\vec{j}(t) = -en\vec{v}(t)$ and after another Fourier expansion we find a relation between the Fourier components of the current and the electric field:

$$\vec{j}(\omega) = \frac{ne^2}{m}\frac{i\omega}{i\omega\Gamma - (\omega_0^2 - \omega^2)}\vec{E}(\omega) \tag{3.16}$$

Comparing with Eq. (3.8) we immediately obtain an expression for $\hat{\sigma}(\omega)$:

$$\hat{\sigma}(\omega) = \frac{\omega_p^2}{4\pi}\frac{i\omega}{i\omega\Gamma - (\omega_0^2 - \omega^2)} \tag{3.17}$$

where we introduced the plasma frequency $\omega_p^2 \equiv 4\pi ne^2/m$. The Drude expression for the free charge is obtained when the spring constant is set to zero (i.e. for $\omega_0 \to 0$):

$$\hat{\sigma}(\omega) = \frac{\omega_p^2}{4\pi}\frac{1}{\Gamma - i\omega} \tag{3.18}$$

Surprisingly, the Drude-Lorentz model is still used to this day. For the Drude model this is due to the fact that the effective description of nearly-free electrons in terms of non-interacting quasiparticles, as proposed by Landau, happens to be equivalent to the Drude's description of a gas of charged particles. Similarly, it turns out that the probability for transitions between different quantum mechanical states follows a dependence on energy that can be described approximately by the functional form of a Lorentz oscillator. The full optical conductivity in a solid can be written as,

$$\hat{\sigma}(\omega) = \frac{\omega_p^2}{4\pi}\frac{1}{\Gamma_f - i\omega} + \sum_i \frac{i\omega f_i^2}{i\omega\Gamma_i - (\omega_{0,i}^2 - \omega^2)} + \sum_{ph} \frac{i\omega f_{ph}^2}{i\omega\Gamma_{ph} - (\omega_{0,ph}^2 - \omega^2)} \tag{3.19}$$

where $f_{i/ph}$ are called the oscillator strength. The first term approximately describes the contribution to the response due to non-interacting quasi-particles. The second term describes electronic optical transitions and the last term describes the excitation of lattice vibrations in the solid. Other terms are in principle possible (for example, due to spin flip excitations or due to a contribution from excitons), but these are not relevant for the results presented in this thesis.

3.2 Quantum description of the electronic structure of solids

In this section, the basic theory behind the calculation of the band structure of solids is presented. We will start from the general expression for a many-body Hamiltonian, which is followed by the Born - Oppenheimer approximation. The band structure calculation is introduced through density functional theory.

3.2.1 Many-body Hamiltonian and Born - Oppenheimer approximation

The discussion presented in the following section is taken from the book by Salasnich, Ref. [25]. Let us consider N atoms; we therefore have a system consisting of N_P nuclei with masses M_P and electric charge $Z_P e$ and N_e electrons with mass m and charge $-e$. Thus, the Hamiltonian for such system is given by [25]:

$$\hat{H} = \hat{H}_P + \hat{H}_e + \hat{V}_{Pe} \tag{3.20}$$

where $\hat{H}_e$ and $\hat{H}_P$ are the Hamiltonians describing the electrons and nuclei, respectively and $\hat{V}_{Pe}$ is the Coulomb interaction between the nuclei and the electrons. The

Hamiltonian of the electrons $\hat{H}_e$ is given by:

$$\hat{H}_e = -\sum_{i=1}^{N_e} \frac{\hbar^2}{2m_e}\nabla_i^2 + \frac{1}{2}\sum_{i=1}^{N_e}\sum_{j\neq i=1}^{N_e} \frac{e^2}{|\vec{r}_i - \vec{r}_j|} \tag{3.21}$$

where $\vec{r}_i$ is the position of the i-th electron. The first term describes the kinetic energy and the second term describes the electron-electron interaction. Similarly, the Hamiltonian for the nuclei reads:

$$\hat{H}_P = -\sum_{P=1}^{N_P} \frac{\hbar^2}{2M_P}\nabla_P^2 + \frac{1}{2}\sum_{P=1}^{N_P}\sum_{Q\neq P}^{N_P} \frac{Z_P Z_Q e^2}{|\vec{R}_P - \vec{R}_Q|} \tag{3.22}$$

where $\vec{R}_P$ is the position of the P-th nucleus. The last term of Eq. (3.20) can be written as:

$$\hat{V}_{Pe} = -\frac{1}{2}\sum_{i=1}^{N_e}\sum_{P\neq i}^{N_P} \frac{Z_P e^2}{|\vec{r}_i - \vec{R}_p|} \tag{3.23}$$

The stationary Schrödinger equation for the full many-body system reads:

$$\hat{H}\psi(r_1, ..., r_{N_e}; R_1, ..., R_{N_P}) = \mathcal{E}\psi(r_1, ..., r_{N_e}; R_1, ..., R_{N_P}) \tag{3.24}$$

where $\psi(r_1, ..., r_{N_e}; R_1, ..., R_{N_P})$ is the full, many-particle wavefunction for all electrons and ions in the solid.

It goes without saying that the calculation of the ground-state energy and the wavefunction of the system with $(N_e + N_P)$ particles is a hopelessly complicated procedure. In order to make the first simplification, the Born-Oppenheimer approximation is often used. This approximation is based on the fact that the mass of an atomic nucleus is much larger than the mass of an electron and therefore the dynamics of the nuclei and electrons takes place on very different time scales. This allows us to separate the wavefunction in Eq. (3.24) into the product of two wavefunctions; one for the electron motion and the second for the nuclear motion. Another consequence of the Born-Oppenheimer approximation is that the potential term, Eq. (3.23), can be treated as a static potential through which the electrons move. The Schrödinger equation for electrons moving through a static potential landscape generated by the ion background can then be written as [25]:

$$\left(-\sum_{i=1}^{N_e} \frac{\hbar^2}{2m_e}\nabla_i^2 + V_{ee}(\vec{r}) + V_{Pe}(\vec{r}, \vec{R})\right)\psi_e(\vec{r}) = \mathcal{E}_e(\vec{R})\psi_e(\vec{r}) \tag{3.25}$$

where $\psi_e(\vec{r}, \vec{R})$ and $\mathcal{E}_e(\vec{R})$ are the electronic wavefunction and the eigenenergy respectively. Thus, Eq. (3.25) describes an electronic eigenstate for a particular configuration

of atomic positions. However, even after making the Born-Oppenheimer approximation, the Hamiltonian is still quite complicated, and it has to be further simplified by making the single particle approximation. This approximation replaces the complicated sum of potentials by a single effective potential leading to the following expression for the Hamiltonian:

$$\hat{H}_i = -\frac{\hbar^2}{2m_e}\sum_i \nabla_i^2 + U_{eff}(r_i) \tag{3.26}$$

where $U_{eff}(\vec{r})$ is an approximate expression that reflects the potential landscape (or mean field) generated by all nuclei and electrons through which a single electron moves. This expression forms the basis for the so-called tight binding approach that we learn in solid state textbooks. A more advanced method, based on Eq. (3.25), provides a better picture of the electronic structure of solids and is known as density functional theory. This method is the subject of the next section.

3.2.2 Density functional theory

This section is based on the discussion provided in Ref. [26]. Density functional theory (DFT) is based on the Hohenberg-Kohn theorems. These theorems state that the ground state properties of a system are determined by a unique functional of the ground state electron density $\rho(\vec{r})$. This approach reduces the N-body problem from $3N$ spatial coordinates to three spatial coordinates of the density functional. Within this method, the many-body effect such as electron-electron interaction is included approximately in the exchange-correlation potential. Further, the theorems state that the ground state properties of a system of interacting electrons can be determined by the minimization of the total energy as a functional of electron density (see [26], page 9):

$$E[\rho(\vec{r})] = T[\rho(\vec{r})] + \int V_{ext}(\vec{r})\rho(\vec{r})d\vec{r} + \int \rho(\vec{r})d\vec{r}\int \frac{\rho(\vec{r}')}{|\vec{r}-\vec{r}'|}d\vec{r}' + E_{xc}[\rho(\vec{r})] \tag{3.27}$$

where $T[\rho(\vec{r})]$ is the kinetic energy of non-interacting electron gas moving in the external potential $V_{ext}(\vec{r})$. The third term of Eq. (3.27) describes the Coulomb interaction energy which is associated with charge distribution $\rho(\vec{r})$. The last term $E_{xc}[\rho(\vec{r})]$ represents the exchange-correlation energy, which describes the energy differences between non-interacting and interacting systems and the contribution from non-classical electrostatic interaction. In DFT the required electron density $\rho(\vec{r})$ is expressed through a sum of all occupied single-electron states:

$$\rho(\vec{r}) = \sum_{i=1}^{N} |\phi_i(\vec{r})|^2 \tag{3.28}$$

where $\phi_i(\vec{r})$ is the single-electron eigenfunction and N is a total number of electrons in the system. In order to minimise functional Eq. (3.27) one has to vary it with respect to the wavefunctions $\phi_i(\vec{r})$ (with additional normalisation conditions for $\phi_i(\vec{r})$ [26]) which leads to the following equation:

$$\left[-\frac{\hbar^2}{2m_e}\nabla^2 + V_{eff}(\rho(\vec{r}))\right]\phi_i(\vec{r}) = \mathcal{E}_i\phi_i(\vec{r}) \tag{3.29}$$

where $V_{eff}(\rho(\vec{r}))$ is effective potential, which represents static mean field of the electrons and is given by:

$$V_{eff}(\rho(\vec{r})) = V_{ext}(\vec{r}) + e^2\int\frac{\rho(\vec{r}')}{|\vec{r}-\vec{r}'|}d\vec{r}' + \frac{\delta E_{xc}[\rho(\vec{r})]}{\delta\rho(\vec{r})} \tag{3.30}$$

where $\delta/\delta\rho$ is the functional derivative. Eq. (3.27) and Eq. (3.30) are referred to as the Kohn-Sham equations and have to be determined in a self-consistent way due to the fact that $V_{eff}(\vec{r})$ depends on $\rho(\vec{r})$.

DFT doesn't give us the precise expression for $E_{xc}[\rho(\vec{r})]$, resulting in further approximation schemes. The most widely used approximation is known as the local density approximation (LDA) for the exchange energy, $E_{xc}[\rho(\vec{r})]$:

$$E_{xc}^{LDA}[\rho(\vec{r})] = \int\epsilon_{xc}[\rho(\vec{r})]\rho(\vec{r})d\vec{r} \tag{3.31}$$

where $\epsilon_{xc}[\rho(\vec{r})]$ is the single particle exchange and correlation energy for electrons with total density $\rho(\vec{r})$. Since Eq. (3.31) now depends on the coordinates of a single particle, this approximation is in some sense equivalent to the single particle approximation. Various expressions for $\epsilon_{xc}[\rho(\vec{r})]$ have been proposed and the interested reader is referred to Ref.[27]. Given an expression for $\epsilon_{xc}[\rho(\vec{r})]$, $E_{xc}[\rho(\vec{r})]$ the Kohn-Sham equations can be solved and the electronic band structure of a particular solid can be obtained.

3.3 Optical transitions

In section 3.1 we discussed the classical description of the optical response leading to the Drude-Lorentz model. We already hinted at the fact that this description approximately held, even for band electrons in solids. In this section, we discuss the description of optical properties in terms of the microscopic properties of solids. The Kubo formalism provides the basis for understanding the interaction between light and band electrons. However, the basic physics can be understood by alluding to the somewhat simpler Fermi's golden rule description. We conclude this section with a brief discussion of

optical selection rules. Some elements of the Kubo formalism will be discussed in chapter 4.

3.3.1 The relation between electronic structure and optical properties of matter

The derivation presented in this section is taken from references [21] and [28]. We start from the Hamiltonian describing the system in the presence of an external electromagnetic field given by:

$$\hat{H} = \hat{H}_0 + \hat{H}_{int} \tag{3.32}$$

where $\hat{H}_0$ is the Hamiltonian in the absence of the external electromagnetic field. The second term $\hat{H}_{int}$ represents the interaction between the electrons and the external electromagnetic wave. The coupling we will use is derived from a minimal substitution and second order terms of the vector potential have been neglected. In such a form the interaction Hamiltonian is given by:

$$\hat{H}_{int} = \frac{e}{2m_e c}\sum_{i=1}^{N}[\vec{p}_i \cdot \vec{A}(\vec{r}_i) + \vec{A}(\vec{r}_i)\cdot\vec{p}_i] - \sum_{i}^{N} e\Phi(\vec{r}_i) \tag{3.33}$$

where $\vec{p}$ is the electron momentum, $\vec{A}$ is the vector potential and $\Phi(\vec{r}_i)$ is the scalar potential. The current density is given by:

$$\vec{J}(\vec{r}) = -\frac{e^2}{2m_e}\sum_{i=1}^{N}[\vec{p}_i\delta(\vec{r}-\vec{r}_i) + \delta(\vec{r}-\vec{r}_i)\vec{p}_i] - \frac{e^2}{m_e c}\sum_{i=1}^{N}\vec{A}(\vec{r}_i)\delta(\vec{r}-\vec{r}_i) \tag{3.34}$$

We can use this expression to rewrite Eq. (3.33). For transverse fields and thus $\Phi = 0$, we have:

$$\hat{H}_{int} = -\frac{1}{c}\int \vec{J}(\vec{r})\cdot\vec{A}(\vec{r})d\vec{r} \tag{3.35}$$

where terms quadratic in the vector potential have again been neglected. The derivation of the optical conductivity using the Kubo formalism is rather lengthy and will not be repeated here. Instead, we use Fermi's golden rule to approximately calculate the rate of a transition from an initial state to a final state. Its derivation straightforwardly follows from the Schrödinger equation and can be found, for example, in Ref. [21] or [29]. The transition rate is:

$$\lambda_{i\to f} = \frac{2\pi}{\hbar}\left|\langle f|\,\hat{H}_{int}\,|i\rangle\right|^2 \rho \tag{3.36}$$

where i denotes an initial state, f a final state and ρ is the density of final states. The term in brackets is also known as the matrix element of the transition. The total transition probability is then obtained by summing over all possible initial and final

states, resulting in [21]:

$$W = \sum_{i,f} W_{i\to f} = \sum_{i,f} \frac{2\pi}{\hbar} \left|\langle f|\hat{H}_{int}|i\rangle\right|^2 f(E_i)[1-f(E_f)]\delta[\hbar\omega - (E_f - E_i)] \tag{3.37}$$

where $f(E)$ is the Fermi-Dirac distribution and E_m the energy of state m. The two factors involving the Fermi-Dirac distributions ensure that the Pauli principle is respected, while the delta function ensures energy conservation. From the total absorbed power $P = \hbar\omega \cdot W$ one then obtains an estimate for the real part of the optical conductivity [21]:

$$\sigma_1(\omega, T) = \frac{e^2}{(2\pi m)^2 \hbar\omega} \int d\vec{k} \left|\langle f|\,\hat{p}\,|i\rangle\right|^2 f(\hbar\omega_i, T)[1-f(\hbar\omega_f, T)]\delta[\omega - (\omega_f - \omega_i)] \tag{3.38}$$

Once the real part is known, one typically calculates the imaginary part of the response by making use of Kramers-Kronig relations. The optical conductivity will thus be finite if the excitation energy equals the energy difference between two states, the initial state is occupied and the final state is empty and if the dipole matrix element for this transition is finite. We therefore conclude this section with a brief account of the selection rules that tell us when the dipole matrix element will be finite.

3.3.2 Selection rules

The optical conductivity depends on the finiteness of the dipole matrix element appearing in Eq. (3.38). Figure 3.1 shows a schematic representation of the excitation from an initial state to a final state for which the matrix element for the transition is given by:

$$\hat{M}_{i\to f} = \langle f|\hat{p}|i\rangle \tag{3.39}$$

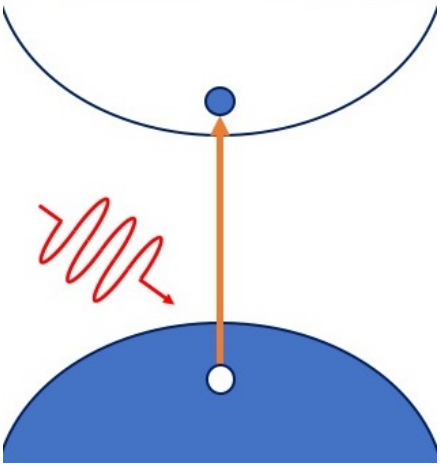

FIGURE 3.1: Schematic illustration of an optically induced transition between initial and final state.

where i and f are initial and a final state as before. The determination of these matrix elements for a gas of atoms is pretty straightforward. In that case we can have some hope to accurately calculate the matrix elements, since the atomic wavefunctions are known to some degree of accuracy and the transitions take place within a single atom or molecule with a well defined set of states and excited states. In solids this becomes a lot more complicated because we should consider a transition from the many-body groundstate wavefunction (blue shaded density

of states in Fig. 3.1) to an excited state of the system. Within the local density approximations to density functional theory presented above, we have some idea of what the groundstate wave function looks like, but the excited states (empty area in Fig. 3.1) cannot be (easily) obtained within DFT. The best we can do to approximately calculate the matrix elements in Eq. (3.39) is to take the occupied wavefunctions as initial states and use the calculated unoccupied wavefunctions to represent the final states.

Although the dipole integral in Eq. (3.39) can be explicitly calculated in DFT, it is not always easy to identify afterwards which states contributed to the optical conductivity. Obviously, optically induced transitions have to obey conservation laws, such as energy, momentum and angular momentum. The first two can be used to distinguish between direct and indirect optical transitions. A direct transition is the equivalent of the 'resonant' transition known from atomic physics. In a direct transition the initial and final state carry the same momentum and the excited state has an energy $\varepsilon_f = \varepsilon_i + \hbar\omega$, where the latter term is the energy carried by the photon. In atomic transitions, the photon momentum is translated into linear motion of the atom as a whole (a so-called recoil). In solids, the photon momentum is typically absorbed by the crystal. This means that the excitation is always inelastic to some extent. However, since the photon momentum is orders of magnitudes smaller than typical electron momenta, one can safely ignore these effects. Indirect transitions are characterized by a large momentum mismatch between the initial and final states. Momentum is conserved by the simultaneous excitation or absorption of phonon excitations. These types of transitions are crucial in explaining spectra of most semiconductors.

The last conservation law involves angular momentum and this is the most complicated one in solids. The spin angular momentum of the photon needs to be absorbed in the transition. The total angular momentum $\vec{J} = \vec{L} + \vec{S}$ of the initial and final states should thus differ by one. In atomic physics this leads to relatively straightforward selection rules (i.e. $p \rightarrow d$ is optically allowed, but not $p \rightarrow p$). In solids the mixed character of the wavefunctions complicate this picture, but sometimes one can still have some hope to identify transitions if DFT predicts large weight on a particular orbital.

3.4 Correlation driven phase transitions and the underlying topological order.

The classification of matter using concepts from topological geometry has become one of the major driving forces behind fundamental research in condensed matter physics. This topic is intimately connected to the theory of quantum phase transitions as we

will show in the following section. Phase transitions on their own are a fascinating topic that have been a fundamental aspect of condensed matter physics since its early history. In the following sections we will briefly introduce the idea behind topological classifications and the relation with quantum phase transitions. We will be mostly interested in phase transitions resulting from the complex interplay of many electronic degrees of freedom. The superconducting phase transition and the cross-over between Fermi liquid and Kondo insulator are examples of such transitions, which are the topic of this thesis. In the second half of this section we provide a brief overview of the experimental signatures of the correlated electron physics underlying these transitions.

3.4.1 Topological classifications.

The concept and description of topology is a rich and very active field in mathematics. It ranges from the description of topological spaces through differentiable functions on manifolds to geometrical properties of surfaces and knots. Geometrical topology and the topological classification of surfaces is perhaps the most easily understandable example that introduces some general concepts from topology that will be used in the rest of this section. The topological classification of surfaces is based around the action of continuous smooth deformations on a surface. For example, the surface of a sphere can be smoothly transformed (deformed) to the surface of a rectangular block or the surface of a simple bowl. To create more complicated shapes requires puncturing the surface. The sphere cannot be deformed to the surface of a doughnut without making a hole in the surface. The sphere and doughnut are therefore topologically different and are distinguishable by a so-called topological invariant, known as the genus g. In this case, the genus is an integer that describes the number of holes through a surface. Surfaces with a different genus cannot be deformed smoothly into each other.

This is one simple example of a much more abstract and purely mathematical framework. In recent years the topological classification of differentiable functions on manifolds has found its way into the field of condensed matter physics as we will now discuss.

3.4.2 The renormalization group approach.

The relation of these concepts to condensed matter physics is not obvious, but the description of the electronic structure of solids has been shown to adhere to a form of topological classification. This classification is based on concepts borrowed from algebraic topology and equally makes use of concepts such as topological invariants and smooth deformations. The application of smooth deformations in physics quite naturally

follows from the renormalization group theory, while the concept of topological invariants was rediscovered by and attributed to Sir Michael Berry [30].

Any physical system can be described quantum mechanically by a Hamiltonian. The eigenfunctions and eigenvalues of such a Hamiltonian are unique and fully determined by some 'tuning' parameters. Wilson's renormalization group theory [31] shows what happens to the solutions (eigenvalues and eigenfunctions) of a model Hamiltonian when its parameters are tuned (flow) from one extreme to another. The renormalization flow leads to the definition of so-called fixed points, which describe the general properties of whole families of Hamiltonians. Such renormalization group flow can be used to define the concept of smooth deformations of Hamiltonians and their 'topological equivalence': if we smoothly deform a Hamiltonian (i.e. by changing a coupling constant), the new model is topologically equivalent if it flows to the same fixed point under renormalization. If it flows to the exact same fixed point, this also implies that under the smooth deformation the wavefunctions and energy spectrum do not change significantly and that observables will follow the same scaling behavior.

A pertinent example relevant to this thesis would be the Kondo-problem [32]:

$$H = \sum_{\mathbf{k},\sigma} \varepsilon_{\mathbf{k}} c^{\dagger}_{\mathbf{k},\sigma} c_{\mathbf{k},\sigma} + J\mathbf{S}(\mathbf{0}) \cdot \mathbf{S} \tag{3.40}$$

where the first term describes a simple tight-binding band of non-interacting electrons and the second term is the so-called Kondo coupling of these electrons to an impurity spin $\mathbf{S}$ (through the spin density $\mathbf{S}(\mathbf{0}) \equiv \sum_{\mathbf{k},\sigma} c^{\dagger}_{\mathbf{k},\sigma} \overline{\sigma}_{\sigma,\sigma'} c_{\mathbf{k},\sigma'}$ where $\overline{\sigma}_{\sigma,\sigma'}$ are Pauli matrices (for more details see chapter 5)). Renormalization group theory explains under which conditions the solutions of a particular Hamiltonian (for a given ε_k and value of J) flow to a certain fixed point. In the case of the Kondo problem there are two fixed points: a Fermi liquid fixed point for $J \leq 0$ and the Kondo singlet fixed point for $J \to \infty$. Obviously, in the absence of the Kondo coupling and at finite density, we end up with a Fermi liquid. The result obtained by Wilson [31] shows that if we add a finite, ferromagnetic interaction this result does not change. However, if the interaction is anti-ferromagnetic the renormalization flow of the coupling diverges to ∞ for any non-zero J and the system forms a Kondo singlet state. The physical result of this analysis is that for a given real metal with anti-ferromagnetic coupling to an impurity, the conduction electrons will always screen the impurity spin at sufficiently low temperature resulting in the Kondo effect. The temperature scale below which this Kondo effect sets in (defining the Kondo temperature), scales with the coupling strength.

3.4.3 The integer quantum Hall effect.

The renormalization group approach has a natural extension to the concept of topological classification, which was first understood from a discussion of the two-dimensional integer quantum Hall state [33, 34]. A thorough discussion of the quantum Hall effect is beyond the scope of this thesis (many good and recent reviews can be found online. An early, pedagogical review can be found in ref. [35]). In the simplest picture, the description of an electron moving in 2 dimensions (2D) under the influence of a magnetic field is given by:

$$H = \frac{\left(\hat{p} - \frac{e}{c}\vec{A}\right)^2}{2m} \tag{3.41}$$

In the Landau gauge, $\vec{A} = By\hat{x}$, this can be shown to be equivalent to:

$$H_B = \frac{\hat{p}_x^2}{2m} + \frac{1}{2}m\omega_c^2\left(\hat{x} - x_0\right)^2 \tag{3.42}$$

where $\omega_c \equiv eB/mc$ is the well-known cyclotron frequency and $x_0 \equiv \hbar k_x/m\omega_c$ is an average 'radius' for the cyclotron orbits (note that x_0 is proportional to B^{-1} as expected). Equation 3.42 is nothing other than a quantum Harmonic oscillator problem and the solutions are well known. In particular, the energy eigenvalues (in this case known as Landau levels) are $\epsilon_n = \hbar\omega_c(n+1/2)$ and to each eigenvalue corresponds a particular (N-particle) eigenfunction. Landau levels come with a large degeneracy N, which depends on the strength of the magnetic field B and the area A of a piece of material:

$$N = \frac{BA}{\left(\frac{hc}{e}\right)} = \frac{\Phi}{2\Phi_0}. \tag{3.43}$$

Here Φ is the total flux and $\Phi_0 = \frac{2e}{hc}$ is the flux quantum, a constant per electron (note: the factor two in the numerator counts spin degeneracy). In solids, the 2D integer quantum Hall effect appears when a gas of electrons is confined to a two-dimensional interface. Experimentally this can be achieved by gating a thin, doped semiconductor such as GaAs, resulting in quantum well states near the surface of the semiconductor [33]. In the absence of a magnetic field, the electrons behave just like a free electron gas, with a Fermi surface and constant density of states (see figure 3.2). When a magnetic field is applied perpendicular to the 2D plane, the eigenvalues and wavefunctions undergo a radical transformation and Landau levels are formed. However, in a given piece of material the total number of electrons is fixed and as a consequence of Eq. (3.43), fewer and fewer Landau levels will become occupied with electrons (see figure 3.2) and the Fermi level will shift from one Landau level to the next. For large ranges of field strengths the Fermi level will actually be in between two Landau levels rendering the

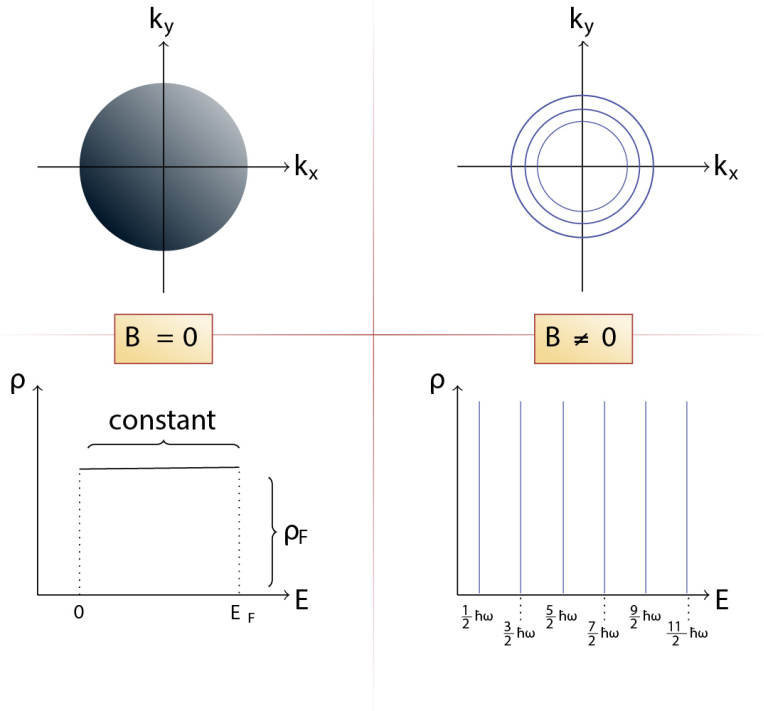

FIGURE 3.2: Left: Fermi surface (top) and density of states (bottom) for a 2D electron gas without applied magnetic field. Right: Landau levels (top) and associated density of states (bottom) in the presence of a magnetic field. Note that in this case the Fermi level depends on the strength of the applied magnetic field.

system insulating. In experimental situations, disorder will broaden the Landau levels in energy (lifting some of the degeneracy) and this will result in small ranges of field strengths where the system becomes metallic.

The implications of the above on physical properties becomes clear if we consider the transport behavior of such two dimensional electron gases. The experiment conducted by von Klitzing and co-workers is relatively simple: take a two dimensional electron gas in a perpendicular magnetic field (see figure 3.3a), apply a voltage along one direction of the electron gas (keeping a constant drain current of 1 μA) and measure the perpendicular Hall voltage that develops. They then apply a gate voltage to control the density of the electron gas, enabling them to tune the occupation of Landau levels starting from zero density. As figure 3.3a shows, the Hall voltage shows clear steps resulting from the quantization of the electron orbits in an applied magnetic field as predicted by the Hamiltonian, Eq. (3.42). At the same time the voltage that is required to keep the drain current constant shows strong fluctuations. From a measurement of the Hall voltage one can define the Hall conductivity as

$$\sigma_{xy} = \frac{j_x}{E_H} = n\frac{eB}{h} \tag{3.44}$$

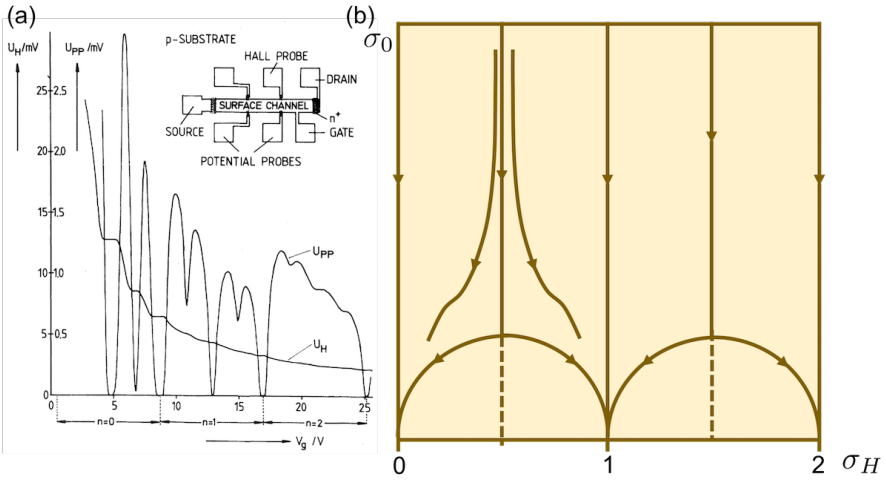

FIGURE 3.3: (a): Original experimental observation of Ref. [33]. In this experiment the gate voltage V_G is swept at constant magnetic field (18 T). As the gate voltage increases the electron density increases and more Landau levels become filled. This results in oscillations in the voltage drop along the Hall bar. The Hall voltage decreases with electron density and shows marked steps at low gate voltages. The inset shows the experimental geometry. (b): Renormalization flow diagram adapted after [36]. The diagram indicates the flow of the longitudinal and Hall conductivity as function of system size. The longitudinal conductivity flows towards zero at a fixed point. Depending on the density, the flow will be to different fixed points that can be distinguished by integer values of the Hall conductivity.

where E_H is the Hall field and j_x the applied current along the perpendicular direction and n is the carrier concentration. A first important step towards understanding the experimental observation of conductance quantization in the QHE is known as Laughlin's argument [37]. According to Laughlin, the Hall conductance will always be quantized in an integer times e^2/h. Laughlin considered a ribbon (see Fig. 3.4a) made up out of a 2D electron gas rolled up on itself. The resulting loop of length L, is periodic along one direction and has a magnetic field pointing outwards, perpendicular to its surface everywhere. In the presence of disorder, δ-function like sets of Landau levels are broadened such that extended states emerge and start to overlap with each other. Laughlin considered the case where the Fermi level was inside the so-called mobility gap (where the density-of-states is small at Fermi level even in the presence of disorder). In this case, the current running along the loop is proportional to the 'adiabatic' derivative of the total electronic energy with respect to the total magnetic flux through the loop [37]:

$$I = c\frac{\partial U}{\partial \phi} = \frac{c}{L}\frac{\partial U}{\partial A} \tag{3.45}$$

where in the last step A denotes the vector potential. Classically, this derivative should be zero, since measurable quantities cannot depend on $\vec{A}$. In quantum mechanics the vector potential plays a different role as can be seen from Eq. (3.41). The Schrödinger equation in the presence of a vector potential $\vec{A}$ remains gauge invariant if we take,

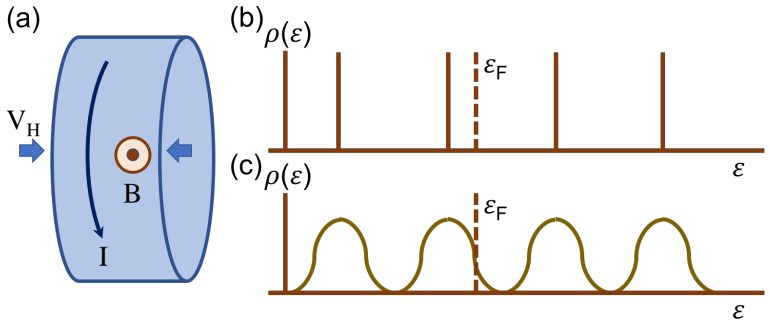

FIGURE 3.4: (a): a 2D electron gas is rolled up into a loop of length L. A magnetic field is applied normal to the surface everywhere and a current is set to flow along the ribbon. A Hall voltage develops between the two edges of the ribbon. (b): the density of states in the absence of disorder represents a series of δ-functions. (c): in the presence of disorder the delta functions become extended and can start to overlap. In both cases (b,c) the Fermi level is indicated by ε_F. The figure is adapted from [37].

$\vec{A} \rightarrow \vec{A} + \nabla\chi$, $\phi \rightarrow \phi - \partial\chi/c\partial t$ and,

$$\psi \rightarrow e^{i\frac{q}{\hbar c}\chi}\psi \tag{3.46}$$

Therefore, if $\vec{A}$ is changed also the phase of the wavefunction must change. Laughlin considered the case where a possible choice for χ would be,

$$\chi = Ax \tag{3.47}$$

where x is along the loop. Such a gauge transformation is however not allowed, unless

$$A = n\frac{hc}{eL} \tag{3.48}$$

since it then winds an integer times 2π around the length of the loop and the wavefunction at $x = 0$ and $x = L$ connect smoothly. The key point is now that the flux penetrating the ring can change only in steps of a single flux quantum, $\Delta\phi = hc/e$, such that the vector potential jumps by 2π. In the absence of disorder and with the Fermi level in between the Landau levels, no states are available in the bulk of the loop. Therefore, if the flux threading the loop is adiabatically changed so that no charges are excited over the bulk gap, it follows that the change in current must be driven by adding electrons at the edges of the loop. Laughlin argued that the resulting change in current is therefore driven by the transfer of n electrons from one edge of the loop to the opposite edge and is given by [37],

$$I = c\frac{neV_H}{\Delta\phi} = \frac{ne^2V_H}{h}. \tag{3.49}$$

Laughlin further showed that this result could be upheld even in the presence of disorder, as long as the Fermi level was in between Landau levels.

Thouless, Kohmoto, Nightingale and den Nijs (TKNN) [34] provided a final, more rigorous explanation based on a topological argument. Their work showed why quantization was upheld even for arbitrary filling. We qualitatively discuss this idea in terms of a renormalization group approach that was developed by Pruisken [36]. Figure 3.3b shows a renormalization group (RG) flow diagram for the quantum Hall effect. The initial number of electrons sets the longitudinal conductance (e.g. the conductance along the same direction along which the initial potential is applied). As the system size is scaled while the number of electrons is kept fixed, the longitudinal conductance flows towards zero, while the perpendicular conductivity (i.e. the Hall conductivity) flows to an integer times the 'von Klitzing constant' (e^2/h). The flow diagram,Fig. 3.3b, shows that there are in fact many distinct fixed points, characterized by an integer n, that each define a distinct ground state. TKNN showed that this integer n is in fact a topological invariant and as a result it has become known as the TKNN invariant. It can take on all integer values and therefore $n \in \mathbb{Z}$. The flow diagram further indicates that the ground state is always insulating ($\sigma_{xx} = 0$). However, in order to move from one insulating ground state to another, the longitudinal conductivity has to become finite, indicating that the gap must briefly close. In the quantum Hall experiment this is indeed observed as an oscillation in the longitudinal voltage (U_{pp} in Fig. 3.3a).

The interpretation of the TKNN integer takes us back to the first paragraph of section 3.4.1. The basic idea proposed in the TKNN work is that each of the QHE groundstates can be described by a generalized Bloch function $u(k_1, k_2)$ that satisfies generalized boundary conditions (k_1 and k_2 are two orthogonal momenta and considered to be good quantum numbers). The function $u(k_1, k_2)$ is an eigenfunction of the Hamiltonian and describes a manifold of solutions in momentum space. TKNN showed that the Hall conductance could be calculated using the Kubo-formula and is given by [34],

$$\sigma_H = \frac{ie^2}{4\pi h} \sum \int d^2r \oint dk_j \int \left(u^* \frac{\partial u}{\partial k_j} - \frac{\partial u^*}{\partial k_j} u \right) \tag{3.50}$$

where the sum runs over the occupied subbands and the integrations are over the unit cells in r and k space respectively. The important point is that the integration over k-space has been converted to a surface integral using Stokes theorem and that its value (for non-overlapping subbands) must be an integer times $4\pi i$. The value of this integer is analogous to the genus defined in section 3.4.1. However, instead of measuring the number of holes in a surface, it measures the number of times the phase of the Bloch wavefunction winds around 2π when the integral in Eq. 3.50 is taken over a closed surface encompassing the first Brillouin zone. The phase winding and its importance

was later expounded by Berry [30] and the surface integral and this particular form of the kernel are nowadays referred to as the Berry curvature of the Bloch functions.

3.4.4 The rise of graphene and topological order.

A few years after the seminal work by TKNN, Haldane constructed a model that demonstrated how the quantum Hall effect could also arise in materials in the absence of an external field [38]. Haldane showed that time-reversal symmetry breaking (such as occurs for magnetically ordered groundstates) could give rise to a QHE without Landau levels. This result demonstrated that it was possible to have topologically distinct ground states in non-interacting electron systems. This work is nowadays considered as a first example of the importance of topological order in physics and Haldane was awarded 1/4 of the 2016 Nobel prize for this contribution. At the time, Haldane considered his toy model "unlikely to be realizable", but the discovery of graphene by Geim and Novoselov [39] rekindled the interest in its unusual quantum Hall effect. At first glance, graphene (a single atomic layer of graphite) appears to be a perfect 2D electron gas. There is however a crucial difference between the dispersion of graphene and the 2D electron gases in semiconductors discussed above. Considering only the $2p_z$ orbital and a hexagonal lattice with 2 carbon atoms per unit cell (also referred to as a honeycomb lattice), the tight binding dispersion can be shown to be:

$$E_k = \varepsilon \pm \gamma_0 \sqrt{3 + 4\cos\left(\frac{\sqrt{3}}{2}k_x a\right)\cos\left(\frac{k_y a}{2}\right) + 2\cos\left(k_y a\right)} \tag{3.51}$$

where ε parametrizes an on-site energy, while γ_0 is a hopping amplitude between neighboring sites. Around the corners of the Brillouin zone (for example at the K-point (k_x, k_y)=$(0, 4\pi/3a)$) the dispersion Eq. (3.51) can be Taylor expanded as:

$$E_k = \varepsilon \pm v|q| \tag{3.52}$$

where $v = (\sqrt{3}/2)a\gamma_0$ and q is the momentum measured relative to the K (K') point of the Brillouin zone. Equation 3.52 is a linear relation between energy and momentum and as a result the second derivative (i.e. the inverse band mass) is zero. The electrons in graphene are therefore said to behave as relativistic or *massless* fermions. In experimentally available graphene the Fermi level sits very close to the so-called charge neutrality point (for which $\varepsilon = 0$), making graphene an almost perfect semi-metal with close to zero free carrier density. By creating field-effect devices similar to the device shown in Fig. 3.3, one can actually tune the chemical potential to the charge neutrality

point. The linear dispersion and the existence of a charge neutrality point are reminiscent of the solution to the famous Dirac equation and the charge neutrality point is often referred to as a Dirac point. These very special properties have a large impact on the transport properties of graphene. In particular, shortly after the initial discovery of graphene the quantum Hall effect was experimentally realized in a graphene flake [40]. The quantization of the linearly dispersing electrons in a magnetic field result in Landau level spectrum that is distinctly different from the solution to Eq. (3.42) and instead reads:

$$\epsilon_n = sgn(n)\sqrt{2e\hbar v^2|n|B} \tag{3.53}$$

The most important distinction with the integer quantum Hall effect is the presence of the n=0 Landau level with ϵ_0=0 as predicted by Haldane [38]. The presence of this n=0 Landau level results in a Hall conductivity that is quantized according to

$$\sigma_{xy} = \pm g_s(n + 1/2)\frac{e^2}{h} \tag{3.54}$$

where g_s is the Landau level degeneracy. The additional factor $e^2/2h$ gives rise to the nomenclature 'half-integer' Hall effect and is an implicit manifestation of a non-trivial Berry phase [40].

Around the same time that the quantum Hall effect in graphene was reported, Gene Mele and Charles Kane came with a radical prediction for a new type of quantum Hall effect in graphene: the quantum spin Hall effect [41]. Kane and Mele started from the same model as Haldane, but with the benefit of new experimental insights and the flurry of theoretical activity at the start of the graphene era they considered a time-reversal conserving perturbation. Their argument was fully grounded in the use of fundamental, discrete symmetries of graphene. In contrast to previous works they sought to construct a Hamiltonian that preserved the fundamental symmetries of graphene (e.g. time-reversal symmetry, inversion symmetry and mirror symmetry about the plane). The only interaction that is allowed under these conditions is the spin-orbit (SO) interaction,

$$V_{SO}(k) = \Delta_{SO}\vec{h}(\vec{k}) \cdot \vec{\sigma} \tag{3.55}$$

with Δ_{SO} the spin-orbit coupling, $\vec{h}(\vec{k})$ the intrinsic spin orbital field and $\vec{\sigma}$ the spin-operators of the conduction electrons. The function $\vec{h}(\vec{k})$ is a complicated function that depends on the crystal structure. Note that under time-reversal $\vec{k} \rightarrow -\vec{k}$ and $\vec{\sigma} \rightarrow -\vec{\sigma}$, hence $\vec{h}(\vec{k}) \rightarrow \vec{h}(-\vec{k})$. This also implies that with inversion symmetry (for which $\vec{h}(\vec{k}) = \vec{h}(-\vec{k})$), the intrinsic SO field must vanish. Kane and Mele showed that for any finite coupling Δ_{SO}, the SO interaction results in a gapped (i.e. insulating) groundstate. The key difference with the work by Haldane is that the spin-orbit interaction not only

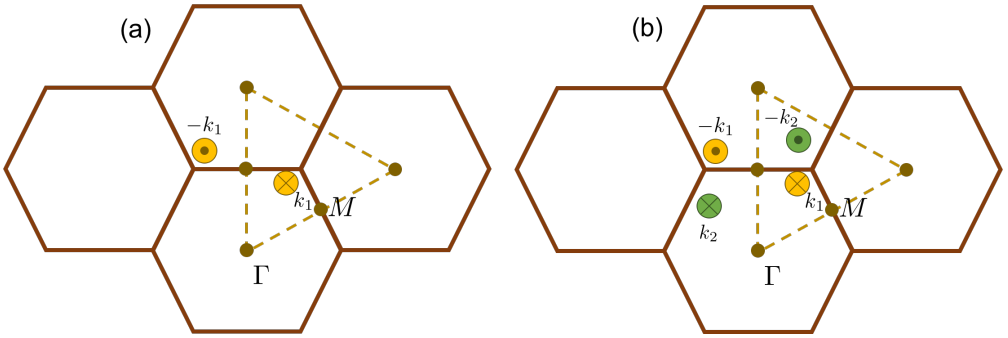

FIGURE 3.5: (a): Brillouin zone boundary of graphene. There are two time-reversal invariant points indicated (Γ and M). The dashed lines form the integration contour for Eq. (3.57). Also indicated are two zeros of the Pfaffian (Eq. (3.58)). The cross and dot indicate the opposite vorticity of the phase of the Pfaffian. (b): the same as in (a), but now with two zeros of the Pfaffian.

preserves time-reversal symmetry, but also that its effect is opposite for spin-up and spin-down electrons resulting in a spin current [41]:

$$\vec{J}_s = \frac{\hbar}{2e}\left(\vec{J}_\uparrow - \vec{J}_\downarrow\right) \tag{3.56}$$

and a corresponding spin Hall conductivity $\sigma_{xy} = e/2\pi$. Applying Laughlin's argument, this spin current must be carried by edge states just as in the normal Hall effect. An explicit calculation for a strip of 2D graphene shows that the bulk of such a strip is gapped as a result of the SO interaction and that there are two edge states traversing the gap [41]. However, the spin dependence introduced by the SO interaction lifts the degeneracy of the spin states resulting in spin-filtered states at each edge (allowing quasi-particles with a certain spin to move in only one direction).

Kane and Mele quickly realized that they had uncovered a new principle that had previously gone unnoticed in condensed matter physics: topological order. In a follow-up paper [42], they showed that the quantum spin Hall phase was in fact distinguishable from an ordinary insulating phase by the introduction of a topological invariant similar to the TKNN invariant introduced above. The TKNN invariant cannot be applied to the case considered by Kane and Mele, as it vanishes in a time-reversal invariant system. Instead, they borrowed ideas from the mathematical framework of knots and bundles to construct a new topological invariant [42],

$$I = \frac{1}{2\pi i}\oint_C d\vec{k}\cdot\nabla_{\vec{k}} log\left[P(\vec{k}) + i\delta\right] \tag{3.57}$$

where the function $P(\vec{k})$ is the so-called Pfaffian,

$$P(\vec{k}) = Pf\left[\left\langle u_i(\vec{k})\right| \Theta \left|u_j(\vec{k})\right\rangle\right] \tag{3.58}$$

Here Θ represents the time reversal operator and the $\left|u_j(\vec{k})\right\rangle$ are Bloch wavefunctions. The action of the Θ operator on these Bloch wavefunctions can be either even or odd and the Pfaffian distinguishes between these two cases. For even wavefunctions the Pfaffian $|P(\vec{k})| = 1$, while for odd wavefunctions $P(\vec{k}) = 0$. Kane and Mele showed that the number of pairs of zeros of $P(\vec{k})$ defines the $\mathbb{Z}_2$ invariant. This is illustrated in Fig. 3.5. In Fig. 3.5a, the Brillouin zone (BZ) of graphene is shown. There are two distinct high symmetry points in the Brillouin zone that are even under time reversal symmetry: the Γ and M point (note that the middle of each vertex of the BZ is an M point). At these points the Bloch wave functions are even with respect to Θ and therefore the Pfaffian at these points is $|P(\vec{k})| = 1$. Depending on the tuning parameters of the Hamiltonian, there can be isolated points where $P(\vec{k}) = 0$. Figs. 3.5a,b show two distinct possibilities: an odd number of pairs (a) and an even number of pairs (b). Note that the zeros come in pairs where the partners have opposite winding direction (vorticity) of the phase of the Pfaffian. As a result of time-reversal invariance the zeros must be at $\vec{k}$ and $-\vec{k}$ and this means that the zeros of Fig. 3.5a cannot be removed by smooth deformation of the Hamiltonian. By changing the tuning parameters of the Hamiltonian these zeros would have to meet at the Γ or M-point, but at these points the Pfaffian is $|P(\vec{k})| = 1$. In contrast, with an even number of pairs (or no pairs at all) the zeros can be eliminated by smoothly deforming the parameters such that k_1 becomes equal to $-k_2$. (see Fig. 3.5b). The contour integral of Eq. (3.57) counts the number of zeros in the Brillouin zone when integrated along the dashed line indicated in Fig. 3.5 and takes on the value 0 or 1 depending on the number of zeros and their vorticity. The situation sketched in Fig. 3.5 is not the real situation for graphene, since the crystal structure imposes C_{3v} symmetry. As a result the only allowed momenta for zeros of the Pfaffian are at the corners (K and K' points) of the Brillouin zone. Kane and Mele showed [42] that the invariant, Eq. (3.57), with or without spin-orbit interaction takes on different values, thus distinguishing the quantum spin Hall state from the normal insulating state.

3.4.5 Topological insulators in two and three dimensions.

The discovery of the quantum spin Hall phase and the subsequent identification of the $\mathbb{Z}_2$ invariant were tied together in further work by Fu and Kane [43], who established the connection between the invariant and the edge states. Working on the problem at the same time, Moore and Balents [44] coined the phrase "topological insulator" to denote a material with a $\mathbb{Z}_2$ invariant different from vacuum and generalized the results of Kane and Mele to three dimensions. Further generalizations [45–47] of the 2D graphene model soon followed, as well as a prediction for a system in which this new state could possibly be observed [48]. The experimental discovery of 2D [49] and 3D [50]

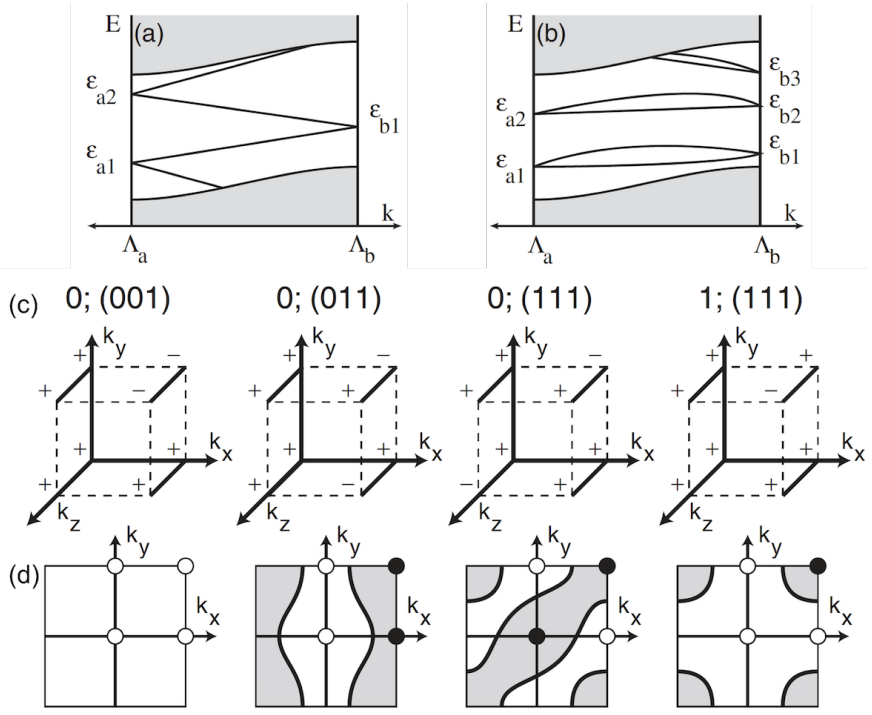

FIGURE 3.6: (a,b): Two possible ways to connect degenerate Kramers pairs across the Brillouin zone corresponding to the two values the $\mathbb{Z}_2$ invariant can take. In (a) there is no way to smoothly deform the Hamiltonian such that a gap opens at the Fermi level. In (b) the edge states can be shifted in energy such that there are no states crossing the Fermi level. Therefore (a) corresponds to the topological insulator case and (b) does not. (c): Some of the possible phases corresponding to specific choices for the invariants (ν_0;ν_1,ν_2,ν_3). The $\pm$ indicate the sign of the δ_i (Eq. 3.59) at the indicated TRIM points. (d) Corresponding Fermi arcs for the phases in (c) projected onto the (001) surface. Figure adapted from [46].

topological insulators marked the beginning of a new era in condensed matter physics where topology has turned into a guiding principle to classify electronic states of matter. With the field blossoming and quickly expanding from condensed matter physics to other fields in physics, a complete overview of the subsequent discoveries is beyond the scope of this thesis. Instead, we will focus on a small corner where topological protection is provided by the symmetries of a 3D cubic crystal structure with inversion symmetry. We refer the reader interested in other aspects of topological insulators to the wide range of available reviews and books that are now available.

Fu, Kane and Mele [46] showed how to generalize the 2D quantum spin Hall (QSH) state to a 3D crystal. For a two dimensional crystal, Laughlin's argument can be used to show that a special quantity, defined as a so-called *time-reversal polarization* (TRP), can take on two distinct values [47]. This then defines a so-called $\mathbb{Z}_2$ invariant that takes on two distinct values (0 or 1, for example) and its value measures whether there is a Kramers degenerate state at the edge of the system. The invariant can be calculated by multiplying the TRP's at the time-reversal invariant momentum points (TRIM-point) in the first Brillouin zone, $\mathbb{Z}_2 = \prod \pi_i$. The TRP for a specific time-reversal invariant

momentum point (TRIM-point) can be calculated from $\pi_i = \prod \delta_k$ where δ_k is given by:

$$\delta_k = \sqrt{det\left[w(\Gamma_k)\right]}/Pf\left[w(\Gamma_k)\right] \tag{3.59}$$

where $Pf(x)$ stands for the Pfaffian and w is the expectation value of the time reversal operator between time reversed eigenfunctions, $w_{ij}\left(\mathbf{k}\right) = \langle u_i\left(-\mathbf{k}\right)|\,\Theta\,|u_j\left(\mathbf{k}\right)\rangle$ This abstract invariant encodes a very beautiful physical picture (Fig. 3.6a,b): it measures how Kramers degenerate pairs at the TRIM points in the Brillouin zone are connected. As Fig. 3.6a,b shows, Kramers pairs can connect from one to another (a) or pairwise (b). In the first case there is no way to smoothly deform the Hamiltonian such that a gap opens at the Fermi level (apart from making a deformation that closes the bulk band gap). In the second case the edge states can be moved in such a way that there are no states crossing the Fermi level.

The abstract method of determining the $\mathbb{Z}_2$ invariant provides the basis for the generalization to three spatial dimensions. However, now there are 8 TRIM-points resulting in 16 possible phases. In ref. [46] it was shown that these configurations can be distinguished by 4 $\mathbb{Z}_2$ invariants. These invariants are grouped together as (ν_0;ν_1,ν_2,ν_3) where the first invariant, ν_0, divides the 16 phases into two groups. When ν_0=0 there are either 0 or 2 Dirac points on the faces of the Brillouin zone (see for example the middle two panels of Fig. 3.6c and 3.6d). Depending on the values of the other invariants it is then possible to have Dirac-like edge states on certain surfaces and these phases therefore resemble a stack of 2D QSH phases. However, in this case any weak periodic potential that doubles the unit cell will fold the Dirac points onto each other and thereby destroy the topological edge states.

The ν_0=1 phases are more interesting as they characterize the situation with an odd number of Dirac points in the Brillouin zone. An example of such a phase is indicated in the right hand-side column of Fig. 3.6c,d. In this case it is not possible to destroy the edge states by a weak periodic perturbation. The invariant ν_0 therefore distinguishes between "weak" (ν_0=0) and "strong" (ν_0=1) topological insulating phases. Apart from weak periodic perturbations, the two dimensional edge states are also protected from localization by disorder. The latter is a consequence of a Berry phase of π that the electron wave function acquires when the electron follows a path encircling the Dirac point [51, 52].

The topological Kondo insulator discussed in chapter 5 is in fact nothing else than a 'strong' topological insulator as described in the previous paragraphs. There are again 4 indices that characterize the phase of the Kondo insulator. The definition of the δ_k's is a bit different. It builds on the observation, developed by Fu and Kane [47], that

for materials with time-reversal and space-inversion symmetry the topological structure is determined by the parity of the occupied wavefunctions at the TRIM-points. Dzero *et al.* [53] used this definition for the specific case of Kondo insulators where *d*- and *f*-bands interact strongly. Since the relevant bands around the Fermi level are made up out of even (d) and odd (f) parity states one can define the δ_k's as:

$$\delta_m = sgn\left(\varepsilon_{k_m} - \varepsilon f\right) \tag{3.60}$$

and the 'strong' invariant $\nu_0 \equiv \prod \delta_m = \pm\ 1$ where m runs over the 8 high symmetry points of the cubic Brillouin zone.

This concludes the discussion of the theory of topological phases of matter. In the next section we explore experimental signatures of topological phases and phase transitions in optical experiments.

3.5 Experimental signatures of topological and correlated electrons.

In this section I will briefly discuss the limitations of optical spectroscopy when it comes to investigating the edge states of 2D or 3D topological insulators. This will be followed by a discussion of the areas where optical spectroscopy is a much more powerful tool: the exploration of phase transitions in correlated electron systems.

3.5.1 Edge states in optical experiments?

The key feature that distinguishes topologically non-trivial from trivial states is the presence of gapless edge states as discussed in the previous sections. The breakthrough experiments that led to the blossoming of topology in condensed matter physics were angle resolved photoemission spectroscopy (ARPES) experiments [50]. Since these first experiments many materials have been discovered that feature Dirac like surface states. In Fig. 3.7 we show a typical ARPES spectrum displaying the surface states in the TI material Bi_2Se_3 (taken from Ref. [54]). Indicated with dashed, yellow lines are the bulk energy bands. Two linearly dispersing states connect the valence band with the (partially occupied) conduction band, crossing each other at a Dirac point in the centre of the Brillouin zone, 450 meV below the Fermi energy. Quantum well states resulting from a quantization of the bulk bands in the strongly band-bending potential near the crystal surface [55] are clearly visible below both the conduction and valence bands.

ARPES is the key identifier when it comes to establishing the topological nature of a material. The application perspective for topological materials is more towards the interesting electro-magnetic properties that are believed to emerge associated with twists in the electronic structure [56–60]. Despite the many predictions, optical spectroscopy studies reporting signatures of the topological surface states [61, 62] are far and few between. Instead, most works [63–65] report negative or indirect results. So, why does optical spectroscopy fail to detect edge states when ARPES tells us clearly they are there?

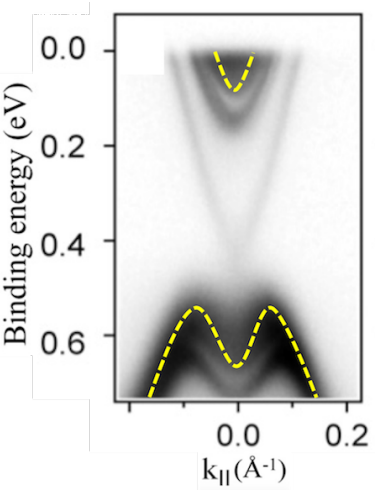

FIGURE 3.7: ARPES spectrum of Bi_2Se_3. The surface projected bulk bands are indicated with dashed, yellow lines. The Dirac point sits approximately 450 meV below the Fermi energy. Also clearly visible are 'quantized' bulk bands split of from the main bulk bands. Adapted from ref. [54].

The answer to this question is important, because in chapter 5 I will discuss the optical properties of SmB_6. In this topological Kondo insulator a gap opens at the Fermi level and surface states are supposed to form inside the hybridization gap. The gap that forms at the Fermi level is of the order of 10 - 20 meV and that poses a real problem for ARPES experiments to resolve the surface states (see Ch. 5 for further details). After many inconclusive ARPES reports, the scientific community is looking for other means to detect signatures of the surface states.

The simple reason why optical experiments have a hard time detecting surface states is simply a 'numbers' game. As Eq. 3.18 shows, the optical response of free charge carriers is proportional to $\omega_p^2 = 4\pi ne^2/m$. In other words, directly proportional to the free charge carrier density. Despite their name, even the most insulating topological insulators are lightly doped semiconductors. Most of the materials discovered so far are small bandgap, thermoelectric materials with relatively complicated crystal structures. In such materials crystallographic defects form relatively easily and impurities are an important factor in determining the true bulk doping [66]. Indeed, Fig. 3.7 suggests that the bulk of Bi_2Se_3 is doped with n-type carriers since the Fermi level appears to sit in the bulk conduction band (note that due to band-bending near the crystal surface, care has to be taken in making definitive statements about the bulk doping from ARPES experiments [54]). Importantly, optical spectroscopy is a bulk probe with a probing depth up to microns. The response measured in an optical experiment is therefore always a combination of both bulk and surface conduction. To answer the 'numbers' question is then simply a matter of comparing the bulk and surface carrier densities. This is somewhat complicated by the fact that the surface states are 2D in nature and its

free carrier concentration is given per unit area. To compare the two we must therefore make a small approximation. First we compute the relation between the bulk and surface carrier density. We assume that the bulk Fermi surface is approximately spherical so that we obtain a relation between the bulk carrier density and E_F,

$$E_F = \frac{\hbar^2}{2m}\left(3\pi^2 N_{BD}\right)^{2/3}, \tag{3.61}$$

which holds for a 3D Fermi gas. This should be compared to the relation between E_F and the surface density for massless Dirac like states:

$$E_F = \hbar v_F \left(4\pi N_{SD}\right)^{1/2}, \tag{3.62}$$

Figure 3.8 shows the resulting relation between N_{BD} and N_{SD} based on the ARPES data reported in ref. [54]. The typical carrier densities reported for Bi-based TI's is on the order of $10^{12}/\mathrm{cm}^2$, which corresponds with a bulk carrier density of approximately $10^{18}/\mathrm{cm}^3$. However, one should not forget that the surface states are highly localized to the surface. Clear estimates for their extent into the bulk are not precisely known, but ARPES experiments on thin films report that the surface states interact when the film is less than 5 quintuple layers (QL) thick [67]. This places a rough bound of 2.5 QL on the extent of the surface states, corresponding to a thickness of approximately 2.5 nm. The real surface state carrier density should therefore be corrected for this factor and gives a 'bulk' surface carrier density of order 10^{11}. This should be compared to estimates of the bulk carrier density in the $Bi_{2-x}Sb_xTe_{3-y}Se_y$ family of materials, which depends strongly on crystal quality [68] and varies between 10^{15}-$10^{20}/\mathrm{cm}^3$. This informs us that the ratio between bulk and surface conduction is larger than 10^4 in the best case. Since the optical conductivity is directly proportional to the carrier density, we can safely estimate that a direct observation of the surface states through a measurement of the absolute value of the optical conductivity will probably always be below the detection limit in optical experiments.

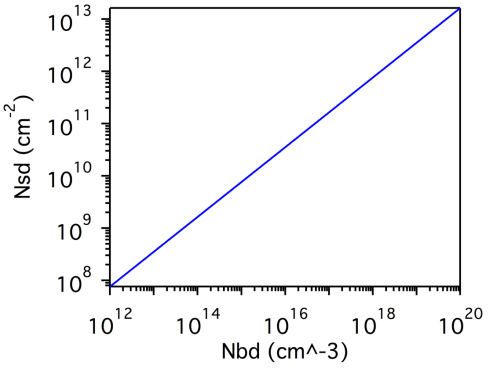

FIGURE 3.8: Calculation of the relation between bulk and surface carrier density based on a fit to measured ARPES dispersions.

3.5.2 Probing correlated electrons with optical spectroscopy.

In the first few sections of this chapter we discussed the classical response of a gas of non-interacting charges and subsequently explained how the electronic bandstructure of solids gives rise to modifications of this simple picture. The simple picture based on Fermi's golden rule does however not include the effects of interactions between the electrons, assuming instead that upon excitation the electronic structure does not 'change'. This picture works well for a simple metal such as copper, but not for a large class of materials dubbed 'correlated electron systems'. In such materials the perturbation of the electron system by creating an electron-hole pair subtly, but significantly, alters the entire many-body state. In chapter 4 I will explicitly show how the optical response is altered as a result of interactions. Here I will briefly discuss how optical spectroscopy can be used to study interacting electron systems. I will do this based on two 'observables' that can be derived from a measurement of the optical conductivity.

Looking back to Eq. 3.18 one notes that the optical conductivity of the non-interacting system is characterized by three numbers: (i) the free charge carrier density, (ii) the scattering rate and (iii) the quasi-particle mass. This gives a frequency dependence that is essentially ω^2. How will this change if we consider a non-interacting gas? This question is explicitly answered in chapter 4, but without any further input it is likely that interactions will not change the carrier density. The most obvious change will be observable as a change in the frequency dependence of the optical response. This cannot, however, be changed randomly: the real and imaginary part of the optical conductivity still need to obey Kramers-Kronig relations.

Without delving into the details, the changes in the frequency dependence of the optical conductivity are best captured by assuming that in the interacting case the scattering rate and effective mass become frequency dependent [69]. The complex-valued free charge optical conductivity can then be written as

$$\sigma(\omega,T) = \sigma_1(\omega,T) + i\sigma_2(\omega,T) = \frac{i\omega_p^2}{4\pi}\frac{1}{\omega + M(\omega,T)}, \tag{3.63}$$

where $\omega_p^2 = 4\pi ne^2/m$ is the plasma frequency and $M(\omega,T) = M_1(\omega,T) + iM_2(\omega,T)$ is the complex memory function. For a simple Drude metal $M(\omega,T) = i\Gamma_D$ is frequency independent, while interactions beyond simple impurity scattering introduce a frequency and temperature dependence. In the latter case Eq. (3.63) is referred to as the extended Drude model.

Another, more convenient, way of expressing the extended Drude model is through the optical scattering rate and optical mass:

$$\frac{1}{\tau(\omega)} = \frac{\omega_p^2}{\omega} \frac{\epsilon_2(\omega)}{[\epsilon_{\infty,IR} - \epsilon_1(\omega)]^2 + \epsilon_2^2(\omega)} \tag{3.64}$$

and

$$\frac{m(\omega)}{m_b} = \frac{\omega_p^2}{\omega^2} \frac{\epsilon_{\infty,IR} - \epsilon_1(\omega)}{[\epsilon_{\infty,IR} - \epsilon_1(\omega)]^2 + \epsilon_2^2(\omega)}. \tag{3.65}$$

where we have chosen to express the scattering rate and mass in terms of the dielectric response, highlighting the importance of the interband response, $\epsilon_{\infty,IR}$. Equations 3.64 and 3.65 provide a 'simple' method to determine the impact of interactions on the optical response. If the material under study is a simple metal a simple inversion of the measured optical conductivity should give an approximately frequency independent scattering rate and effective mass. On the other hand, the frequency dependence and the energy range over which this deviates from the Drude result provide a direct measure of the impact of interactions on the electrons in the solid. This approach has been widely used in the study of the cuprate high T_c superconductors and other correlated materials (see Ref. [3] for an overview).

There is an important caveat to keep in mind when making use of the extended Drude model to study departures from the Drude model. The caveat is that one has to exclude frequency dependencies arising from other sources. An almost trivial example, which has been neglected by many, is that low energy interband transitions will equally well change the frequency dependence. As discussed extensively in chapter 4, the extended Drude model does not allow for an unambiguous separation of the intra- and interband response. Even when the intra- and interband responses are well separated in energy, as is the case in the cuprate superconductors, Eq.'s 3.64 and 3.65 show that their (frequency independent) contribution, parameterized by $\epsilon_{\infty,IR}$, should be taken into account.

The second observable that allows us to investigate the impact of correlations, particularly across phase transitions, is the optical spectral weight. The spectral weight, or sum rule, is a measure of the total charge in the material and is therefore not expected to change. The sum rule is defined as:

$$SW(\omega, T) = \int_0^\infty \sigma_1(\omega, T) d\omega \tag{3.66}$$

For the simple Drude model of Eq. 3.18, it is easy to check that this integral evaluates to $\omega_p^2/8$ and is therefore directly proportional to the charge density. When the optical conductivity takes on a more complex form, the integral in Eq. 3.66 remains a temperature independent constant and that provides the basis for its usefulness. Since in

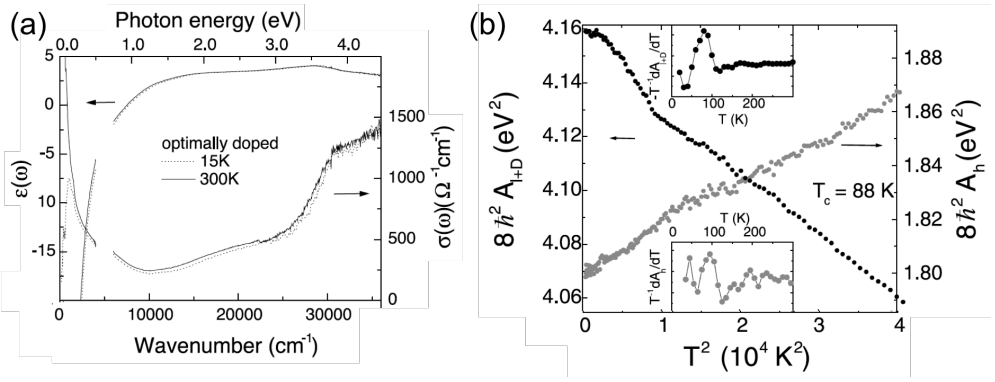

FIGURE 3.9: (a): optical conductivity and dielectric function of optimally doped $Bi_2Sr_2CaCu_2O_{7+\delta}$ at two temperatures. The critical temperature of this material is 88 K. Note the large differences in the optical response at low energy. The difference in the areas of these two curves is the spectral weight loss recovered in the zero frequency δ-function. (b) Partial sum rules A_{L+D} and A_H (explained in the text). Images adapted from ref. [72]

practice we cannot integrate from zero to infinite frequency, we are always bound to evaluate so-called partial sum-rules. These partial sum rules do not immediately give information on interactions, but they can if the spectral weight at different temperatures is compared.

One famous example of a partial sum-rule is known as the f-sum rule or Ferrel-Glover-Tinkham sum rule [70, 71]. This sum rule applies explicitly to superconductors and allows for a determination of the fraction of electrons that become superconducting at the critical temperature. It states:

$$\int_{0+}^{\infty} [\sigma_{1,NS}(\omega,T) - \sigma_{1,SS}(\omega,T)]\, d\omega = \frac{\pi n_S e^2}{2m} \tag{3.67}$$

where $\sigma_{1,NS}$ is the normal state, $\sigma_{1,SS}$ the superconducting state conductivity and n_S the fraction of superconducting electrons. Note that the integrals start at 0+ and in principal should be integrated to as high a frequency as possible. The sum rule states that the spectral weight lost at *finite* frequency when a material becomes superconducting, is recovered in a (collisionless) superfluid condensate at *zero* frequency (the perfect diamagnetic response).

A recent example of the application of this sum rule was reported in Ref. [72], the main result of which is shown in Fig. 3.9. Panel 3.9a shows the optical conductivity of an optimally doped high-T_c cuprate superconductor in the normal (300 K, full curve) and superconducting (15 K, dashed lines) state. At low energy (< 0.25 eV) the 15 K data is clearly below the 300 K curve, indicating a loss of conductivity or spectral weight (area of $\sigma_1(\omega,T)$) at these frequencies. Since the dashed curve is always below the full curve, this spectral weight is not recovered in the measured experimental range. The

loss is a result of the electronic reorganization that takes place when the material enters the superconducting state. First of all, a gap of size 2Δ opens at the Fermi level. In a 'clean' superconductor at zero temperature, this gap opening would result in a complete removal of spectral weight below 2Δ. At finite temperature, there is some conductivity expected below the gap edge as a result of thermal excitation of Cooper pairs. In this particular case a lot more conductivity is visible. This is a result of the $d-wave$ gap that characterizes the superconducting state in these materials. Nevertheless, a significant amount of spectral weight appears to be lost and this weight is transferred to a (non-visible) superfluid condensate at zero frequency. This condensate is not accessible in measurements of the optical conductivity (we note that as a consequence of the Kramers-Kronig relations, the dominant frequency behavior of $\epsilon_1(\omega)$ is changed from ω^{-1} to ω^{-2} and this can be measured [73]). As panel 3.9b shows, the changes in spectral weight are continuous as a function of temperature down to the critical temperature, T_c. The functions A_{L+D} and A_H are defined as follows. Firstly, the total measured integrated spectral weight is defined as A_L+A_H:

$$SW(T) = \int_{\Omega_0}^{\Omega_L} \sigma_1(\omega, T)d\omega + \int_{\Omega_L}^{\Omega_H} \sigma_1(\omega, T)d\omega \tag{3.68}$$

Secondly, the zero frequency spectral weight is defined as:

$$D(T) = SW(T) - SW(300K) \tag{3.69}$$

Figure 3.9b shows the functions,

$$A_{L+D}(T) = D(T) + \int_{\Omega_0}^{\Omega_L} \sigma_1(\omega, T)d\omega \tag{3.70}$$

and

$$A_H(T) = \int_{\Omega_L}^{\Omega_H} \sigma_1(\omega, T)d\omega \tag{3.71}$$

Equation 3.70 is integrated in [72] up to $\Omega_L = 1.25$ eV. As Fig. 3.9a shows this corresponds to the minimum in the optical conductivity and is taken as the separatrix between free and interband responses. For temperatures above T_c, the spectral weight decreases quadratically with temperature, which is a direct consequence of the temperature dependence of the scattering rate.

Since $A_{L+D}(T)$ includes the zero frequency δ-function, one expects no significant change at the critical temperature. The remarkable observation made in Ref. [72] is that at the critical temperature $A_{L+D}(T)$ shows a sudden upturn and increases faster than expected from the normal state trend. The authors of Ref. [72] subsequently point out that this additional spectral weight is removed in the visible range of the spectrum

by calculating $A_H(T)$ with cutoff frequencies $\Omega_L = 1.25$ eV and $\Omega_H = 2.5$ eV. In this energy range the optical conductivity shows a broad structure that can only be an interband transition. These structures are believed to arise from transitions between the charge transfer bands situated well away from the Fermi level (approximately 1 eV below and above the Fermi level). These experiments have been performed with remarkable accuracy, allowing the authors to conclusively demonstrate that spectral weight is transferred from the visible part of the spectrum to the low energy part of the spectrum. This is an indirect demonstration that a reorganization of the electronic structure on the scale of the Coulomb interaction (U$\approx$ 2-4 eV) takes place in these materials and a signature of the unconventional nature of the superconducting state.

In Chapter 5 I will use a similar argument to show that spectral weight in SmB_6 is transferred over energy scales associated with the Coulomb energy. In this case a transition from a bad metal to a Kondo insulating state takes place and there is no δ-function to be detected. Spectral weight that is removed below the energy gap is instead expected to be recovered in the energy range just above the gap edge. I will use partial sum rules in a similar way as discussed here to show that spectral weight is lost in the entire measured energy range. This spectral weight is likely recovered in an interband transition associated with the f-level multiplet.

Chapter 4

Fermi liquid like groundstate in an iron-pnictide superconductor.

4.1 Introduction.

Strong electronic correlations and Mott physics have played an important role in shaping our understanding of high-T_c superconductivity (HTSC) [74]. With the discovery of the iron-pnictide family of HTSCs, a new playground to study correlation effects has emerged [75]. Unlike the cuprate HTSC, the pnictides are properly classified as moderately correlated semi-metals [76]. By studying their normal state properties a new picture has started to emerge [77], where intra-atomic exchange processes (Hund's coupling) govern the degree of correlation effects. In the resulting "Hund's metal" state [78], Hund's coupling reduces the propensity towards a strongly correlated Mott insulating state, while simultaneously reducing the coherence temperature below which Fermi liquid (FL) properties emerge. A strong dependence of the nature of this Hund's metal state on orbital filling has been found, providing a natural explanation for the differences between hole- and electron-doped pnictides [75, 79]. Recently, Werner *et al.* showed [80] that the combined effect of dynamic screening (manifested through a single particle self-energy, $\Sigma(\omega, T)$) and orbital occupancy results in a Fermi-liquid like state in electron-doped pnictides, while a spin-freezing transition separates an incoherent metal regime from the FL regime in hole-doped materials (for a more extensive review of the role of Hund's coupling in the iron-pnictides, see Ref. [75]). A clear experimental identification of both these regimes is currently lacking. In this chapter I provide direct experimental confirmation of the Fermi liquid state in the electron-doped case. Before turning to my results, I will provide a brief introduction to the iron-pnictide superconductors. I then introduce the optical data measured on two single crystals grown in Amsterdam.

Making use of the high temperature stability of the cryostat, I present a novel way to display the temperature and frequency dependence of the optical response. Model calculations of the optical response of a Fermi liquid display remarkable agreement with the experimental results and provide a strong indication that the normal state of the investigated single crystals is indeed Fermi liquid like.

4.2 Iron-pnictide superconductivity.

4.2.1 Discovery of a new family of high temperature superconductors.

One of the key topics driving research in the field of condensed matter physics has been superconductivity. Superconductivity is the principal example of the exceptional behavior that electrons display under the influence of the rules of quantum mechanics. Indeed, superconductivity is a macroscopic manifestation of the effects of quantum statistics on charged, fermionic particles. First explained by Bardeen, Cooper and Schrieffer, the theory of superconductivity has developed into a quantitative framework that explains global properties of superconductors (e.g. the critical temperature and superconducting gap size). The framework is based on the so-called Migdal-Eliashberg theory of electron-phonon driven superconductivity and describes the properties of most elemental superconductors.

Initially, it was believed that the critical temperature was limited to a maximum of about 40 degrees Kelvin. The argument was based on the observation by Cohen and Anderson [81] that the dielectric function posed constraints on the stability (and thus existence) of crystals. These arguments were later partially refuted by Dolgov and Maksimov [82], but the dispute ended abruptly in 1986. In that year Bednorz and Mueller announced they had discovered a new type of superconductor with an unusually high critical temperature of 35 K [83]. Albeit the highest critical temperature to date, T_c was still within the bound proposed by Anderson. This all changed a few months later when the discovery of superconductivity was announced in $YBa_2Cu_3O_{7-\delta}$ with a critical temperature of 93 K, well above the boiling point of liquid nitrogen [84]. This work led to the discovery of a whole family of materials with high transition temperatures nowadays colloquially referred to as 'the cuprates'. It quickly became clear that these materials did not fit well within the paradigm of superconductivity mediated by the electron-phonon interaction. Several aspects (other than the unusually high T_c) hinted at a new mechanism underlying the unusual properties of these materials. Among these are the strongly correlated metallic state from which the superconductor forms and the *d*-wave pairing symmetry of the order parameter, or superconducting gap. To this date

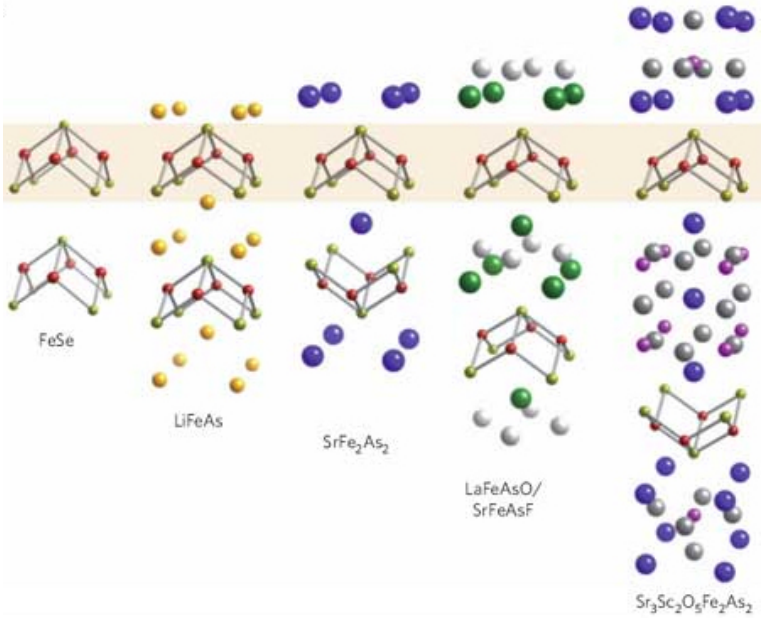

FIGURE 4.1: Crystal structures of the different members of the iron-pnictide superconductors with increasing structural complexity from left to right. The yellow box highlights the commonality between these different structures: the Fe-As plane. Image adapted from [86].

these aspects have eluded a thorough theoretical treatment and the physics of high T_c's remains at the forefront of condensed matter research.

The discovery of a second family of high T_c superconductors took a little more than twenty years. In 2008, Hideo Hosono and his group announced that they had discovered a new superconductor in a so-called oxy-pnictide compound, $La[O_{1-x}F_x]FeAs$ [85] with a critical temperature of $T_c \approx 26$ K. The announcement resulted in a flurry of papers reporting superconductivity in several closely related materials, now referred to as the family of iron-pnictides. In the following sections I will show that the various members, like the cuprates, have some commonalities in their crystal structure and electronic properties, which likely hold the key to the unconventional superconducting state and high critical temperature.

4.2.2 The versatility of the iron-pnictide crystal structure.

There are various crystal structures that belong to the family of iron-pnictide superconductors. An overview is given in Fig. 4.1, which is adapted from Ref. [86]. Within the groups of individual crystal structures, several materials typically can be found that display superconductivity or some other form of electronic order. The chemical composition of the various structures is used as shorthand to distinguish them. Examples are '11' for the FeSe structure and related compounds, 'Li-111' for LiFeAs or 'Na-111' for NaFeAs. In this thesis we will only be concerned with the '122' crystal structure and

the Ba-122 crystal structure in particular. After the original discovery by the Hosono group, it quickly became clear that the electronic properties were largely determined by so-called iron-arsenide planes (see below). With this idea in mind the focus shifted to other compounds featuring FeAs planes and $BaFe_2As_2$ was the first material discovered to be also superconducting [5]. This discovery established the importance of the FeAs planes and resulted in the wealth of new superconducting materials displayed in Fig. 4.1. Despite the wealth of possible materials to study, the $BaFe_2As_2$ family remains the most widely studied compound. The main reason for this is the relatively simple crystal structure and necessary growth conditions. The thermodynamic phase diagram for this compound is relatively simple and this enables the growth of large, homogeneous single crystals. Moreover, the electronic properties can be tuned with a large variety of different methods (chemical substitution, pressure etc.) enabling the study of superconductivity in this material from several different angles.

The crystal structure of Ba-122 is shown in Fig. 4.2, together with a top view of the FeAs plane. The tuning of electronic properties can be achieved through chemical substitution on each of the atomic sites in the unit cell. For example, Ba can be partially replaced by K resulting in an effective 'hole'-doping (i.e. a lowering of the chemical potential with respect to the bandstructure.). Electron doping (raising the chemical potential) can be achieved by Co substitution, while chemical pressure (no change in chemical potential) can be achieved by substitution of As with P. The bands dominating the electronic structure near the Fermi level mostly derive from Fe $3d$ states with some admixture of As $4p$ states. In this thesis we will focus on electron doped Ba-122. The relevant substitution to achieve electron doping is by replacing Fe with a small percentage of Co (Co atoms are indicated in Fig. 4.2b in green). The electronic properties strongly depend on this substitution as is clear from Fig. 4.2c. In figure 4.2c, a phase diagram has been constructed based on measurements performed on a series of single crystals with increasing Co concentration. The electronic phases are determined by transport (resistivity and susceptibility) experiments, which were initially performed by Mr. R. Huisman on crystals grown by Dr. Yingkai Huang in Amsterdam [87].

The parent compound Ba-122 is an anti-ferromagnetic (AFM) metal at low temperature. The anti-ferromagnetic order is destroyed with increasing temperature by the excitation of spin waves, resulting in a phase transition to a paramagnetic state at 130 K. This transition is accompanied by a structural transition from orthorhombic to tetragonal. As some of the Fe is substituted by Co, both transition temperatures decrease until the AFM phase is completely suppressed at a Co concentration of approximately 12 %. The exact doping where this happens is however obscured by the emergence around 6 % doping of a superconducting phase. With increasing Co substitution the critical

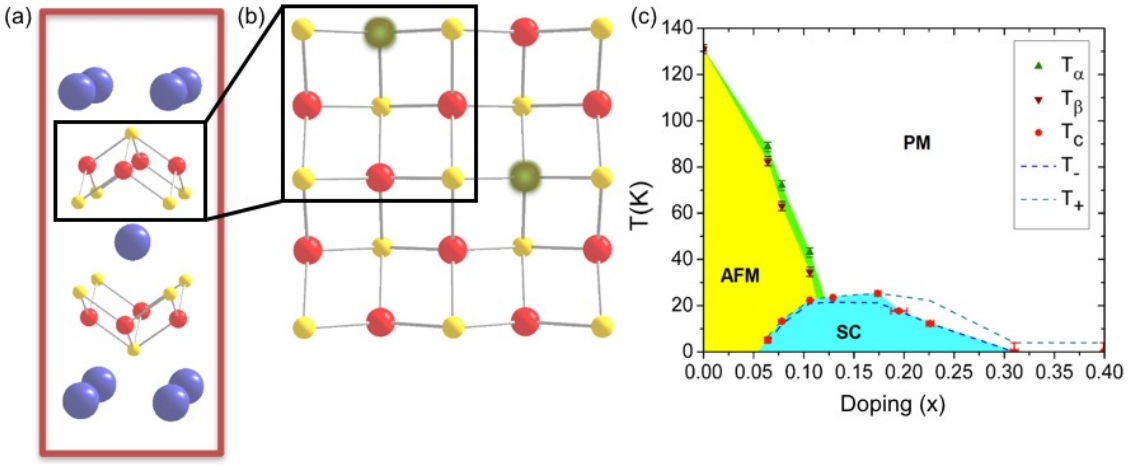

FIGURE 4.2: (a): Prototypical 122 crystal structure. Red and yellow balls represent the Fe and As ions, respectively. Blue represent Ba ions. (b): top view of the FeAs plane. Also indicated are a few green balls where Co atoms are substituted. (c): phase diagram determined by measuring transition temperatures [87]. Three different transitions are observed: (i) structural (T_α), (ii) magnetic (T_β) and (iii) superconducting (T_c). These transitions separate the anti-ferromagnetic metal (AFM) from the superconducting (SC) and paramagnetic metal (PM) phases.

temperature rises, reaching a maximum of approximately 25 K at a Co concentration of 17 %.

4.2.3 General features of the electronic structure of iron-pnictides.

In the early days of iron-pnictide research it was speculated that these materials could shed new light on the long-standing problem of high T_c superconductivity in the cuprates. This idea was quickly abandoned once the basic features of the electronic structure became clear [88]. At first glance the basic crystallographic building blocks of the iron-pnictides and cuprates are very similar. In the former, conducting Fe-As layers are separated from each other by an 'insulating' Ba layer, while in the cuprates Cu-O planes are decoupled by (more complicated) oxide layers. In both cases $3d$ transition metal ions (Fe and Cu) form an approximately square lattice where the bond between individual transition metal ions is through an anion (As or O, respectively). In the cuprates this Cu-O network is fundamental in determining its overall electronic features, resulting in the formation of a so-called charge transfer insulator [89]. In contrast, the overall electronic structure of the iron-pnictides seems to be mostly determined by the Fe square lattice with only a minor role for the As anions (although there are reports that attribute an important role to the anions [90]). The difference is a result of a small buckling of the Fe-As plane by which As anions are alternatingly placed slightly above and below the Fe layer (see Fig. 4.2a). This buckling results in a doubling of the unit cell and, consequently, a folding of electronic bands in the Brillouin zone.

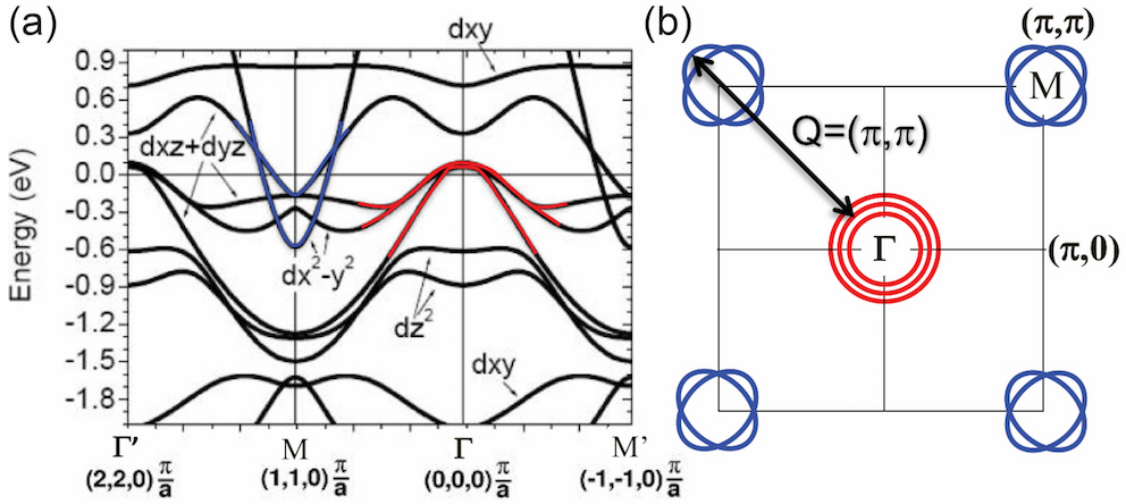

FIGURE 4.3: (a): Bandstructure for $BaFe_2As_2$ calculated within the GGA approximation to DFT. The hole-like bands around the Γ-point (red) have mostly $d_{xz/yz}$ character, while the electron-like bands at the M-point (blue) have a mostly $d_{x^2-y^2}$ character. Panel adapted from ref. [91]. (b): schematic representation of the Fermi surface sheets in the Brillouin zone.

The band structure for $BaFe_2As_2$ has been calculated using density functional theory (DFT) by many authors. In Fig. 4.3 we show calculations from Ref. [91]. These calculations show that the main bands around the Fermi level derive from the Fe $3d$-orbitals with a strong variation of weights of the different $3d$-orbitals throughout the Brillouin zone. Around the Γ-point three hole like bands are found (indicated in red) and two electron like pockets around the M-point of the Brillouin zone (indicated in blue). A schematic picture of the resulting Fermi surfaces is shown in Fig. 4.3b. The placement and shapes predicted by DFT calculations lend themselves perfectly for a scenario where superconductivity is a result of pairing mediated through anti-ferromagnetic fluctuations [92]. The spin susceptibility associated with anti-ferromagnetic spin waves peaks at a wave vector of (π,π) and as indicated in Fig. 4.3b such a wavevector provides a good 'nesting' of the electron and hole like Fermi surfaces. Despite the early prediction that this could result in an instability of the normal state, no conclusive evidence for this scenario has been presented.

The overall electronic structure as measured in angle resolved photoemission spectroscopy (ARPES) experiments seems to match quite well with the band structure predicted by DFT after an overall scaling of the bandwidth is taken into account. An example of a typical intensity distribution map, $I(k, E)$, is shown in Fig. 4.4a. Indeed a hole like band is observed around the Γ-point, while an electron-like band is observed around the M-point in the Brillouin zone (at $\sqrt{2}\pi/a$). Also shown is a 10-orbital tight binding model [93], with parameters optimized to match the measured band structure. Compared to the DFT calculations the overall bandwidth of the tight-binding bands

had to be renormalized by a factor of approximately 1.5. This renormalization has been taken as evidence that this material is moderately correlated with the renormalization resulting from electron-electron interactions [94], a conclusion similar to the one obtained based on optical spectroscopy experiments [76].

The measured Fermi surface is shown in Fig. 4.4b and also agrees well with the calculated Fermi surface. There is however one crucial difference with the predicted Fermi surface: in Fig. 4.4b an additional Fermi surface sheet is clearly visible around the X-point of the Brillouin zone. The origin of this additional Fermi surface sheet turns out to point to an important problem when it comes to the interpretation of ARPES experiments. It was first pointed out by Massee *et al.* that the cleaved surface of Ba-122 crystals as observed by scanning tunneling microscopy showed signs of surface reconstructions [95]. This observation was later confirmed and completely quantified by van Heumen *et al.* using low energy electron diffraction (LEED) experiments [96]. These authors determined the surface crystal structure from their LEED experiments and used this as input for DFT slab calculations. They observed that there are two different possible cleavage surfaces, each characterized by a different long range ordering of the 1/2 Ba layer that remains at the surface after a crystal is cleaved. In particular, they showed that cleaving results in 2×1 and $\sqrt{2} \times \sqrt{2}$ reconstructions. Based on the refined surface crystallographic structure, DFT slab calculations then predict the emergence of additional Fermi surface sheets around the X-point in the Brillouin zone. This additional Fermi surface sheet arises from Ba derived states and it was shown in Ref. [96] that there are in fact many surface bands that overlap with the bulk bands. This provides a natural explanation for the relatively broad energy bands observed in the ARPES $I(k, E)$ map of Fig. 4.4a: rather than a being a single band there are in fact several overlapping bands, closely spaced in energy and momentum, that appear as a single band with a large scattering rate. This rules out a more detailed analysis of ARPES line shapes of the entire family of M122 iron-pnictide superconductors (M=Ca, Sr, Ba) that could provide indications of electron-electron correlation effects. Similar surface reconstruction effects have also been observed for the 1111 family of materials [97] and this seemed to make ARPES a very ineffective tool for the study of electron-electron correlations in the pnictides. However, the 11 and 111 families turn out to provide a good cleavage surface and provide important information on the impact of correlations on the electronic structure of the iron-pnictides [98, 99].

4.2.4 Signatures of Fermi liquid behavior in the optical response.

Before discussing the experimental results, I will first describe how optical experiments can be used to detect signatures of (non-) Fermi liquids. As was discussed in Ch.

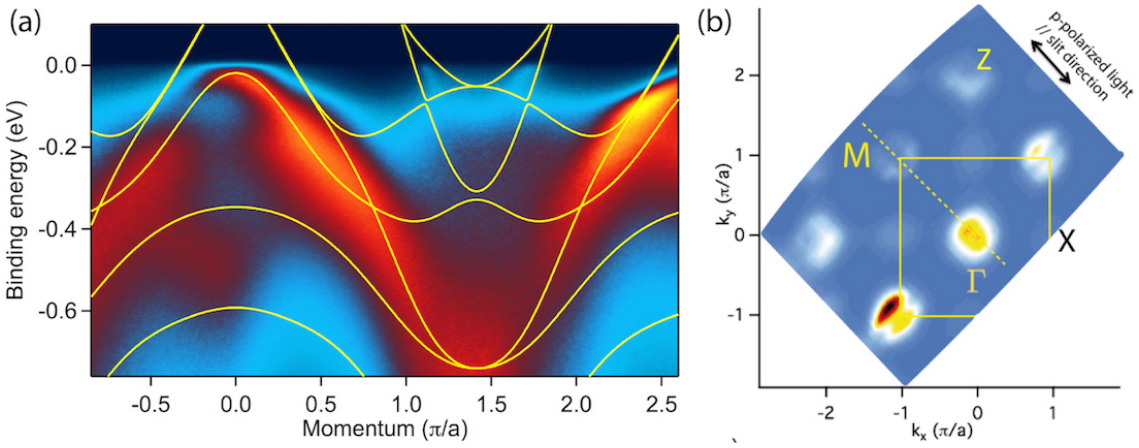

FIGURE 4.4: (a): ARPES intensity distribution map, $I(k, E)$, measured on as-grown $BaFe_{1.83}Co_{0.17}As_2$ with 74 eV photon energy. Also shown are tight-binding bands (yellow) of a 10 orbital model [93] with parameters optimized to match the measured dispersions. The data was taken from Ref. [96].

3 and further below, one of the key models to study correlation effects with optical spectroscopy (the extended Drude model) cannot easily be applied to the study of iron-pnictide superconductors. We therefore developed a framework to address the impact of correlations on the optical response and this will be described in this section. The extended Drude model is given by (see Ch.3):

$$\sigma(\omega, T) = \sigma_1(\omega, T) + i\sigma_2(\omega, T) = \frac{i\omega_p^2}{4\pi} \frac{1}{\omega + M(\omega, T)}, \tag{4.1}$$

where $\omega_p^2 = 4\pi ne^2/m$ is the plasma frequency and $M(\omega, T) = M_1(\omega, T) + iM_2(\omega, T)$ is the complex memory function.

The frequency and temperature dependent optical conductivity for interacting electrons can be obtained from the Kubo formalism as first derived by Allen [100]. This so-called Allen-Kubo formula for the optical conductivity is given by,

$$\sigma(\omega, T) = \frac{\omega_p^2}{i4\pi\omega} \int_{-\infty}^{+\infty} \frac{n_F(\omega + x, T) - n_F(x, T)}{\omega - \Sigma(x + \omega, T) + \Sigma^*(x, T) + i\Gamma_{imp}} dx \tag{4.2}$$

where n_F are the Fermi-Dirac distribution functions and $\Sigma(\omega, T) = \Sigma_1(\omega, T) + i\Sigma_2(\omega, T)$ is the so-called single-particle electron self energy. These self-energy functions describe the modification of the quasi-free electron dispersion and scattering rate as a result of residual interactions. Comparing Eq. 4.1 and Eq. 4.2, we see that there is a (integral) relation between the single-particle self-energy and the memory function. The single particle self-energy thus manifests itself in the free charge carrier response, appearing as a deviation from a classical Drude response. This makes optical spectroscopy a

powerful tool to probe self-energy effects [3] as a function of frequency and temperature simultaneously.

If we consider a Fermi liquid (FL) where the residual interactions are 'local', $\Sigma(\omega, T)$ follows a universal quadratic dependence on both energy and temperature. In this context 'local' is taken to mean that the residual interaction is considered to be momentum independent. For such a local Fermi liquid $\Sigma_2(\omega, T)$ takes on the form [101]:

$$\Sigma_2(\omega, T) = -\frac{i}{\pi k_B T_0}\left[(1+a)(\hbar\omega)^2 + (\pi k_B T)^2\right] \tag{4.3}$$

where an additional elastic resonant scattering contribution has been added, parameterized by the value of a. This additional parameter is a phenomenological parameter, which was introduced by Maslov and Chubukov [101] as explained below. $k_B T_0$ is an overall energy scale characterizing the correlation strength.

The real part of the self-energy can be obtained from Eq. 4.3 by Kramers-Kronig transformation. In real materials, we need to take into account that we have a finite bandwidth. In this case we can modify Eq. 4.3 to [101, 102],

$$\Sigma_2(\omega, T) = \begin{cases} \frac{1}{\pi k_B T_0}[(1+a)(\hbar\omega)^2 + (\pi k_B T)^2] & 0 < |\omega| < \omega_c \\ \frac{1}{\pi k_B T_0}[(1+a)(\hbar\omega_c)^2 + (\pi k_B T)^2] & \omega_c < |\omega| < D \\ 0 & D < |\omega| \end{cases}, \tag{4.4}$$

where D represents (a fraction of) the total bandwidth. We have also introduced a cutoff frequency ω_c above which the Fermi liquid response turns into a frequency independent scattering. To facilitate the calculation of the optical response for such a self-energy, we derived an analytical expression for the real part of the self-energy by Kramers-Kronig transformation. The real part, $\Sigma_1(\omega, T)$, is given by

$$\begin{aligned} \Sigma_1(\omega, T) = \; & \tfrac{(1+a)}{\pi^2 k_B T_0} 2\omega\omega_c + \tfrac{(1+a)}{\pi^2 k_B T_0}(\omega_c^2 - \omega^2)\left[\log\left(\tfrac{|D-\omega|}{|\omega_c-\omega|}\right) + \log\left(\tfrac{|\omega_c+\omega|}{|D+\omega|}\right)\right] \\ & + \tfrac{\Sigma_2(\omega,T)}{\pi}\log\left(\tfrac{|D-\omega|}{|D+\omega|}\right) \end{aligned} \tag{4.5}$$

for $0 < |\omega| < \omega_c$,

$$\Sigma_1(\omega, T) = \frac{(1+a)}{\pi^2 k_B T_0} 2\omega\omega_c + \frac{(1+a)}{\pi^2 k_B T_0}(\omega^2 - \omega_c^2)\log\left(\frac{|\omega_c - \omega|}{|\omega_c + \omega|}\right) + \frac{\Sigma_2(\omega_c, T)}{\pi}\log\left(\frac{|D-\omega|}{|D+\omega|}\right) \tag{4.6}$$

for $\omega_c < |\omega| < D$, and

$$\Sigma_1(\omega,T) = \frac{(1+a)}{\pi^2 k_B T_0} 2\omega\omega_c + \frac{\Sigma_2(\omega,T)}{\pi}\log\left(\frac{|\omega_c-\omega|}{|\omega_c+\omega|}\right) + \frac{\Sigma_2(\omega_c,T)}{\pi}\left[\log\left(\frac{|D-\omega|}{|\omega_c-\omega|}\right)+\log\left(\frac{|\omega_c+\omega|}{|D+\omega|}\right)\right] \tag{4.7}$$

for $\omega > D$.

In ref.'s [101, 102] an approximate expression for the memory function was derived, based on the energy and temperature dependent $\Sigma_2(\omega,T)$ (Eq. 4.3). These authors found that for a Fermi liquid, at low enough temperature, the memory function should have the following form:

$$M_2(\omega,T) = \frac{2}{3\pi k_B T_0}\left[(1+a)(\hbar\omega)^2 + (2\pi k_B T)^2\right] \tag{4.8}$$

Summarizing, the Kubo-Allen formula Eq. 4.2 combined with Eq. 4.3 predicts that the optical response for a Fermi liquid deviates from the basic Drude response and that this deviation is given by Eq. 4.8. Based on the work by Maslov and Chubukov [101] and later the work of Berthod *et al.* [102], several groups experimentally tested these predictions [103–107] in purported Fermi liquid materials. In these works a slightly modified Eq. 4.8 was used, namely:

$$M_2(\omega,T) = \frac{2}{3\pi k_B T_0}\left[(\hbar\omega)^2 + (p\pi k_B T)^2\right], \tag{4.9}$$

where $a = (p^2-4)/(1-p^2)$[101]. For a local FL ($a = 0$) one expects $p = 2$, however in most experiments deviations from this value are observed. To date the only known example with $p = 2$ is Sr_2RuO_4 [108], while $p \neq 2$ has been reported for several other materials [103–107].

When applied to the iron-pnictide superconductors, the accurate determination of $M(\omega,T)$ is hampered by the presence of low-lying interband transitions. In the following we first show that $M(\omega,T)$ extracted for carefully annealed $BaFe_{2-x}Co_xAs_2$ single crystals indeed displays the characteristic ω,T-scaling predicted by Eq. 4.9. We then introduce an analysis of the complex optical conductivity that represents a direct confirmation of the Fermi liquid normal state of these electron doped iron-pnictides . This is made possible by the 2 K temperature resolution in our experiments, which allows us to compare the detailed frequency *and* temperature dependence with similar resolution.

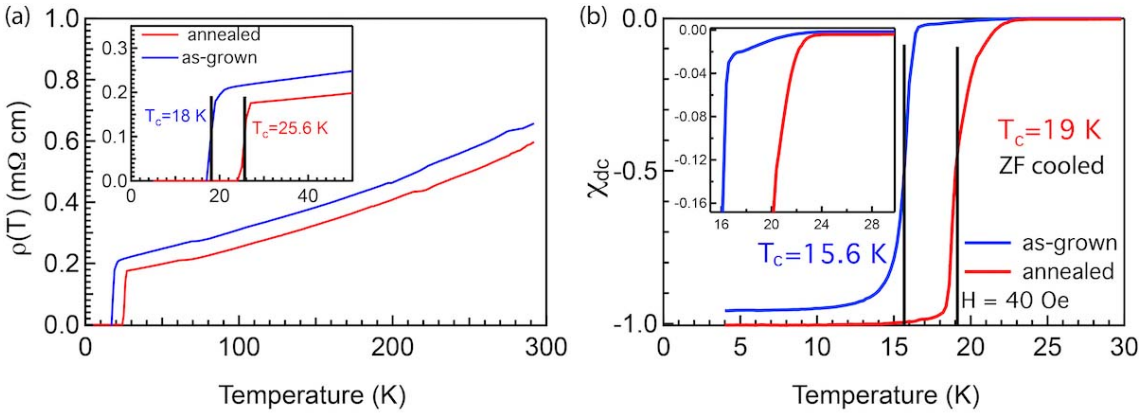

FIGURE 4.5: Two crystals were measured: as-grown (blue) and annealed (red) crystals. (a) dc resistivity with an approximate T^2 dependence up to 300 K. The little kinks at 70 K and 220 K are experimental artifacts. The inset shows an enlarged view of the superconducting transitions to the zero-resistance state. (b) dc susceptibility measured in a 40 Oersted field. As the inset shows the onset of the transition takes place at significantly higher temperature compared to the temperature where the full volume of the crystal becomes superconducting.

4.3 Optical properties of electron doped iron-pnictide superconductors.

4.3.1 Crystal growth and characterization.

A large 4 x 5 x 0.1 mm^3 single crystal of $BaFe_{1.8}Co_{0.2}As_2$ was grown from self-flux. Its chemical composition has been determined with electron probe microanalysis, resulting in the determination of a Co concentration, $x = 0.195$. We subsequently cut the crystal into two pieces and annealed one piece for 75 hours at 800 °C. The dc resistivity and susceptibility were measured for both pieces, see Fig. 4.5. The resistivity shows a significant enhancement of the critical temperature from 18 K for the as-grown crystal to 25.6 K in the annealed crystal. The dc susceptibility shows an onset to superconductivity at similar temperatures, but the full Meisner volume is obtained at somewhat lower temperatures. A similar increase in T_c has been previously reported in [109].

4.3.2 From reflectivity to optical conductivity.

The details of the experiments have been extensively described in Chapter 2. The reflectivity for the pnictide crystals studied in this chapter is shown in figure 4.6, at selected temperatures. For the as-grown crystal we observe the opening of the superconducting gap below 18 K as can be seen in panel 4.6c. The superconducting gap manifests itself as a small upturn at low frequency. Below the gap edge, the reflectivity has to be unity,

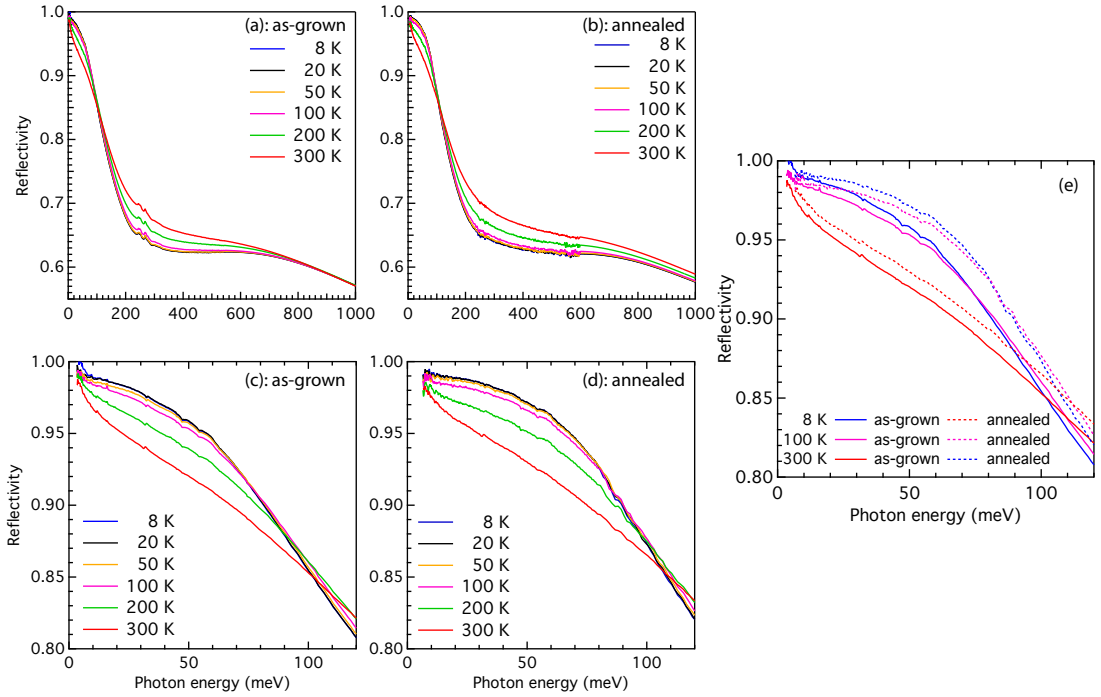

FIGURE 4.6: Reflectivity of the as-grown (a,c) and annealed (b,d) crystals at selected temperatures. (e): comparison between the two crystals at selected temperatures.

as there are no excitations possible inside the superconducting gap. The somewhat smaller crystal size (2 x 1 x 0.1 mm^3) for the annealed crystal complicated the accurate determination of the reflectivity below 10 meV. This is most likely due to diffraction effects becoming important at these longer wavelengths. Figure 4.6e compares the low frequency reflectivity of the annealed and as-grown crystals. Based on the higher reflectivity of the annealed crystal one can immediately observe that the overall scattering rate has decreased, assuming that the charge carrier concentration has not significantly changed. In a first step the reflectivity data is modelled using a Drude-Lorentz model with parameters optimized by a least-square Levenberg-Marquardt routine [23]. We tried different models to determine the robustness of the modeling, as we want to use it later on in the extended Drude analysis. The Drude-Lorentz models presented in table 4.1 (see below) for both crystals (i) gives the lowest χ^2, (ii) consistently describe our optical data at all temperatures and (iii) are nearly identical for both crystals as one might expect. Based on this model and the full reflectivity data we use a variational dielectric function routine developed in [22] to extract the optical conductivity, as will be discussed in the next section.

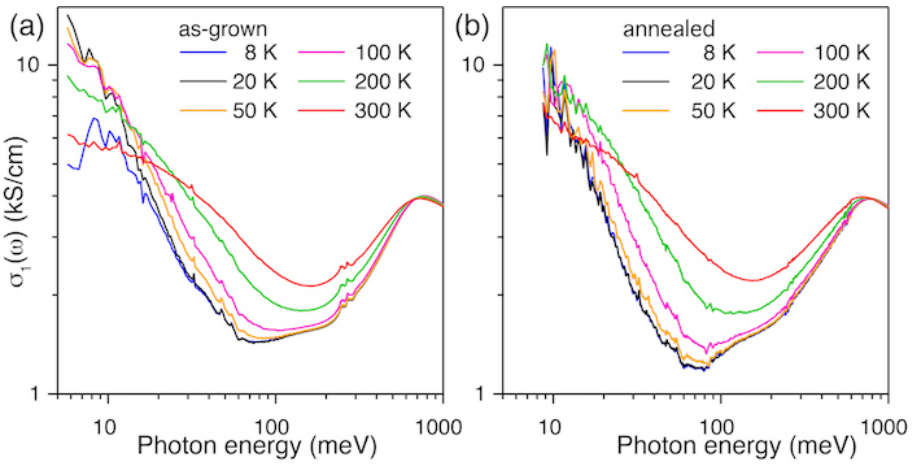

FIGURE 4.7: (a, b): Comparison of the real part of the optical conductivity $\sigma_1(\omega)$ for as-grown ($T_c \approx 18$ K) and annealed ($T_c \approx 25$ K) $BaFe_{1.8}Co_{0.2}As_2$ at selected temperatures. The most significant, annealing induced change is a reduction of a broad incoherent background that is most clearly seen by the deeper minimum around 70 meV separating the free charge and interband optical conductivity.

4.3.3 Optical conductivity.

The in-plane optical conductivity of as-grown and annealed $BaFe_{1.8}Co_{0.2}As_2$ are shown in Fig. 4.7a and 4.7b, respectively. After annealing we observe a decrease in the depth of the minimum around 70 meV separating the free-charge and interband optical conductivity. To pin-point its origin we turn to a standard Drude-Lorentz modeling of the data. The decomposition of the optical conductivity of both as-grown and annealed crystals in Drude and Lorentz terms is given in table 4.1. We find that the intraband contribution can be described by two relatively narrow Drude terms and a low energy Lorentz oscillator. The incoherent background extending to low energy is captured by a high energy oscillator (labeled as number 7 in table 4.1). Upon annealing, the width of this oscillator decreases, resulting in a much weaker contribution at low energy. This effect can be clearly seen in the optical conductivity data by comparing the depth of the minimum (at 70 meV) separating the intra- and interband response. Apart from this difference in the incoherent background, the Drude-Lorentz models are nearly identical, indicating that the annealing results in a rather subtle change of the intraband response. Put differently, annealing does not significantly change the overall

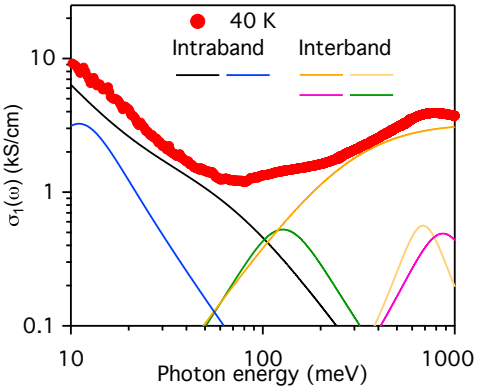

FIGURE 4.8: Experimental spectrum for the annealed crystal at 40 K (symbols) and the decomposition in oscillators (solid lines) corresponding to the parameters given in table 4.1. Note that the two Drude components are plotted as a single curve (black).

TABLE 4.1: The high-frequency dielectric constant $\epsilon_\infty \approx 9$. ω_j is the centre frequency of an oscillator, ω_{pj} its area (Drude terms) or oscillator strength and γ_j is the width. All values reported correspond to 40 K data.

as-grown								
j	1	2	3	4	5	6	7	8
$\hbar\omega_j$ (eV)	0	0	0.01	0.12	0.67	0.92	1.6	1.82
$\hbar\omega_{pj}$ (eV)	1	0.96	0.42	0.59	2.49	1.96	14.56	3.65
$\hbar\gamma_j$ (eV)	0.005	0.065	0.01	0.12	0.58	0.73	14.55	1.84
annealed								
$\hbar\omega_j$ (eV)	0	0	0.011	0.13	0.68	0.87	1.6	
$\hbar\omega_{pj}$ (eV)	1.1	0.8	0.51	0.72	1.28	1.62	14.95	
$\hbar\gamma_j$ (eV)	0.0034	0.064	0.01	0.13	0.39	0.72	9.48	

electronic structure (such as a large chemical potential shift), and the high-energy optical properties are mostly unaffected. The optical conductivity of the annealed crystal at 40 K and its decomposition in terms of the oscillators from Table 4.1 is shown in Fig. 4.8 for completeness.

4.3.4 Spectral weight analysis

Once the optical conductivity is known, we can calculate derived quantities such as the optical spectral weight. The spectral weight can be used to further quantify the annealing induced changes in the optical response and is a necessary ingredient for the determination of the memory function. An interesting quantity is the plasma frequency, which is the integrated *intra*-band optical conductivity. Unfortunately, as the previous section shows, interband transitions are present in the entire energy range and it is not clear how to separate the two. As discussed in Chapter 3, the spectral weight is obtained by integrating the real part of the optical conductivity over frequency up to a cutoff frequency ω_c:

$$SW(\omega_c, T) = \int_0^{\omega_c} \sigma_1(\omega, T) d\omega \tag{4.10}$$

Figure 4.9 shows the integrated spectral weight as function of cutoff frequency ω_c. For both crystals we find that the integrated spectral weight is nearly temperature independent for $\omega_c \approx 100$ meV, corresponding roughly to the minimum in the optical conductivity presented in Fig. 4.7a,b. At this point the integrated spectral weight $SW(\omega_c, T) \approx 3.1\pm0.15 \cdot 10^6\ \Omega^{-1}\text{cm}^{-2}$ (as-grown) and $SW(\omega_c, T) \approx 3.4\pm0.15 \cdot 10^6\ \Omega^{-1}\text{cm}^{-2}$ (annealed). If we assign this spectral weight in both cases entirely to the intraband response we obtain values for the plasma frequencies of: $\omega_p \approx 1.35$ eV (as-grown) and $\omega_p \approx 1.4$ eV (annealed). Given the error bar on the estimation of $SW(\omega_c, T)$ we use $\omega_p \approx 1.4$ eV for both crystals.

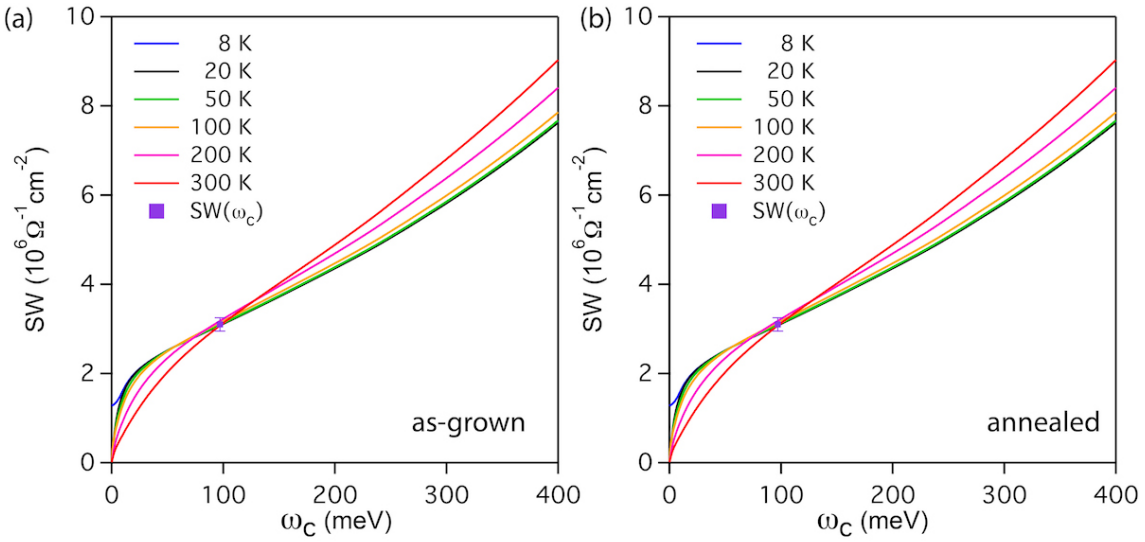

FIGURE 4.9: Spectral weight of the as-grown (a) and annealed (b) crystals at selected temperatures.

4.4 Experimental signatures of the Fermi liquid state.

Subtle changes in the free charge carrier response are more easily analyzed in terms of equations (4.1) and (4.9), but the extended Drude model analysis assumes that interband transitions do not contribute to the optical conductivity in the energy range of interest. The multi-band nature of the pnictides complicates the extraction of $M(\omega, T)$ since inter-band processes have a significant contribution to the optical conductivity [6, 7, 110, 111]. In the next section I will first describe the procedure used to extract the memory functions and explain how we determined the range of validity.

4.4.1 Extended Drude analysis: interband contributions and range of validity.

As discussed above, overlapping intra- and interband conductivities complicate the extraction of the memory function from optical conductivity data. In the absence of overlapping intra- and interband conductivities (e.g. such as is the case for cuprate HTSC) one can write the memory function in terms of the dielectric function:

$$M_1(\omega) = \frac{\omega_p^2}{\omega} \frac{\varepsilon_2(\omega)}{[\varepsilon_{\infty,IR} - \varepsilon_1(\omega)]^2 + \varepsilon_2^2(\omega)} \tag{4.11}$$

$$M_2(\omega) = \frac{\omega_p^2}{\omega} \frac{\varepsilon_{\infty,IR} - \varepsilon_1(\omega)}{[\varepsilon_{\infty,IR} - \varepsilon_1(\omega)]^2 + \varepsilon_2^2(\omega)} - \omega \tag{4.12}$$

where $\varepsilon_{\infty,IR}$ represents a frequency independent contribution to the *real part* of the dielectric function due to high energy interband transitions, which can be estimated from the oscillator strengths of those transitions. What happens in the case of iron-pnictides where interband transitions have a low energy onset (estimated to be situated around 100 meV, see Fig. 4.8)?

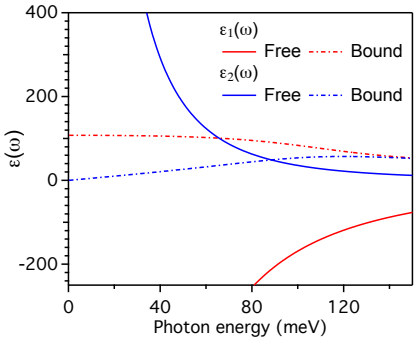

FIGURE 4.10: Decomposition of the dielectric function in bound and free charge response at 40 K corresponding to the model parameters of table 4.1.

This is most clearly illustrated in figure 4.10 where we show the free charge (or intraband) and bound charge (or interband) contributions to the dielectric model presented in table 4.1. The question that arises is whether the bound charge response can be approximated with a constant in the photon energy range where we want to analyze the memory function. Given the relative strengths of the free and bound charge response, the approximation of using a frequency independent $\varepsilon_{\infty,IR}$ could possibly be upheld below about 50 meV. This is fortified by explicitly calculating the imaginary part of the memory function for a series of models as we will now discuss.

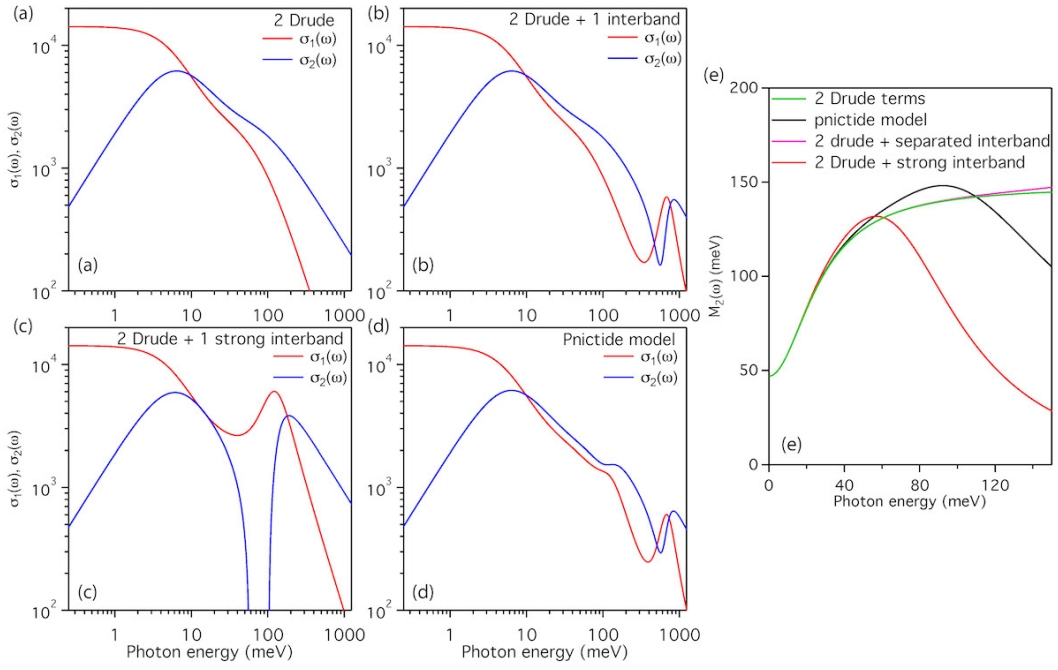

FIGURE 4.11: (a): superposition of two Drude terms, (b): two Drude terms and a well separated interband transition, (c): two Drude terms and a strong interband transition overlapping with the intraband response and (d): a model used for the annealed crystal. (e): Memory functions calculated for each of the panels (a-d) without taking the presence of the interband transitions into account. The comparison shows that the additional frequency dependence of interband processes is modest for photon energies up to 50 meV for the worst case considered (e.g. two Drude terms + overlapping strong interband transition).

Fig. 4.11 shows the optical conductivity for 4 different models. In panel 4.11a the real and imaginary part of a sum of two Drude terms with different widths is shown. Panel 4.11b,c show the same model but now with a single interband transition added to it. In panel 4.11b the intra- and interband parts are well separated as in the cuprates, while panel 4.11c has a strong interband transition well within the intraband region. Finally, panel 4.11d shows the optical conductivity for a model similar to the pnictide model. Panel 4.11e now compares the extracted memory functions for these models *without* making any correction for the interband contribution. The two Drude case (in green) would represent the correct optical scattering rate that we would like to extract in an experiment. The other cases show deviations from this ideal curve to varying degrees. What is important for the current work is that below about 50 - 80 meV the frequency dependence in all cases is very close to the ideal case indicating that in the realistic case relevant to the iron-pnictides (black curve) the extended Drude model gives relevant results in the low energy range.

4.4.2 Extended Drude model: comparison of methods

Despite the reassuring results of the previous section, we tested two methods to determine the memory function. In the first method we approximate the interband contribution to the optical conductivity with a temperature independent $\varepsilon_{\infty,IR} \approx 100$ - 105 (for as-grown and annealed crystals respectively). We then use Eq. 4.11 to calculate the memory function. In the second method we subtract the interband part obtained from the Drude - Lorentz model obtained at each individual temperature. In this section we compare both methods and will find that the final results provide similar results. First of all, at low temperatures ($\leq$ 150 K) and photon energies between 10 - 50 meV both methods give nearly identical results. At higher temperatures differences are starting to become more evident as can be seen most clearly by comparing the 200 K data for the annealed crystal. At photon energies above 50 meV differences

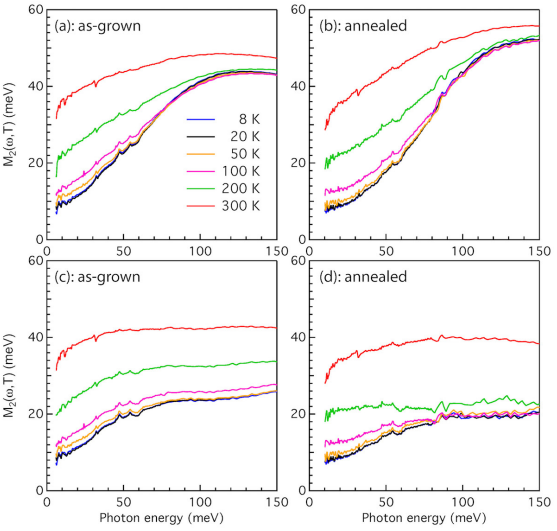

FIGURE 4.12: Comparison between the memory functions obtained using the method of subtracting $\varepsilon_{\infty,IR} \approx 100$ -110 (a,b) and by subtracting the full frequency dependent interband conductivity (c,d).

between the two methods become more prominent. In particular, a significant extension of the photon energy range where $M_2(\omega, T)$ shows a strong frequency dependence becomes apparent from the comparison of the top and bottom panels.

4.4.3 (ω, T)-scaling of the optical response.

The previous section shows that even though the determination of the memory function comes with uncertainty at higher energies, at low energies ($\hbar\omega \leq 50$ meV) interband transitions only weakly affect the frequency dependence. In the following we use the second method to subtract the interband response, as this provides the most stringent test; however, we note that our conclusions remain the same when alternative methods for accounting for the interband transitions are applied.

The frequency and temperature dependence of the imaginary part of the memory function $M_2(\omega, T)$, is shown in Fig. 4.13a and 4.13b for the as-grown and annealed crystal. The clear frequency dependence of the memory function indicates the presence of residual interactions beyond a classical Drude response. We fit both datasets with a power-law form $M_2(\omega, T) = 1/\tau(0, T) + B(T)\omega^{\eta(T)}$, where $1/\tau(0, T)$ is the zero-frequency scattering rate and $\eta(T) = 2$ is expected for a FL. These parameters are determined independently at each temperature. The temperature dependence of $1/\tau(0, T)$ and $\eta(T)$ are displayed in Fig. 4.13c,d for both the as-grown and annealed crystal. We find that the annealed crystal displays characteristic FL behavior with $\frac{1}{\tau(T)} \sim T^2$ (Fig. 4.13c) and $\eta(T) \sim 2$ (Fig. 4.13d) over a large range of energy (10 meV $\leq \hbar\omega \leq$ 50 meV) and temperature (8 K $\leq T \leq$ 100 K). We further find that the prefactor $B(T)$ is temperature independent in the same temperature range as is expected from Eq. (4.9) (see next section). The as-grown crystal on the other hand does not display FL behavior. Instead, the zero frequency scattering rate follows a more linear temperature dependence, while the frequency exponent $\eta(T) < 2$. Given the approximate T^2 and ω^2 dependence of the memory function apparent in Fig. 4.13c,d we test whether the scaling form of Eq. 4.9 applies to the annealed crystal. Fig. 4.13e demonstrates that $M_2(\omega, T)$ indeed follows a universal FL scaling as function of the scaling variable $\xi^2 = (\hbar\omega)^2 + (p\pi k_B T)^2$, with $p \approx 1.47$ (see also the next section).

We highlight three deviations from universal FL behavior that can be discerned in Fig. 4.13e. First, universal FL behavior disappears above 100 K. Second, for $\xi^2 \geq 2500$ meV^2, $M_2(\xi)$ changes slope, as indicated by the dashed pink line, signaling a crossover to a nearly energy independent $M_2(\omega, T)$ for $\hbar\omega \geq 50$ meV (Fig. 4.13b). Third, $p = 1.47$ rather than 2, indicating that an additional elastic contribution is present beyond residual electron-electron scattering. However, the precise value of p determined by

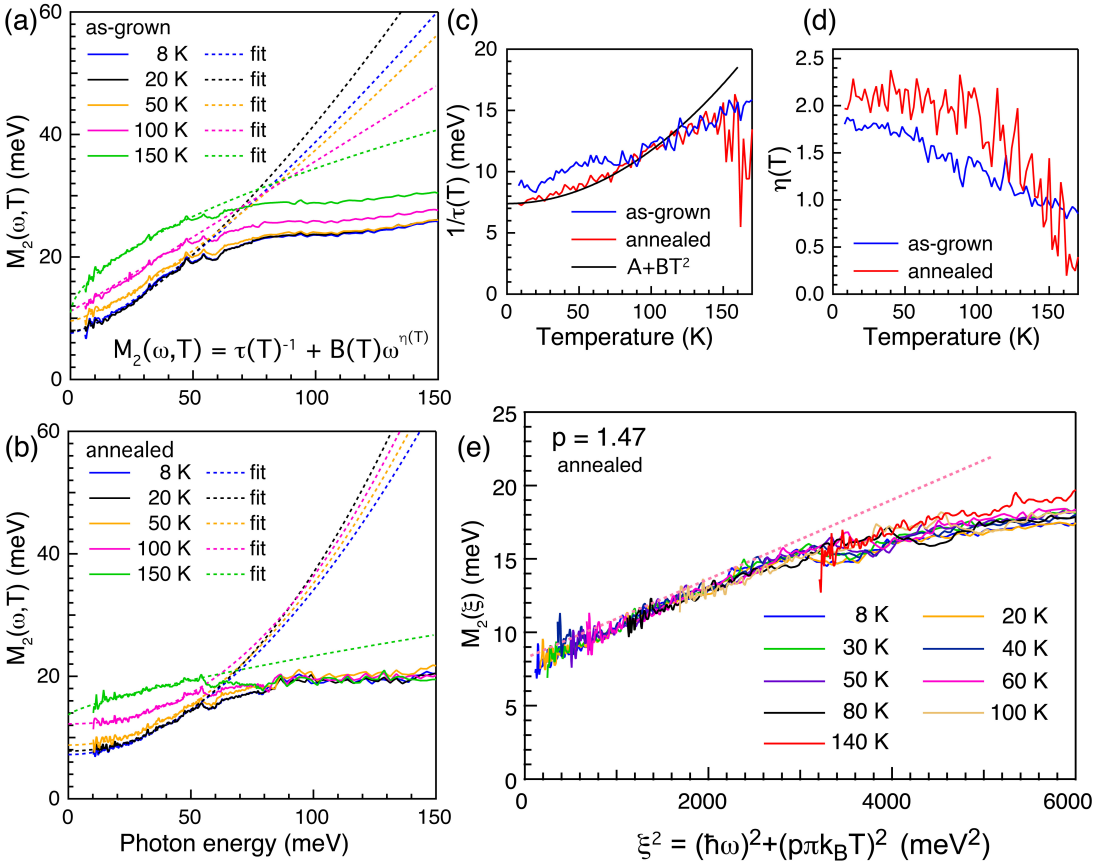

FIGURE 4.13: (a, b): Imaginary part of the memory function, $M_2(\omega, T)$, revealing the difference in free charge response for as-grown and annealed crystals. The memory function is obtained by subtracting the full interband response as discussed in sec. 4.4.2. Dashed curves indicate fits made using the fitting function indicated in panel (a). (c): Temperature dependence of the static scattering rate $1/\tau(T)$ obtained from the fits in panels (a, b). For the annealed crystal $1/\tau(T)$ displays a T^2 behavior below $T \sim 100$ K as indicated by the fit. (d): Temperature dependence of the exponent, $\eta(T)$, extracted from the fits in panel (a, b). The exponent for the annealed crystal shows ω^2 dependence in the same temperature range where $1/\tau(T)$ has a T^2 temperature dependence. At higher temperatures a clear deviation from Fermi liquid behavior is found. (e): Scaling collapse obtained by plotting $M_2(\omega, T)$ as $M_2(\xi)$, where $\xi^2 = (\hbar\omega)^2 + (1.47\pi k_B T)^2$. Above $\xi^2 \approx 2500$ meV^2 the scaling deviates from the universal Fermi liquid behavior which is indicated by the dashed pink line.

collapsing the data on a universal curve comes with some uncertainty as it depends on the assumed strength and frequency dependence of the interband contribution as we will now show.

4.4.4 Determination of the scaling parameter p.

In section 4.4.2, we already alluded to the fact that one of the key results, namely the T^2 and ω^2 dependence of $M_2(\omega, T)$, would be extended over a larger energy and temperature range if a different method to determine $M_2(\omega, T)$ is used. Here we will discuss the estimation of the value of p for which all the data collapses onto a universal curve. In Ref. [108] the following method was proposed: one plots the data as function of $\xi^2 = \left[(\hbar\omega)^2 + (p\pi k_B T)^2\right]$ for a range of values of p. We take $1 \leq p \leq 2$ with steps of 0.01. One then calculates the root-mean square for each value of p determined by summing over the deviations of each temperature from a universal curve for that value of p. These RMS values are then summed over a range of temperatures up to a certain maximal temperature. Figure 4.14 shows the dependence of p on the maximum temperature, T_{max}, used in the scaling analysis. We apply this method to the memory function extracted with both methods indicated above and find that the value of p depends weakly on temperature. At 100 K, where the power of the frequency dependence starts to deviate from $\eta \approx 2$ we find the values $p = 1.2$ (ε_∞ correction) and $p = 1.47$ (interband subtraction).

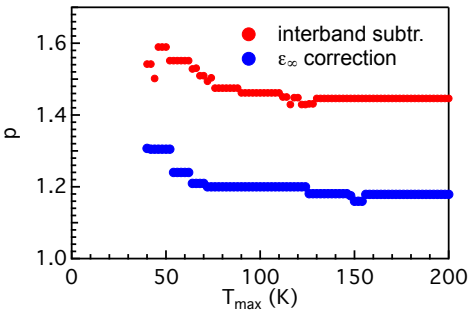

FIGURE 4.14: Value of p giving the best scaling collapse as a function of maximum temperature used in the determination of the deviation of the data from a universal curve.

4.4.5 Robustness of the scaling collapse and consistency with transport data.

In section 4.4.3 we showed that the DC extrapolation of the scattering rate follows a T^2 temperature dependence, implying that the resistivity is also a function of T^2. To confirm this expectation we show in figure 4.15a the resistivity data of Fig. 4.5 plotted as function of T^2. We indeed find that $\rho(T)$ is an approximate function of T^2 in the same range of temperatures (30$\leq$ T $\leq$120 K) as $1/\tau(0)$ (see Fig. 4.15b). From Fig. 4.15a we estimate $d\rho/d(T^2) \approx 6.5{\cdot}10^{-9}$ Ω cm/K^2, while $d(\tau)^{-1}/d(T^2) \approx 3.5{\cdot}10^{-3}$ cm^{-1}/K^2. We can now use the Drude expression for the DC resistivity $\rho = 4\pi/\omega_p^2\tau$ to compare the slopes of both quantities. Together with the plasma frequency $\omega_p \approx 11290$ cm^{-1} we obtain $d\rho/d(T^2) \approx 1.7{\cdot}10^{-9}$ Ω cm/K^2 from $d(\tau)^{-1}/d(T^2)$. Given the uncertainties involved in determining $1/\tau(0)$ this is a reasonable agreement. We note that the resistivity deviates from the approximate T^2 behavior at the onset of superconductivity and at elevated temperatures. Above the temperature scale where Fermi liquid scaling

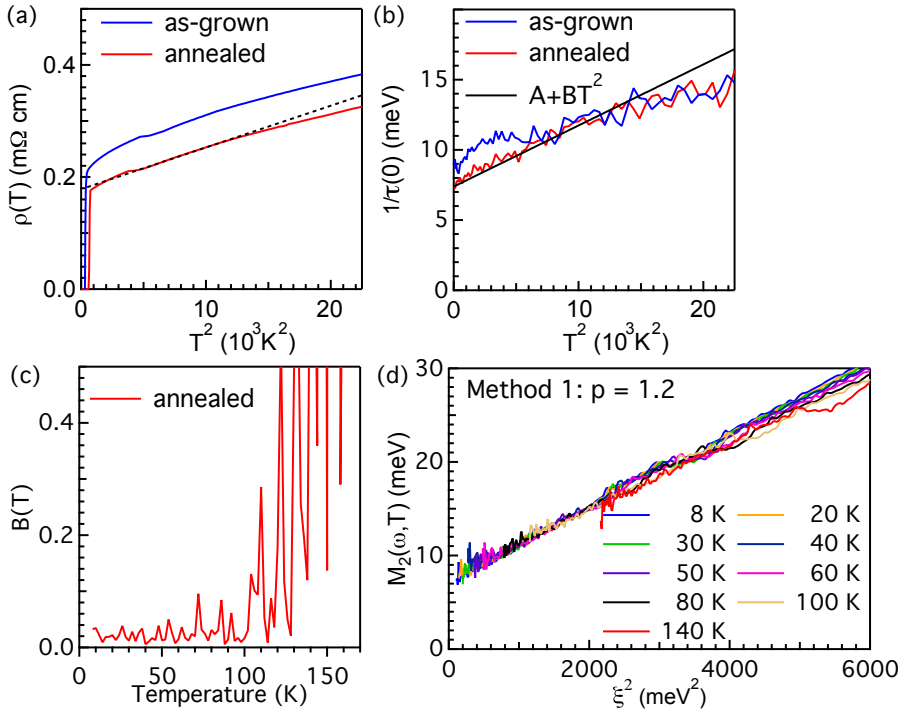

FIGURE 4.15: (a): Resistivity as function of T^2. The dashed line is a guide to the eye. (b): DC scattering rate as function of T^2. This panel is equivalent to Fig. 4.13e of the main text (c): Prefactor, $B(T)$, of the frequency component of the memory function. (d): Scaling collapse of $M_2(\omega, T)$ obtained by correcting M_2 with a frequency independent interband contribution.

applies both the DC resistivity and scattering rate are still approximate functions of T^2, but with slightly smaller slopes as can be seen from the deviation from the black lines. Figure 4.15(c) shows the temperature dependence of the pre-factor, $B(T)$, of the frequency component appearing in $M_2(\omega, T) = 1/\tau(0, T) + B(T)\omega^{\eta(T)}$. Comparing this empirical relation with Eq. 4.9, $B(T)$ is expected to be temperature independent in the range of validity of Eq. 4.9. Fig. 4.15(c) shows that this is indeed the case below $T \approx 100$ K. In panel 4.15(d) we plot the scaling collapse for the memory function obtained by subtracting $\varepsilon_{\infty,IR}$. Note that in this case the scaling extends over a larger energy window due to the higher energy where the memory function saturates (≈ 120 meV, Fig. 4.12b).

4.5 Direct observation of Fermi liquid signatures in the optical conductivity.

Our analysis provides compelling evidence that the normal state of $BaFe_{1.8}Co_{0.2}As_2$ below 100 K is properly classified as a FL. As the previous section shows, the specific method of accounting for interband processes does not alter the conclusion that the low frequency and temperature dependence of $M_2(\omega, T)$ follows ω^2 and T^2 scaling. In

contrast, the same analysis applied to the as-grown crystal does not show such clear signatures of FL behavior, despite its similar plasma frequency and high-energy optical properties. Nevertheless, the determination of the parameters characterizing the Fermi liquid state using the extended Drude analysis remains sensitive to the choice for the interband contribution. To strengthen our conclusions, and to determine the characteristic properties of the Fermi liquid state more accurately, we now turn our attention to an analysis of the complex optical conductivity, which provides a more direct comparison between theory and experiment and does not require a model specific choice for the interband processes.

4.5.1 Zero crossings and the complex optical conductivity.

Berthod *et al.* showed [102] that in a local FL a dome is defined by the locus of points where $\sigma_1(\omega, T) = \sigma_2(\omega, T)$, which bounds a 'thermal' regime in which FL behavior emerges. Zero crossings signaling the presence of a dome have been clearly observed [108] in Sr_2RuO_4 at low temperatures. Despite the clean Fermi liquid behavior, exemplified in that case by $p = 2$, these authors found that at elevated temperatures deviations from the predicted dome shape appeared, which they linked to the increasing importance with increasing temperature of 'resilient' quasi-particles. This observation provides the means to make a direct comparison between the optical conductivity and theoretical calculations, where one does not have to resort to making the decompositions involved in the extended Drude analysis presented in Fig. 4.13.

Berthod *et al.* observed that in a Fermi liquid the optical conductivity could be described by three different frequency regimes [102]. These regimes are, at low temperature, separated by crossings of $\sigma_1(\omega)$ and $\sigma_2(\omega)$. They demonstrated that at low frequency the optical conductivity follows a Drude behavior, with $\sigma_1(\omega) \leq \sigma_2(\omega)$, at intermediate frequency a thermal regime appears with $\sigma_1(\omega) \geq \sigma_2(\omega)$ and finally at high frequency $\sigma_1(\omega) \leq \sigma_2(\omega)$ again. The boundary separating these regimes can be easily derived from the optical conductivity. Starting from Eq. 4.1 with $M(\omega)$ given by [102],

$$M(\omega) = \frac{i}{\pi k_B T_0} \left[\omega^2 + (2\pi k_B T)^2\right], \tag{4.13}$$

we can equate $\sigma_1(\omega) = \sigma_2(\omega)$, to obtain a second order equation relating temperature T and frequency ω. Solving for T gives [102]:

$$T_1(\omega) = \sqrt{\frac{3k_B T_0}{8\pi}\left(\omega - \frac{2\omega^2}{3\pi k_B T_0}\right)}. \tag{4.14}$$

As was shown in Ref. [101], the pre-factor of the temperature term can be different from 2 if additional contributions to the frequency dependence of the self-energy are present, in which case:

$$\Sigma(\omega) = \frac{i}{\pi k_B T_0}\left[(1+a)\omega^2 + (\pi k_B T)^2\right]. \tag{4.15}$$

Given the value of $p = 1.47$ determined from the scaling collapse presented in sec. 4.4.3, we should therefore take,

$$T_1(\omega) = \sqrt{\frac{3k_B T_0}{8\pi}\left(\omega - \frac{2(1+a)\omega^2}{3\pi k_B T_0}\right)}. \tag{4.16}$$

with $a = (p^2-4)/(1-p^2)$. However, low energy interband contributions further complicate matters. Below we will therefore use the full Allen-Kubo formula (Eq. 4.2 and calculate $\Delta\sigma(\omega, T)$, including the full frequency dependent interband conductivity. It is however instructive, and possibly useful for other materials, to approximate the interband contribution with a purely reactive component and derive an analytic expression for the zero crossings. We will show below that the zero crossings of this expression and the full calculation do not differ too much. Starting instead from,

$$\sigma(\omega) = \frac{i\omega_p^2}{4\pi}\frac{1}{M(\omega)+\omega} - \frac{i\omega\varepsilon_\infty}{4\pi} \tag{4.17}$$

which is equivalent to,

$$\sigma(\omega) = \frac{1}{4\pi}\left[\frac{\omega_p^2 M_2(\omega) + i\left[\omega_p^2\bar{\omega} - \omega\varepsilon_\infty\left(\bar{\omega}^2 + (M_2(\omega))^2\right)\right]}{\bar{\omega}^2 + (M_2(\omega))^2}\right] \tag{4.18}$$

with $\bar{\omega} = \omega + M_1(\omega)$. We consider again the case where $M_1(\omega)$=0 and $M_2(\omega) \propto \left[(1+a)\omega^2 + (2\pi k_B T)^2\right] + \Gamma_0$. Here the last term is an additional, frequency independent impurity scattering rate. Solving Eq. 4.18 for $\sigma_1(\omega) = \sigma_2(\omega)$ results in a fourth-order equation in T and ω, which has only one physical solution:

$$T_\infty(\omega) = \frac{1}{4}\sqrt{\frac{3}{\varepsilon_\infty\pi\omega}\sqrt{T_0^2\left[\omega_p^4 + 4\varepsilon_\infty\omega^2\omega_p^2 - 4\varepsilon_\infty^2\omega^4\right]} - \frac{4\omega^2(1+a)}{\pi^2} - \frac{3T_0\omega_p^2}{\varepsilon_\infty\pi\omega} - \frac{6\Gamma_0 T_0}{\pi}}. \tag{4.19}$$

Although this expression looks more unwieldy than Eq. 4.14, most of the parameters can be determined independently from each other. The plasma frequency, ω_p, can be determined from a spectral weight analysis, while ε_∞ can be estimated from a Drude-Lorentz analysis. Γ_0 can be determined at low temperature from an extrapolation of $M_2(\omega)$ to $\omega = 0$. This leaves T_0 and p as free parameters.

4.5.2 Characteristic Fermi liquid properties of Co-doped $BaFe_2As_2$.

The results of the previous section suggest a new method to facilitate a direct comparison between experiment and theory. We introduce the function $\Delta\sigma(\omega,T) \equiv \sigma_1(\omega,T) - \sigma_2(\omega,T)$, which is readily obtained from experimental data and also from calculations of the optical conductivity. For the particular case of a local FL, the function $\Delta\sigma(\omega,T)$ has the property that it is negative in the thermal regime where characteristic FL behavior should be observed, while it is positive in the incoherent and Drude-like regimes. Moreover, the zeros of this function correspond to the "dome" derived in the previous section. $\Delta\sigma(\omega,T)$ thus allows us to examine the full, complex optical conductivity and search for zero-crossings where $\sigma_1(\omega,T) = \sigma_2(\omega,T)$.

In Fig. 4.16a, $\Delta\sigma(\omega,T)$ is displayed as a false color plot for the annealed crystal. Blue represents $\Delta\sigma(\omega,T) < 0$, while red indicates $\Delta\sigma(\omega,T) > 0$. $\Delta\sigma(\omega,T) = 0$ is indicated in white. The most striking feature of Fig. 4.16a is a clear dome of zero crossings, closely resembling the dome predicted by Berthod *et al.*. In Fig. 4.16b we display calculations of $\Delta\sigma(\omega,T)$, assuming a FL self-energy. Motivated by the saturation of $M_2(\omega,T)$ above 50 meV (Fig. 4.13b), we have introduced a cutoff ω_c above which the imaginary part of the single particle self-energy, $\Sigma_2(\omega,T)$, is constant (see Fig. 4.17a and sec. 4.2.4) and a high energy cutoff D. The calculated $\Delta\sigma(\omega,T)$ is in excellent agreement with the experimental data. As input for the calculation we have used several experimentally available parameters, namely $\omega_p \approx 1.4$ eV, $\Gamma_0 = M_2(\xi \to 0) \approx 7$ meV and $p \approx 1.47$. The cutoffs $\omega_c \approx 41$ meV and $D \approx 1$ eV are motivated below. In addition to the free charge response, we also include the frequency dependent interband response from table 4.1. The only remaining free parameter, $T_0 \approx 1700$ K, is determined by two criteria: (i) the maximum of the dome of zero crossings (at $\hbar\omega \approx 55$ meV) and (ii) the low temperature zero-crossing at $\hbar\omega \approx 100$ meV. To facilitate the estimation of T_0, we use the analytical expression, $T_\infty(\omega)$ derived in the previous section (Eq. 4.19). The consistency between $T_\infty(\omega)$, the data, and the calculation (which includes the full frequency dependence of the interband response) shows that the details of the interband response are unimportant for obtaining this level of agreement.

The deviation from scaling in Fig. 4.13(c-e) around 100 K signals a crossover temperature where $\hbar\omega \leq p\pi k_B T$, above which an incoherent regime emerges [101, 102]. This suggests a natural cutoff $\hbar\omega_c \approx 1.47\pi k_B T$ with $T \approx 100$ K, resulting in $\omega_c \approx 41$ meV. The cutoff $D \approx 1$ eV is less critical but is motivated by the value of T_0. Dynamical Mean Field Theory (DMFT) calculations for a single band Hubbard model [102] indicate that $k_B T_0 \approx 0.57\delta W$ where W is half the bandwidth and δ is the carrier density. This yields

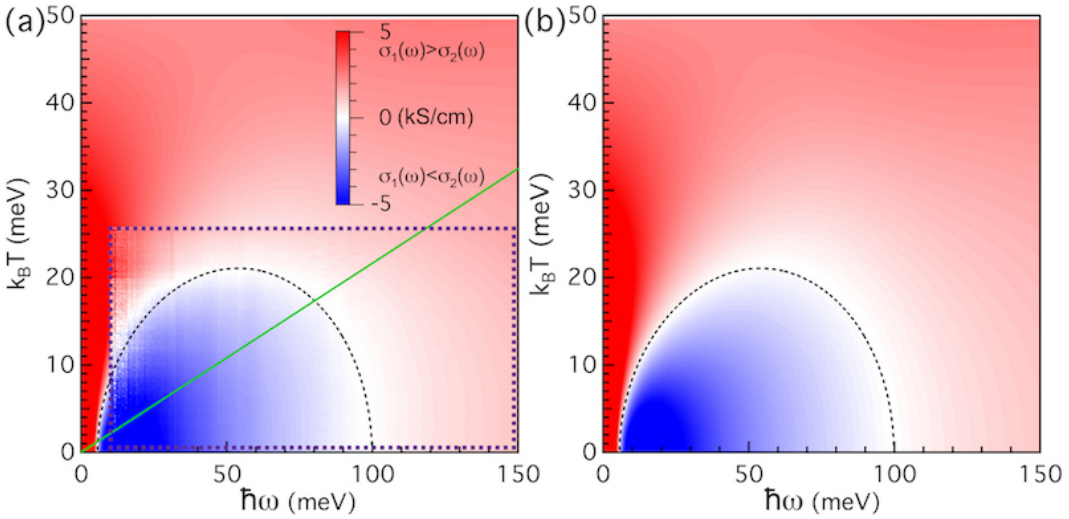

FIGURE 4.16: (a): (ω,T) dependence of $\Delta\sigma(\omega,T) \equiv \sigma_1(\omega,T) - \sigma_2(\omega,T)$. The experimental data is bounded by the purple dashed box, while the background image is the same as in panel **b**. Colour is used to indicate the magnitude of $\Delta\sigma(\omega,T)$, with red indicating the dissipative regime ($\sigma_1(\omega,T) > \sigma_2(\omega,T)$) and blue indicating the inductive regime ($\sigma_1(\omega,T) < \sigma_2(\omega,T)$). The colour scale is chosen such that the boundary between these two regimes, where $\sigma_1(\omega,T) \approx \sigma_2(\omega,T)$, or $\Delta\sigma(\omega,T) \approx 0$, appears as white. This dome of zeroes can be reproduced using the approximate expression $T_\infty(\omega)$. The green line indicates the crossover temperature $1.47\pi k_B T = \hbar\omega$, below which Fermi liquid behavior can be expected. (b): Same as in panel (a), but calculated from the Allen-Kubo formula for the optical conductivity using a Fermi liquid self-energy with parameters derived from the experimental data of Fig. 4.13. The dashed semi-circle is the same as in panel (a).

$W \approx 1.3$ eV in our case, which is reasonable compared to combined density functional theory and DMFT (e.g LDA+DMFT) estimates [80].

Apart from the saturation in $\Sigma_2(\omega,T)$, ω_c also introduces a frequency dependence in $\Sigma_1(\omega,T)$. This is clear from the derivation presented in sec. 4.2.4. The calculated self energy is presented in Fig. 4.17a. The frequency dependence of $\Sigma_1(\omega,T)$ should be manifest as a frequency dependent mass enhancement $m^*/m(\omega,T) \equiv 1 + M_1(\omega,T)/\omega$ in the free charge response. Fig. 4.17b shows excellent agreement between $m^*/m(\omega,T)$ extracted from experiment and the theoretical calculation where $m^*/m(\omega \to 0,T) \approx 1.2$. This value is consistent with a modest $m^*/m \approx 1.8$ predicted by LDA+DMFT calculations for this level of electron doping [80]. The experimental data leaves some room for additional mass enhancement resulting from boson exchange processes (such as phonons or spin-fluctuations) below $\hbar\omega \approx 10$ meV, although it is difficult to make a quantitative statement on their strength due to the low signal-to-noise at low energy. More importantly, the energy dependence of the mass-enhancement introduced through the cutoff in our self-energy rules out the presence of a significant boson exchange spectrum for $\hbar\omega \geq 10$ meV. We emphasize that the calculated mass enhancement is based on an analysis of the optical conductivity, while the experimental mass enhancement is determined using the extended Drude analysis presented in Fig. 4.13. The excellent

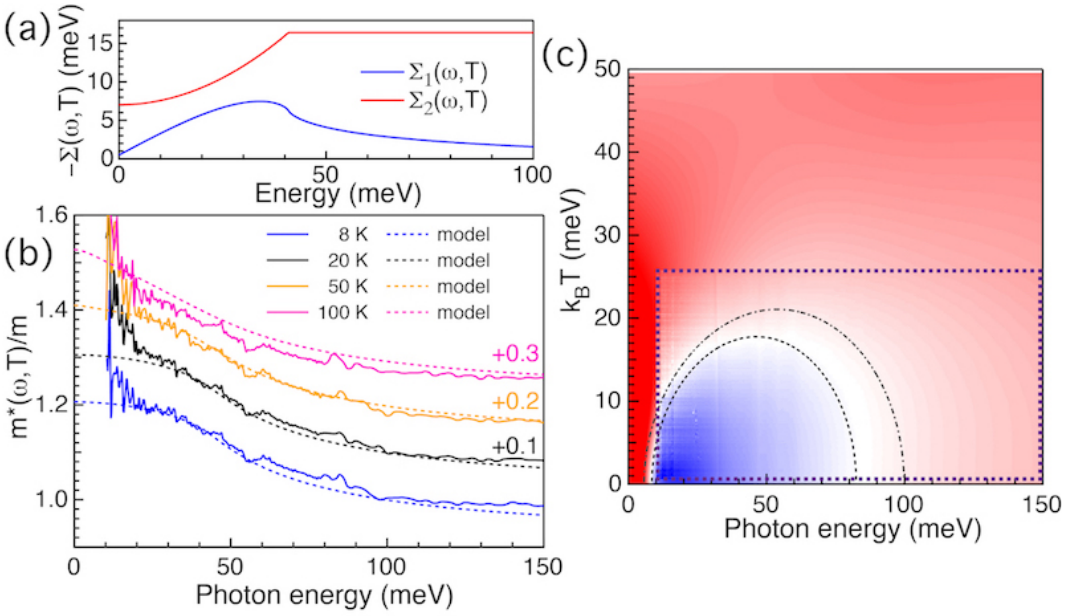

FIGURE 4.17: (a): single particle self-energy, $\Sigma(\omega, 8K)$, extracted from the optical data. The cutoff energy in $\Sigma_2(\omega, T)$ at $\omega_c = 41$ meV introduces a finite slope of $\Sigma_1(\omega, T)$ at lower energy and a corresponding mass enhancement. (b): energy and temperature dependence of the effective mass of the annealed crystal corresponding to the optical scattering rate of Fig. 4.13d. The experimental mass enhancement is shown with solid lines, while the mass enhancement calculated from the Allen-Kubo formula is shown as dashed lines. The effect of the cutoff energy ω_c results in a mass enhancement $m^*/m(\omega \to 0) \approx 1.2$. Note that the data and fits are offset from their actual value with increments of 0.1 at successive temperatures above the 8 K curves. (c): (ω,T) dependence of $\Delta\sigma(\omega, T)$ for the as-grown crystal. The dome of zero-crossings is smaller compared to the annealed crystal. This difference is highlighted by the dashed (as-grown) and dashed-dotted (annealed) semi-circles calculated from $T_\infty(\omega)$. The dashed semi circle is calculated using the same parameters as in Fig. 4.16 except for $\Gamma_0 \approx 8$ meV and $p \approx 1.34$.

agreement between the experimental and calculated $m^*/m(\omega, T)$ therefore serves as a confirmation of the analysis presented in Fig. 4.13.

To conclude we discuss the deviation of p from the FL value $p = 2$. The most likely origin appears to be scattering of quasi-particles on weak, localized magnetic moments [101]. Such localized moments could be associated with the presence of Co impurities in the Fe lattice, although no local moment has been detected for Co impurities in $BaFe_2As_2$ [112]. Regardless the origin, this resonant elastic term has a strong influence on the normal state properties. Figure 4.17c displays $\Delta\sigma(\omega, T)$ for the as-grown crystal, displaying a suppressed dome of zero-crossings compared to the annealed crystal. The dashed semi-circle is calculated using exactly the same parameters as for the annealed case, except for a slightly higher $\Gamma_0 \approx 8$ and $p = 1.34$. This smaller value of p corresponds to a two-fold stronger elastic term in the single particle self-energy $\Sigma(\omega, T)$, indicating that annealing strongly reduces the influence of this scattering channel. Given the concomitant change in superconducting critical temperature, we suggest that this scattering channel could be pair-breaking, possibly providing an interesting direction for future work.

Chapter 5

From bad metal to Kondo insulator: temperature evolution of the optical properties of SmB_6.

5.1 From mixed-valent to topological Kondo insulator

Samarium hexaboride (SmB_6) is a well established mixed-valent compound at high temperature and a Kondo insulator at low temperature. SmB_6 recently gained a lot of attention due to the suggestion that it can host topological surface states, which makes this system the first strongly correlated material with a nontrivial topological electronic structure. After the original prediction that SmB_6 could host a topological Kondo insulating state and reports of the first tantalizing signatures in transport experiments, numerous new insights in its properties have been reported.

One of the techniques that might be able to disentangle the response of the surface states from the bulk carriers is time-resolved optical spectroscopy. We collaborated with the T-REX laboratory in Trieste with the goal to study the ultrafast electron dynamics in SmB_6. It was hoped that these experiments could give additional information on the formation of the Kondo state and possibly some hints on the dynamical properties of the surface states. To make the interpretation of these experiments more quantitative, I measured the equilibrium optical properties in our lab in Amsterdam. These experiments turned out to provide equally interesting results and will be the subject of this chapter.

Several optical studies of SmB_6 have been made in the past, which will be summarized in section 5.4. However, the renewed interest in SmB_6 has also resulted in new advances in single crystal preparation and has improved material quality. These high-quality crystals

enable us to provide a new view on signatures of the formation of the Kondo state in optical spectroscopy experiments. In this chapter, I will start with a brief discussion of the electronic structure of SmB_6 based on first principles calculations. This will be followed by a summary of the theoretical description of the (topological) Kondo insulator (TKIs). After this introduction to the physics of TKIs, I provide a brief overview of some key experimental results in section 5.3. The remainder of the chapter is devoted to the new results I obtained with a detailed study of the temperature dependent optical properties and a discussion of the key findings based upon these results.

5.2 Theoretical description of SmB_6

5.2.1 From first principle band structure to tight binding models

In this section, the band structure of SmB_6 calculated from first principles will be discussed, with as a reference the work of Antonov *et al.* [113]. Apart from providing detailed calculations, this work also provides calculations and predictions that are used to interpret the measured optical data.

Experimentally an average valence of 2.5+ is observed at low temperature, with the presence of both Sm^{2+} and Sm^{3+} being detected [114]. At higher temperatures, the valence increases and it appears that the 3+ valence dominates. Since there have been no reports of charge ordering, it is assumed that the valence for a given ion fluctuates between 2+ and 3+. This makes first principle calculations difficult to interpret, since such fluctuations cannot be captured in density functional type calculations. Antonov *et al.* investigate the impact of valence by performing the calculation for two different configurations (e.g. for a 2+ and 3+ configuration). They start by assuming an effective Coulomb interaction of 7 eV, based on photoemission and bremsstrahlung isochromat spectroscopy.

The calculation that most accurately describes SmB_6 is presented in Fig. 5.1. The top two panels show the band structure (Fig. 5.1a) and corresponding density of states (Fig. 5.1b) for the Sm^{3+} configuration, while the lower two panels show the results for the Sm^{2+} configuration. The SmB_6 band structure with Sm^{3+} configuration has the unoccupied $4f_{7/2}$ states pushed 1 eV above the Fermi level. A single unoccupied $4f_{5/2}$ level lies 0.34 eV above the Fermi level, as indicated in Fig. 5.1a,b, while the five occupied $4f_{5/2}$ states are hybridized with B $2p$ bands.

The divalent samarium configuration has eight unoccupied $4f_{7/2}$ states that are hybridized with the Sm $5d$ bands (see Fig. 5.1c,d). Fully occupied $4f_{5/2}$ bands were used

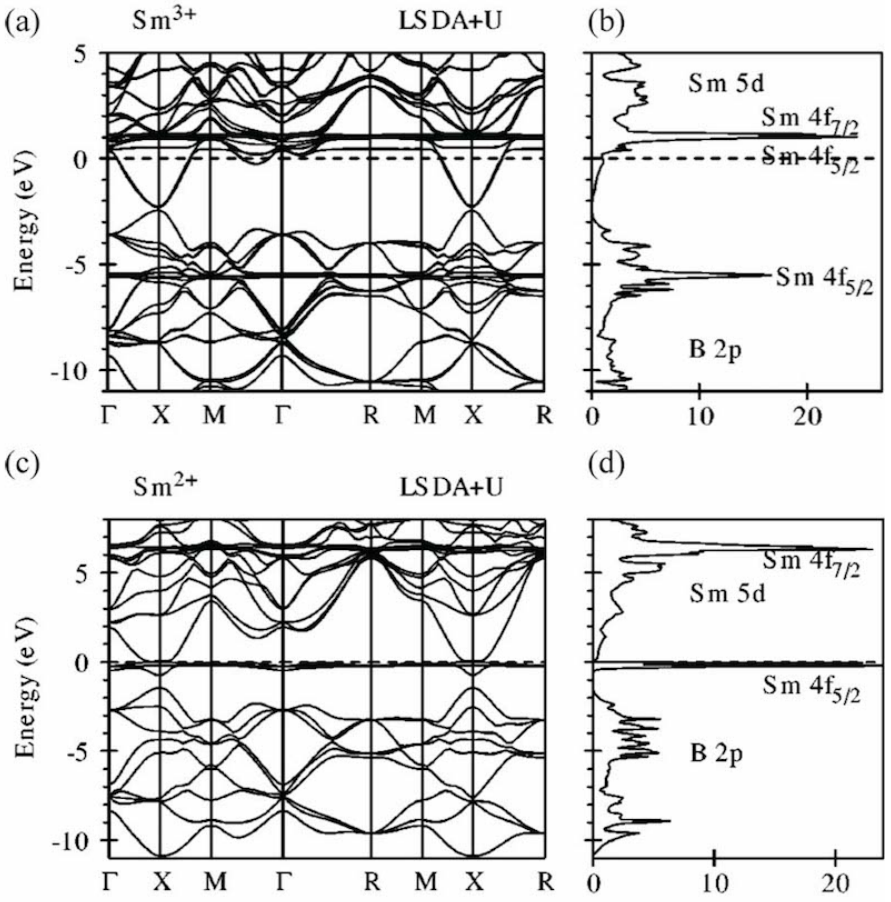

FIGURE 5.1: (a): LSDA+U electronic structure calculations for SmB_6 with Sm^{3+} configuration. (b): density of states corresponding to panel (a). The labels indicate the energy position of the $4f$ multiplet. (c): same as panel (a), but now for the Sm^{2+} configuration. (d): Corresponding density of states for panel (c). Note that in this case the $4f_{5/2}$ state straddles the Fermi level. The figure is taken from [113].

as a starting configuration. Subsequent self-consistent relaxation calculations result in a lifting of the degeneracy of the $4f_{5/2}$ states. The lifting of the degeneracy, in combination with the hybridization with $5d$ bands results in the opening of a semiconductor-like gap at the Fermi level. Based on their calculations, Antonov *et al.* provide a detailed comparison between the optical conductivity derived from the LSDA+U calculations and the optical conductivity presented in Ref. [115]. The observation is that the experimental results contain signatures of both the 2+ and 3+ valence states. As will be discussed in Sec. 5.5.3, the relative contribution of these two valence states appears to vary from crystal to crystal, but is in good agreement with these calculations.

Since the prediction of a possible topological Kondo insulating state in SmB_6, additional band structure calculations have been performed by other groups [116–118]. These works focused on the topological nature of SmB_6 and possess both some common conclusions

and also contain some differences. In the work of Takimoto [116] a tight-binding model is used to calculate the topological indices and surface spectra. It was shown that the SmB_6 (001) surface might have one Dirac cone at the Γ - point and one cone at each X - point in momentum space. Lu *et al.* [117] have performed LDA calculations within the Gutzwiller approximation. In agreement with Takimoto, they have shown that the SmB_6 (001) surface can host one Dirac cone at the Γ - point. In contrast, they find two at the X - point, where one of the X - centered Dirac cones is crossing the Fermi level and the second lies well below the Fermi level.

The surface termination dependence of SmB_6 has been investigated by Kim *et al.* [118] using density functional theory (DFT) slab calculations. They have shown that depending on the surface termination the surface states are formed differently. It is shown that the B - terminated surface hosts Γ - and X - centered surface states, in agreement with [117]. In contrast, a Sm - terminated surface is predicted to have additional surface states located at the M - point. I will return to a discussion of these aspects in section 5.3.3. Before proceeding, I will now first turn to the theoretical framework underpinning the (topological) Kondo state.

5.2.2 Kondo insulators

The Kondo effect was first described by Jun Kondo in 1967 [32]. This effect can occur in materials where a sea of conduction electrons interacts with localized magnetic moments. The interaction between spins of the conduction electrons and a localized magnetic moment occurs at low temperatures forming a non-magnetic Kondo singlet [4] (see also the discussion in Chapter 3). This leads to the formation of an additional scattering channel for the conduction electrons and, as a result, an increase of the resistivity at low temperature. Doniach [119] showed that strong Coulomb interactions in a multi-orbital model lead to a similar effect. This model has become known as the Kondo lattice problem or Kondo lattice model and has been widely studied. The Kondo lattice model describes localized states interacting with conduction electrons. When applied to SmB_6, the necessary ingredients are localized f - states hybridized with delocalized d - electrons. The originally flat $4f$ Sm band (shown in Fig. 5.2a) will mix (hybridize) with the highly dispersive $5d$ Sm band resulting in the opening of an energy gap, as shown in Fig. 5.2b. This effect only takes place at low temperatures making SmB_6 an insulator, while at high temperature thermal fluctuations destroy the Kondo state and SmB_6 behaves like a bad metal.

A theoretical description to explain the formation of the insulating state in SmB_6 was first given by Martin and Allen [8]. In their work the following aspects are taken into

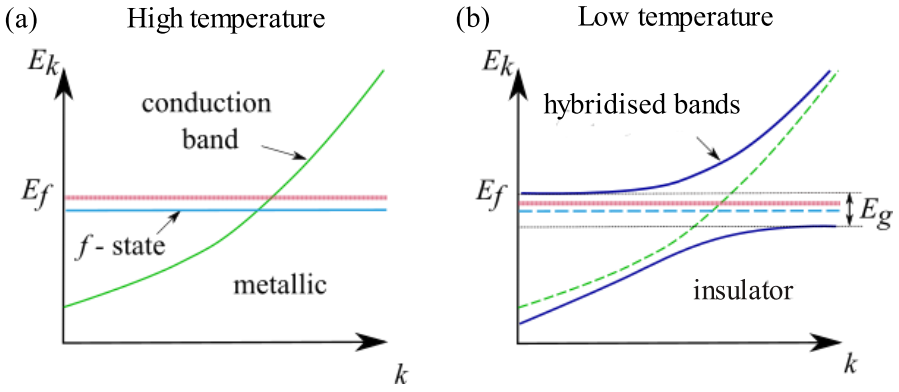

FIGURE 5.2: (a): schematic band structure of SmB_6 at high temperature, (b): schematic picture of band hybridization resulting from the Kondo interaction.

account: a broad conduction band, a lattice of localized f states with a large on-site Coulomb repulsion U between them, and an interaction between the conduction and f electrons. In their model a Hamiltonian is presented as follows [120]:

$$H = \sum_{k,\sigma} E(k) c^{\dagger}_{k\sigma} c_{k\sigma} + \sum_{j,\sigma} [E_f f^{\dagger}_{j\sigma} f_{j\sigma} + \frac{1}{2} U n^f_{\sigma} n^f_{-\sigma}] + \sum_{j\sigma} V[c^{\dagger}_{j\sigma} f_{j\sigma} + c_{j\sigma} f^{\dagger}_{j\sigma}] \qquad (5.1)$$

The first term describes the kinetic energy of the conduction electrons, where $E(k)$ is an energy dispersion, $c^{\dagger}_{k\sigma}$ ($c_{k\sigma}$) creates (annihilates) an electron with momentum k and spin $\sigma = \uparrow, \downarrow$. The second term of the Hamiltonian describes a set of localized f state with energy E_f and on-site Coulomb repulsion U. n^f_{σ} is the occupation number and can take on a value between 0 and 1. The sum over j runs over lattice sites with f-states. The original case considered by Kondo featured a single impurity ion with an f-state. The lattice problem considered by Doniach featured a crystal where the f-states form a periodic array, but it is also possible to consider a random distribution of f-states. The last term in Eq. (5.1) describes the hybridization between the conduction band and the f states, where V is the hybridization strength.

Considering this model in the limit $U \rightarrow 0$ one obtains a hybridized band with an indirect gap $E_g = 2V$, as shown in Fig. 5.2b. The survival of this gap for finite U was explained by Martin and Allen by referring to Luttinger's theorem [8]. According to Luttinger's theorem, the volume enclosed by the Fermi surface remains constant when interactions are included. Starting with $U = 0$, but finite V, and an even number of electrons we know that we have a band insulator with the Fermi level lying in the energy gap. Therefore, the Fermi surface volume is zero and according to Luttinger's theorem will remain zero even in the presence of interactions. This general argument holds as long as bands do not cross the Fermi level.

5.2.3 Topological Kondo insulators

After the initial discovery of the role played by topological invariants in characterizing the electronic structure of solids, several groups considered the application of these concepts to materials where strong electron-electron correlations play an important role [53, 121–125]. One of the first works where the interplay between interactions and topological properties was considered was the work by Dzero *et al.* [53] on the topological Kondo insulator. As discussed above, in a Kondo insulator, the interaction between mobile conduction electrons and localized (f - electron) moments results in hybridization of the mobile and localized states as described above (section 5.2.2). Dzero *et al.* showed that under certain conditions this could lead to the formation of a topological state in close analogy to the topological insulating state formed in 3D TI's with inversion symmetry. In other words, by combining the theory of Kondo lattices (section 5.2.2) with the topological invariants derived from discrete crystal symmetries (see Ch. 3), Dzero *et al.* showed that a non-trivial topological state can arise in the insulating gap created by the exchange interaction. Dzero *et al.* begin their discussion with the periodic Anderson model [53]:

$$H_{ALM} = \underbrace{\sum_{ij\sigma} t_{i,j}^{(c)} c_{i\sigma}^{\dagger} c_{j\sigma}}_{\text{conduction band}} + \underbrace{\sum_{ij\alpha} t_{i,j}^{(f)} f_{i\alpha}^{\dagger} f_{j\alpha} + \frac{U_f}{2} \sum_{i\alpha\alpha'} \hat{n}_{i\alpha}^{f} \hat{n}_{i\alpha'}^{f} +}_{f \text{ electron system}}$$
$$\underbrace{+ \sum_{ij} \sum_{a\sigma\alpha} (V_{ia\sigma,j\alpha} c_{i,a\sigma}^{\dagger} f_{j\alpha} + V_{i\alpha,ja\sigma} f_{i\alpha}^{\dagger} c_{j,a\sigma})}_{\text{hybridization term}}$$

where $t_{i,j}^{(c)}$ and $t_{i,j}^{(f)}$ are hopping amplitudes for conduction and f electrons respectively. $\hat{n}_{i\alpha}^{f}$ is the f-electron density operator. The index α denotes f multiplet components, as will be discussed further below. Thus, $f_{i\alpha}^{\dagger}$ ($f_{j\alpha}$) creates (annihilates) an f electron on site j in the α state of the multiplet.

The authors of [53] note that to determine the topological invariants for the Kondo insulator requires taking into account the crystal field splitting of the f-states that results in a multiplet structure for the f-states. This means that the degeneracy of the f orbitals is lifted as a result of the local electric field environment generated by neighboring ions. Hence, the specific multiplet structure depends on the crystal structure. In Ref. [53] the authors consider a tetragonal lattice, while in Ref. [126, 127] they also consider a cubic lattice.

Depending on the choice of lattice, the lowest f-multiplet state are Kramers doublets (tetragonal lattice) or a doublet and a quartet (cubic lattice). Importantly, for both

choices of lattice the e_g states (i.e. the $d_{x^2-y^2}$ and $d_{z^2-r^2}$ orbital) are lowest in energy. This means that the d and f states hybridizing with each other have opposite parity. It is this fact that enables the authors to invoke Fu and Kane's argument [42] to determine the invariants discussed in Ch. 3.

However, in contrast to the simpler case of 'non-interacting' sp^3 orbitals considered in Ref. [46], the hybridization between d orbitals and strong spin-orbit coupled f multiplets introduces an additional complication. The over-simplified picture in Fig. 5.2 sketches the hybridization gap for a simple mono-atomic, one dimensional chain. In a 3D crystal with additional lattice symmetries, the hybridization gap becomes a complicated function of momentum (much like the momentum dependent SC gap discussed in the chapter on pnictides). In particular, the gap follows the symmetry of the f - multiplet involved in the hybridization and can even acquire nodes (signaling additional inversions). It is therefore not possible to make completely general statements that will hold for any type of lattice or filling. Indeed, one needs to consider the particular details of a given compound and determine the topological invariants by explicit calculation of the invariants from the full wavefunctions. Since this chapter is concerned with the case of SmB_6, we will focus on the cubic lattice case as discussed in Ref. [127]. As mentioned above, for a cubic lattice the $J = 5/2$ orbitals of the $4f$ state split into a doublet and quartet. For Sm, the doublet is fully occupied and unimportant to our discussion. The quartet is formed from the original orbitals as:

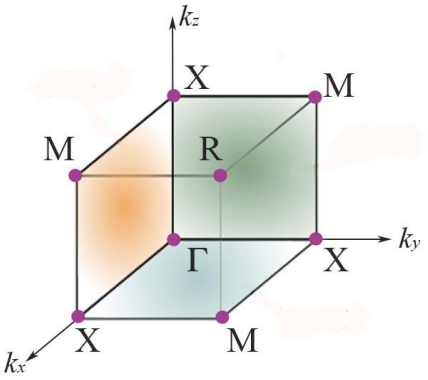

FIGURE 5.3: Schematics of the Brillouin zone of the cubic unit cell. The high symmetry points are marked by dots.

$$\left|\Gamma^{(1)}\right\rangle = \sqrt{\frac{5}{6}}\left|\pm\frac{5}{2}\right\rangle + \sqrt{\frac{1}{6}}\left|\mp\frac{3}{2}\right\rangle \tag{5.2}$$

$$\left|\Gamma^{(2)}\right\rangle = \left|\pm\frac{1}{2}\right\rangle \tag{5.3}$$

These four states are degenerate at the Γ-point [(k_x, k_y, k_z)=(0,0,0)] and at the (π, π, π) or R-point of the 3D Brillouin zone (see Fig. 5.3), because there the spin-orbit interaction vanishes. Away from these points the four states split into two doublets. The e_g states also form a 'quartet': since we are interested in the Kondo insulator, spin is an important quantum number and we should label the e_g states as $|3d_{x^2-y^2}, \pm 1/2>$ and $|3d_{z^2-r^2}, \pm 1/2>$.

Since the f states have odd parity and they are forced to be fourfold degenerate at the Γ and R points of the Brillouin zone, the parity at these point will always be $\delta_\Gamma = 1$ and $\delta_R = 1$ (see Ch. 3 for the definition of δ_i). This restriction does not hold at the X and M points and it is therefore possible to have a different order of the states, resulting in a band inversion. In the cubic lattice case we have 3 X points and 3 M points, we can thus conclude that a strong topological insulator is formed if $\delta_X \cdot \delta_M = -1$, because then $(-1)^{\nu_0} = \delta_\Gamma \cdot \delta_R \cdot (\delta_X \delta_M)^3 = -1$. So, an inversion at either the X or the M point always leads to a strong topological insulator.

The remaining condition to determine whether SmB_6 is a topological Kondo insulator or not requires knowledge of the electronic configuration of the Sm ions ($4f^5$ and $4f^6$ for Sm^{2+} and Sm^{3+} respectively) and a determination of the precise energy position of the Γ multiplet with respect to the d-orbitals at the X and M points. The LSDA calculation of Antonov *et al.* [113] (see section 5.2.1) shows that the quartet at the X-point splits into two doublets, one of which shifts above the Fermi level. It is this shift of one doublet at X from below E_F for $T > T_K$ to above E_F for $T < T_K$ that causes the topological invariant to change sign, giving rise to surface states at the three X points of the Brillouin zone.

5.3 Experimental signatures of the topological Kondo insulator.

There is a tremendous amount of experimental information available for SmB_6, highlighting the many aspects of the physics of this complicated compound. Kondo physics, mixed valence fluctuations and now a possible topological connection have all been studied with a variety of experimental techniques. In this section we will provide a brief overview of some results. Some important results will undoubtedly, but not purposefully, have been omitted.

5.3.1 Transport measurements

The first resistivity measurements on SmB_6 were performed in the 1960's [128, 129]. It was shown that with decreasing temperature the resistivity increases exponentially below 50 - 60 K and saturates below approximately 3 - 5 K (see Fig. 5.4 for a recent measurement). Since then, many other studies have confirmed these general features [130–143]. The sharp increase in the resistivity was linked to the formation of a Kondo insulating state [4]. The resistivity plateau has remained unexplained for a long time

and the proposal by Dzero *et al.* [53], as discussed in the preceding sections, offers a possible interpretation where the surface states emerging inside the Kondo gap result in a 'shorting' of the resistivity.

To exclude an extrinsic origin for the resistivity plateau, improving the crystal quality is crucial. As an example, Hatnean *et al.* [132] used the floating zone technique to grow high quality SmB_6 crystals. The main difference compared with previous studies was the use of high power Xenon arc lamps to reach the melting temperature of SmB_6, which is around 2400 ± 100 °C. This crystal was free of any contamination as shown by energy-dispersive X-ray spectroscopy and single phase as shown by powder X-ray diffraction.

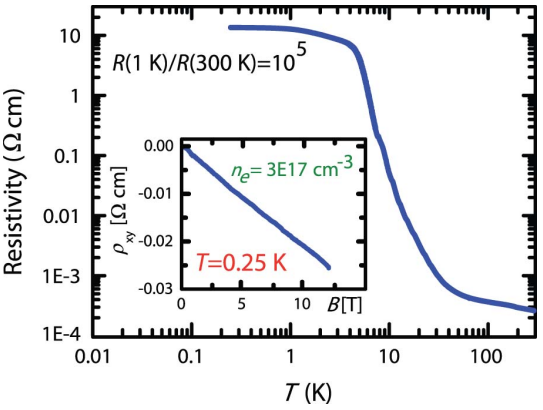

FIGURE 5.4: Temperature dependent resistivity of SmB_6 as measured on a sample taken from the same batch as the one used in this chapter. The inset displays the Hall resistivity indicating an n-type charge carrier concentration. The figure is adapted from [144].

Figure 5.4 shows the temperature dependent resistivity taken from [144], where the measurements were performed on a high quality sample also grown by the floating-zone technique [145]. The Hall resistivity in the saturation regime shows linear dependence on the magnetic field, indicating an n-type carrier concentration of about $n_e = 3 \cdot 10^{17}$ cm^{-3}.

Recent work presented by Tan *et al.* [137] shows a paradox in magnetic torque measurements. These quantum oscillation experiments remain unexplained till now, but provide evidence for a three dimensional Fermi surface at low temperature. However, the presence of such a Fermi surface is in clear contradiction with a Kondo insulating state. It was observed that between 2 K and 25 K the quantum oscillation amplitude exhibits a Lifshitz-Kosevich like temperature dependence [146]. At lower temperatures ($T < 2$ K) instead of saturating, it reveals an abrupt upturn with decreasing temperature. This observation has not found a conclusive explanation and requires further investigation.

5.3.2 Complexity of the SmB_6 surface

The key technique to detect signatures of topological states is angle resolved photoemission spectroscopy (ARPES). Since this is a surface sensitive probe, we will first discuss the surface structure of SmB_6. The crystal structure, (shown in Fig. 5.5a) of SmB_6 does not possess a natural cleavage plane, which implies that cleavage can occur either

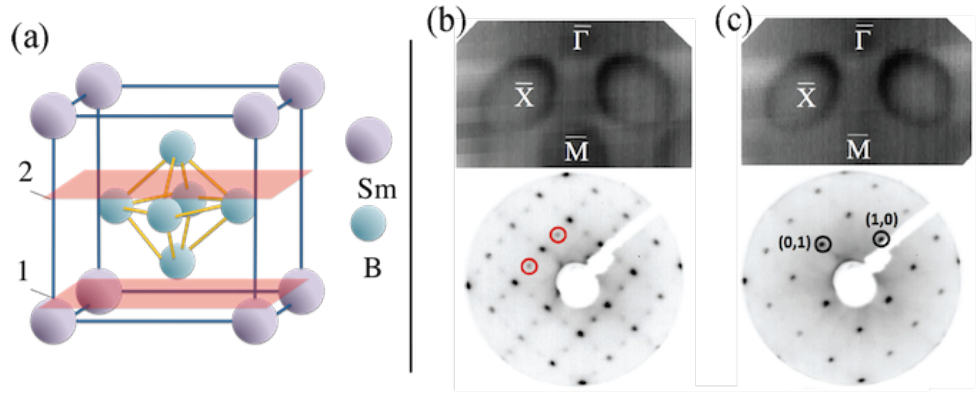

FIGURE 5.5: (a): crystal structure, 1 - cleavage plane between the Sm and B planes, 2 - the cleavage plane lies within a B octahedron. (b): ARPES and LEED data taken from freshly cleaved (001) SmB_6 surface at 37 K [148]. The labels represent high-symmetry points of the Brillouin zone. ARPES data reveals elliptical electron pockets located at the $\bar{X}$ - point and additional feature at the $\bar{M}$ - point. The LEED data show 2×1 periodicity. (c): ARPES and LEED data at the same spot 5 hours after the cleaving process. The LEED data show 1×1 periodicity and ARPES data no longer contain features at the $\bar{M}$ point (figure adapted from [148]).

in between the Sm and B planes, indicated by plane (1) in Fig.5.5a, or within a B octahedron, indicated by plane (2) in Fig. 5.5a. To break the covalent bonds inside the B octahedron requires more energy than to break the ionic bonds between Sm atoms and the B octahedra, thus plane (1) would be more favorable. Considering that on a macroscopic scale both sides of a cleave will be chemically equivalent, plane (1) would lead to the presence of both Sm- and B_6-terminations on a cleaved sample surface. In addition to such general considerations, a pure Sm- or B_6-terminated surface would be polar and thus unfavorable with respect to the minimization of its total energy. The energy of a finite crystal of such a polar system will possess an electrostatic potential which increases with thickness of the system. This would entail a diverging surface energy preventing the existence of pure surface termination [147]. However, energetic stabilization can be achieved on Sm- or B_6-terminated surfaces through a structural or electronic reconstruction.

For instance, the polar instability of the Sm-terminated surface could be resolved by equally dividing the Sm plane between the two cleavage surfaces, leading to 2×1, 1×2 or $\sqrt{2} \times \sqrt{2}$ surface reconstructions. These surface reconstructions have been observed by STM topography [136, 149, 150], and LEED studies of cleavage surfaces of SmB_6 [148] (shown in Fig. 5.5b), as well as in one of the ARPES studies [151]. The STM study presented by Ruan et. al [152] shows $\sqrt{2} \times \sqrt{2}$ surface reconstructions as well as unusual doughnut-like patterns. This finding emphasizes the complexity of the SmB_6 surface structure. Such surface reconstructions can affect the surface electronic properties and might conceal the true electronic properties of the bulk or at least provide a topological

trivial route by which the surface electronic structure differs from that of the bulk. This makes the interpretation of the SmB_6 results from surface sensitive techniques quite challenging.

In addition, although the domain size of the different surface reconstructions can extend over several micrometers, the size of the light spot in most ARPES measurements is larger than several tens of microns. This means that the resulting ARPES data are likely to be a combination of the different spectra coming from the various surface terminations and reconstructions.

Another issue that can complicate surface sensitive studies is a possible time dependence between cleaving process and measurements itself. By combining LEED and ARPES data, Ramankutty *et al.* [148] have shown that 2×1 and 1×2 reconstructions of the cleaved SmB_6 surface can relax over time, even under UHV conditions. The freshly cleaved [001] surface exhibits long-range order with a periodicity of 2×1 and 1×2 (Fig. 5.5b), while after 5 hours the same spot of the cleaved surface reveals only 1×1 periodicity, as shown in Fig. 5.5c. The ARPES data obtained 5 hours after cleaving displays elliptical electron pockets located at the $\bar{X}$ symmetry point, while freshly cleaved surface exhibits an additional feature around $\bar{M}$ - point. These time-dependent changes have been explained by possible surface relaxation through absorption of the residual gases present in vacuum. Time-dependent data is also presented in [147], where the changes in the ARPES data over time are related to the self-annealing of the SmB_6 cleaved surface. From these studies, it is clear that the [001] cleavage surface of SmB_6 is both complex and temporally unstable, and thus the time interval between the cleavage itself and the measurements is also an important factor that should be taken into account before making any conclusion from the measured data.

Another effect that should not be forgotten is band bending, that can occur in systems with inhomogeneous charge distributions into the depth of a cleaved crystal, arising, for example from the existence of surface states. This band-bending can lead to the spatial confinement and even quantisation of the bulk electronic states and is also able to result in complex spin-momentum structures. Band bending has been observed for some hexaborides [148, 153], so that the possible presence of band bending at the surface of SmB_6 should not be ignored.

5.3.3 Angle-resolved photoemission spectroscopy studies of SmB_6

With a good understanding of the surface structure we can now turn our attention to the signatures of topological surface states in SmB_6. However, we will first introduce angle resolved photoemission spectroscopy (ARPES). ARPES is one of the few direct

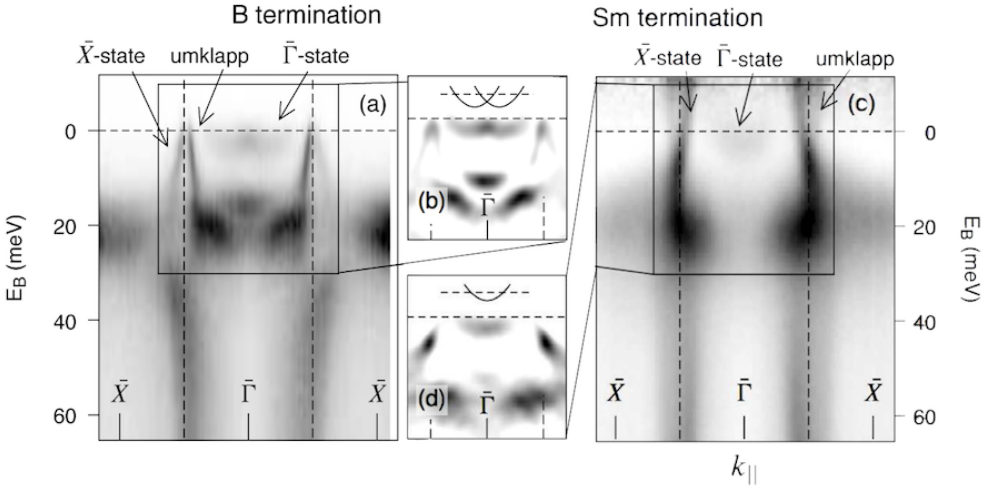

FIGURE 5.6: Energy dispersion for a B_6 terminated surface (a) and for a Sm terminated surface (c). (b), (d) are the second derivatives (d^2I/dE^2) of the selected regions from (a) and (c) respectively, where solid lines indicate Rashba split (b) and simple (d) parabolic dispersions. (Figure adapted from [164]).

probes to measure the band structure of solid materials. By measuring the kinetic energy and emission angle of the photo-emitted electrons, information can be obtained about the binding energy and the in-plane crystal momentum of the electronic states inside a crystal. Additional information such as the spin polarization of the states can be obtained by the spin-resolved APRES [154]. Being a surface sensitive probe, ARPES has been proven to be the perfect tool to measure topologically protected surface states of 3D topological insulators [50, 155, 156].

As was mentioned in the previous sections, SmB_6 has been predicted to be a topological Kondo insulator. In an attempt to confirm this, several ARPES measurements have been performed on cleaved single crystals of SmB_6 [144, 147, 151, 157–164]. Although most of the experiments agree on the global electronic structure, the observation of topological surface states has been a subject of quite some debate. This is a consequence of the complicated cleavage surface as was discussed in the previous section. Although most groups have indeed observed states that be termed 'surface states', the determination whether these states are trivial or topological is complicated. In the next section we will discuss observations hinting to trivial surface states, followed by a discussion of topological surface states in section 5.3.5

5.3.4 Trivial surface states in SmB_6

Surface states that are not expected from bulk band structure calculations have been associated with the existence of trivial surface states. Zhu *et al.* [147] proposed a

polarity-driven scenario for the surface states. Their DFT slab calculations show that surface states originating from the B-2p dangling bonds are present for both Sm and B_6 terminations of the cleavage crystal. Unoccupied surface states originating from boron dangling bonds might be pushed below the Fermi level at the $\bar{\Gamma}$ point due to an electronic reconstruction, which results in surface metallicity driven by avoidance of the creation of polar surface.

In the work presented by Frantzeskakis *et al.* [144] several states crossing the Fermi level have been observed from the unreconstructed SmB_6 surface (the measured LEED pattern from the cleaved surface shows 1×1 surface structure). One of these states is located at the $\bar{\Gamma}$ point in the hybridization region between the $5d$ and $4f$ states. Other states are found at the $\bar{\mathrm{X}}$ - point. These latter states have a strong $k_\perp$ dependence, indicating a bulk origin. The Fermi surface lies 20 meV above the hybridization region.

The Frantzeskakis *et al.* results [144] have been confirmed by Hlawenka *et al.* [164]. They further show that at binding energies well beyond the f multiplets (at 75 and at 260 meV) other features at the $\bar{\mathrm{X}}$ - point are found, besides the bulk states. These states have no $k_\perp$ dependence, indicating their two-dimensional character. In Hlawenka *et al.* [164], a state close to Fermi level (at a binding energy of $\sim$ 2.3 meV) has also been found at the $\bar{\Gamma}$ point (see Fig. 5.6). The topological origin of these states was ruled out based on two observations. Firstly, the surface state does not connect to the valence band. The second, and more important reason for excluding a topological origin of this state comes from the termination dependence. The Sm terminated surface features a single parabolic state, as can be seen in Figs. 5.6c and 5.6d. It thus seems likely that the double branch observed at the $\bar{\Gamma}$ point for a B_6 terminated surface results from Rashba splitting. Additional states located along the $\bar{\Gamma} - \bar{\mathrm{M}}$ direction have been found by Denlinger *et al.* [162]. The observed surface states have been associated with tails of spectral intensity coming from the bulk $4f$ states, which are gapped at low temperature. In Ref. [162], a detailed temperature dependent ARPES measurement is also presented. They show that the conduction band shifts in energy as the temperature is changed, and crosses the Fermi level signaling the opening of a gap at ≈ 60 K. Starting from the lowest temperature data reported ($T = 6$ K) as the temperature increases, the conduction band first appears 9 meV above the Fermi level (at 25 K) and then shifts to 6 meV below the Fermi level (at 100 K). A second observation is that with increasing temperature the Sm $4f$ states lose their coherence. As will be discussed further in this chapter, this last observation is consistent with our optical data.

5.3.5 Topological surface states in SmB_6

Some ARPES studies have attributed the observation of surface-related electronic states to topological surface states [151, 157–161]. For instance, Neupane *et al.* [158] have observed one in-gap state at the $\bar{\Gamma}$ point and one at each of the two $\bar{X}$ - points in the surface Brillouin zone. They have shown that thermal cycling in the Kondo regime from 6 to 50 K shows a systematic appearance and disappearance of the in-gap states at temperatures around 15 K. They argue that together with the odd number of in-gap states, this provides an indication of a strong topological insulating state. However, this study, like all the other ARPES studies, has not provided a clear observation of a Dirac point in the surface state dispersion.

Direct evidence of the topological nature of the surface states would be the observation of their spin texture, an analysis which can be performed using spin-resolved ARPES. In the research presented by Xu *et al.* [151], the authors argue that the observed states at $\bar{X}$ points are spin-momentum locked. However, such conclusion is hard to make due to the high demands as regards the energy and angle resolution. On average, the current best spin-resolved ARPES instrumentation has an energy resolution about 30 meV - 60 meV (in Ref. [151] energy resolution is 60 meV). The angular resolution is commonly set to be about 0.5°-1° for the synchrotron measurement, which would translate to 0.02 - 0.04 $\mathring{A}^{-1}$ for a photoelectron kinetic energy of 20 eV. The topological surface states of SmB_6 would show their characteristic "X" like dispersion in a hybridisation gap of order 10 meV. To be able to show the presence of the spin-momentum locked states located in such small gap, a resolution of 5 meV or better is required, which is far beyond current spin-resolved ARPES instrumentation.

Also, we would like to mention that no quasiparticle interference (QPI) has been directly visualized in SmB_6 [152], which should show characteristic features if the cleavage surface is structurally crystalline and possessing spin-momentum locked surface states. From all above mentioned arguments, it is clear that direct, spectroscopic evidence of the topological nature of the SmB_6 surface states is still controversial.

5.3.6 Quantum oscillations vs. ARPES

Since ARPES is a surface sensitive probe, a comparison with bulk sensitive probes such as transport experiments might shed light on the interpretation of the ARPES data. The first magneto - torque oscillation measurements on SmB_6 were presented by Lu Li *et al.* [165]. In these measurements, de Haas-van Alphen oscillations in the magnetisation of SmB_6 have been detected with the oscillation frequencies up to 1 kT. The data present

the change of the oscillation frequency as a function of the tilt angle in the range more than 180° which goes around the crystalline $\hat{a}$ - $\hat{c}$ plane. The angular dependence of the oscillating frequency follows the inverse of a cosine function suggesting the two - dimensional nature of the SmB_6 electronic states at low temperature. The extrapolation of the Landau level indices shows -1/2 at the high field limit, suggesting a non-trivial Berry phase of π. However, the obtained Fermi surface areas are only 0.2% (for the α pocket from the [001] surface) and 1.23% (for the β pocket from the [101] surface) of the 2D Brillouin zone, which is much smaller than the most prominent features observed by ARPES (for instance 33% for X-states detected in Ref. [144] and [157]).

Later magnetic torque measurements [137] already discussed in section 5.3.1 indicated a three-dimensional Fermi surface and no Berry phase. The reported data present frequencies up to 15 kT with angular dependence over a 90° range along a diagonal plane. By contrast to Ref. [165], the observed frequency of the quantum oscillation is greater than 10 kT, corresponding to approximately half of the Brillouin zone volume. This finding is much closer to the 33% (for $\bar{X}$-states) observed by ARPES [144, 157].

A direct comparison between quantum oscillation measurements and ARPES data was recently presented by Denlinger *et al.* [166]. In this work, an analysis of the quantum oscillations results from both groups [137, 165] has been made. By comparing their own ARPES results of the Fermi surface to the quantum oscillation data, the authors of Ref. [166] conclude that the 2D model is the better one. Nevertheless, the need for more research is also stressed [166].

The literature reviewed in this section goes to show that the surface of SmB_6 is too complicated to make firm conclusions when based only on data from surface sensitive techniques. Consequently, additional information from bulk-sensitive experiments, probing the electronic structure might improve our understanding of the physics behind such a complex compound as SmB_6.

5.4 Optical properties of SmB_6

Another powerful tool to measure the electronic structure of solids is optical spectroscopy. Previous optical measurements of SmB_6 have been reported by several groups [115, 167–174]. It was shown that at high temperature the optical conductivity at low energy exhibits a Drude-like response indicating free charge carriers. At low temperature, the opening of an energy gap has been observed. In the work of Nanba *et al.* [115] the optical conductivity displays three main interband transitions at 0.12, 0.5 and >5 eV. In Ref. [169] measurements up to 12 eV show one additional interband transition

at 10 eV. The two low energy interband transitions also have been observed in our data and will be discussed further in this chapter.

The next point that we would like to mention is the determination of the (optical) energy gap. In the work of G. Travaglini and P. Wachter [173] the energy gap was determined to be 4.7 meV, while later data [115, 169, 171] showed an energy gap of order 13-15 meV. Some of these works [115, 171] based on transmission experiments, suggested a finite conductivity resulting from an absorption band around 4 meV. We can take the optical energy gap of order ≈15 meV as a measure of the energy gap in the density of states around the Fermi level. Therefore, a finite optical conductivity at lower energy must be a result of optical transitions between states within this energy gap and the unoccupied states just above the energy gap. In the earlier works the absorption was attributed to optical transitions between localised impurity states and the conduction band. This was subsequently investigated by Gorshunov *et al.* [170], who accurately measured the temperature dependence of the optical conductivity between 3 K and 20 K using sub-millimeter transmission experiments. They combine their experiments with Hall data in an effort to pin-point the source of the finite sub-gap conductivity. The combination of optical and transport data allowed them to determine the spectral weight, effective mass, carrier density, scattering rate and mobility of these carriers as function of temperature under some assumptions. They conclude that all data below 8 K are consistent with the exponential freezing out of impurity carriers as expected within a variable range hopping model.

More recently this interpretation has been questioned by Laurita *et al.* [174]. These authors use time-domain THz spectroscopy in the range from 1 - 8 meV to probe the complex optical conductivity. Their measurements are taken at several temperatures between 1.6 K and 20 K. At these low temperatures one expects the optical conductivity to vanish due to the opening of the Kondo gap at the Fermi level. In agreement with previous work they find a finite conductivity even at the lowest measured temperature. By examining the temperature and frequency dependence of the optical conductivity they also find qualitative agreement with a variable range hopping model. However, they conclude that quantitatively such an interpretation is hard to maintain. Within the context of the topological Kondo insulator, this naturally leads to an alternative explanation involving conductivity arising from the (topological) surface states. Based on a simplified model of the optical response of a system consisting of surface state - bulk - surface state layers, they rule out this possibility. For both surface states a 2D Drude response was assumed. To get agreement between this model and the data requires the surface states to have a sheet resistance larger than 1000 Ω. This value is much larger

than the reported sheet resistance $R_\square = 250\ \Omega$ for SmB_6 [175] or $R_\square = 200\ \Omega$ for other topological insulator such as Bi_2Se_3 [65, 176].

The authors of Ref. [174] discuss a few other possible interpretations. Although the physical origin of the finite conductivity remains unclear, these experiments provide further evidence for a possible low temperature metallic state. The low temperature Fermi surface observed in quantum oscillation experiments [137], discussed in section 4.3, implies that deep in the Kondo insulating state bands cross the Fermi level. Optical transitions within such a band are expected to give rise to a Drude peak in the optical conductivity. As will be discussed further in this chapter, we also observe a Drude peak at high temperature that collapses below the Kondo temperature. At the lowest temperature in our experiment (14 K) our data indicates a finite conductivity at the lowest temperatures. We observe a much larger conductivity below the gap edge (400 $\Omega^{-1}\text{cm}^{-1}$) compared to the data of Ref. [174] (55 $\Omega^{-1}\text{cm}^{-1}$), but this could be a result of our relatively large error bar at these low frequencies. The zero crossing of $\epsilon_1(\omega)$ in our data at 14 K (inset Fig. 5.11a) is the signature of a narrow Drude peak present in our optical data. The estimated width, $1/\tau$, of this Drude peak ($\sim$ 10 cm^{-1}) and plasma frequency ($\omega_p \approx$1100 cm^{-1}) are in agreement with data presented in [174] where at 14 K a Drude peak can be seen with a width of 0.5 THz (=16 cm^{-1}). These observations together with the Fermi surface observed by another bulk probe [137] provide a real challenge to our current understanding of the true ground state of SmB_6.

5.5 High resolution optical study of the Kondo to bad metal transition.

This brings me to a discussion of my own measurements of the temperature dependence of the optical properties of SmB_6. I will start with a discussion of the reflectivity measurements of SmB_6 and then present an analysis of the optical conductivity and dielectric function derived from them. As the temperature below which surface states are expected to become detectable is below the lowest temperature achievable in our setup, we instead focus on the changes in the optical spectra related to the formation of the Kondo insulating state.

In our experiments we have observed, for the first time, an infrared mode at 19.4 meV. This mode is associated with the motion of Sm ions against the B_6 cages. Furthermore, we found that as temperature is decreased, the incoherent metallic response first becomes more coherent but then collapses below approximately 60 – 70 K. The total amount of spectral weight lost in the metallic response corresponds to approximately 0.076 carriers

per SmB_6 unit and is not recovered in the entire energy range of the optical spectra (up to 4.35 eV). Based on a simple tight binding calculation we rule out kinematic effects associated with the hybridization gap as the cause for the lost spectral weight. Instead, we suggest that strong correlation effects, associated with the effective Coulomb interaction U, are responsible for the transfer of spectral weight to very high energies that has thus far not been observed in mixed valence Kondo insulators.

This crystal used in this work was taken from a single crystal boule that was grown by the floating-zone technique (for details see Ref. [145]). To obtain a large mirror-like surface, we first oriented the as-grown boule using Laue diffraction. We then made a slit using spark erosion, cutting on the side of the crystal along the (100) oriented plane and subsequently cleaved the crystal as done in previous ARPES experiments [144]. This resulted in a large (5 mm diameter) flat surface oriented perpendicular to the [001] direction.

5.5.1 Reflectivity data

Reflectivity spectra for selected temperatures are shown in Fig. 5.7. Figure 5.7a shows the reflectivity over the full spectral range measured. The most prominent changes as function of temperature take place in the low frequency part of the spectrum (displayed in Fig. 5.7b). However, at higher photon energies a clear shift of the plasma edge is visible between 1 and 2 eV. Above the plasma edge several structures in the reflectivity point to interband transitions. Figure 5.7b shows the reflectivity below 0.2 eV, where the effects due to the formation of the Kondo state at low temperature are most prominent. Overall the spectral features agree with previously published data [115, 170, 172, 173], but there are also significant differences as we will discuss further below. At room temperature the reflectivity scales according to the expectation for a metal, namely as $R(\omega) \approx 1 - 2\sqrt{\omega/\sigma_{\mathrm{DC}}}$ (i.e. Hagen - Rubens behavior), with σ_{DC} the DC conductivity. We extracted σ_{DC} by fitting the Hagen-Rubens relation to the low energy $R(\omega)$. It agrees to within a factor 2-3 with the DC resistivity measured on a different crystal taken from the same boule (data reported in Ref. [144]).

At room temperature, Hagen-Rubens (HR) behavior persists up to about 12 meV, but we expect the HR scaling to eventually break down below a certain temperature due to the opening of the hybridization gap. We estimate this temperature scale as follows: we fit the low frequency reflectivity to the relation $R(\omega, T) = A(T) - B(T)\sqrt{\omega}$ and determine $A(T)$ and $B(T)$. The functions $A(T) = 1$ and $B(T) = \sqrt{4/\sigma_{\mathrm{DC}}}$ in the Hagen-Rubens limit. From $B(T)$ we obtain $\rho_{\mathrm{DC}}(T)$, while a deviation of $A(T)$ from 1 is taken as an indication for the opening of the hybridization gap. We can directly compare

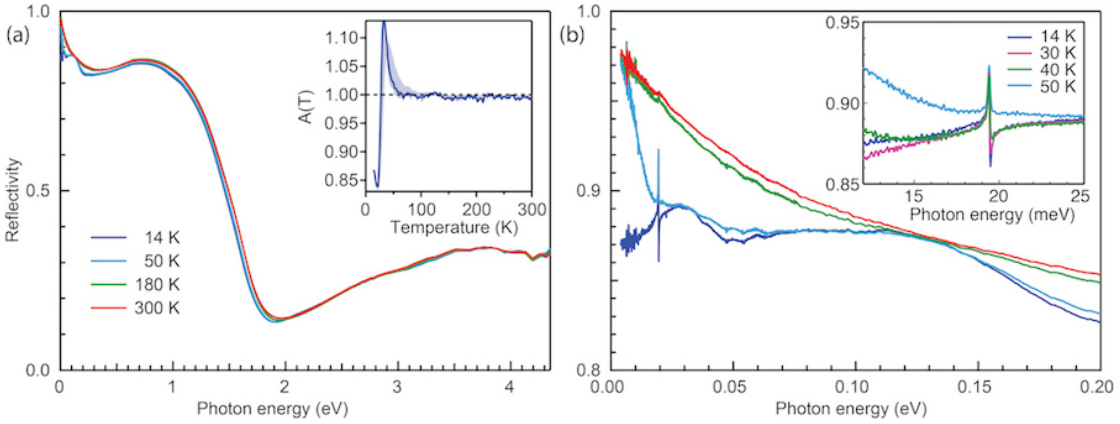

FIGURE 5.7: (a): The reflectivity of SmB_6 at selected temperatures over the full frequency range measured. A small shift in the plasma edge is visible, as well as temperature dependent changes in the UV range. The inset shows $A(T)$ (discussed in the text). The deviation of $A(T)$ from 1 indicates the temperature below which Hagen-Rubens (HR) behavior is lost. The light shaded region indicates the range of values obtained for $A(T)$ by changing the fitted frequency range. (b): Low frequency reflectivity at the same temperatures as in panel (a). With decreasing temperature a minimum develops below the isobestic point around 0.13 eV. At the lowest measured temperature (14 K) the reflectivity spectra resembles those of a semiconductor. The sharp line visible at low temperature around 20 meV is the T_{1u} vibrational mode, which is shown in more detail and at different temperatures in the inset.

$\rho_{DC}(T)$ obtained from our fits to the temperature dependent resistivity reported in Ref. [144]. Apart from a (temperature independent) scaling factor ≈ 2.7, we obtain excellent agreement between these two measurements if we restrict the photon energy range used in the HR fit from the lower limit of the data (4 meV) up to 12 meV. The temperature dependence of $A(T)$ obtained in this case is shown in the inset of Fig. 5.7a. The blue shaded area indicates the dependence of $A(T)$ resulting from varying the upper bound of the photon energy range (6 meV – 30 meV) included in the fits. Based on the departure of $A(T)$ from one, we estimate that the metallic response persists down to approximately 60 - 70 K, which is in good agreement with estimates of the onset temperature for the formation of the Kondo groundstate [177]. We note that this onset temperature increases to about 100 K if we include the frequency range up to 30 meV, but in this case the agreement with the measured $\rho_{DC}(T)$ is lost around 150 K.

Before proceeding with further analysis we highlight a few observations that can be gleaned directly from the reflectivity data itself. With decreasing temperature several minima develop in the reflectivity spectra. An isobestic point (i.e. a frequency where the reflectivity is temperature independent) is visible at 0.13 eV. Both above and below this energy, minima start to develop as temperature is lowered. As we will see below, both minima roughly correspond to interband transitions. As temperature decreases below $\sim$ 60 K, a third minimum develops at the lowest measured energies (starting to become visible around 20 meV in the 50 K spectrum).

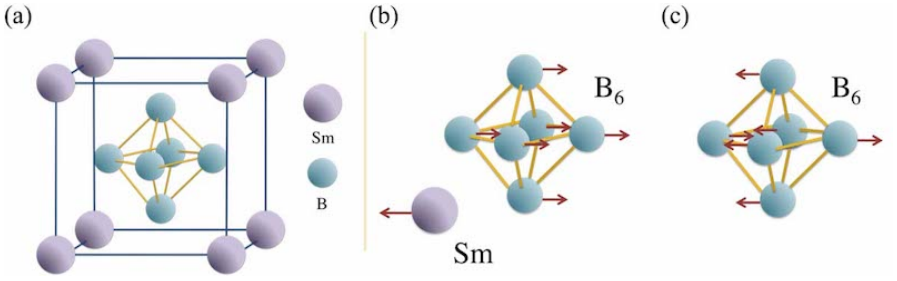

FIGURE 5.8: (a): crystal structure of SmB_6. (b), (c): schematic picture of possible movements of low (high) energy mode.

Another feature that becomes more prominent with decreasing temperature is a peak around 19.4 meV, as shown in the inset of Fig. 5.7b. The crystal structure of SmB_6 is shown in Fig.5.8a, where B_6 octahedra cages are located in the centre of the cubic unit cell with Sm ions placed at each corner. This crystal structure is the same for all rare-earth hexaboride compounds and belongs to the 221 space group [113]. A group theoretical analysis of this structure shows that these compounds have two infrared active modes. One of these modes involves the relative motion of R and B_6 ions, as shown in Fig.5.8b [178–180]. The second mode involves motion of B atoms and corresponds to deformation of the B_6 cage as illustrated in Fig.5.8c. These modes have been observed for some RB_6 compounds (R = Ca, Sr, Eu, La and Yb) [178, 179, 181–187]. The mode involving the movement of the rare-earth ion is found to vary significantly from 13.5 meV (for YbB_6 [178, 186]) to 18.6 meV (for CaB_6 [184, 185]) depending on specific rare-earth ion.

The mode involving B_6 only is found at higher energy at around 105.5 meV for YbB_6 [178, 186] and 108.3 meV for CaB_6 [184, 185] compounds, due to the light weight of the B ions. This mode has thus far not been seen in the IR spectra of SmB_6 [115, 170, 172, 173], attesting to the high quality of our single crystal. A symmetry 'forbidden' excitation was observed in recent Raman experiments [188] with a similar energy as our phonon mode and we suggest that the mode observed in the Raman spectra could thus be interpreted as part of the IR optical phonon branch observed here. We note that the mode becomes more prominent in the reflectivity spectra at low temperature due to 'unscreening'. Specifically, the oscillator strength associated with this mode remains more or less temperature independent, but with decreasing temperature the free charge carrier density is reduced resulting in less effective screening of the mode. Finally, we note a weak but noticeable Fano-like asymmetry for this feature that becomes more prominent as the hybridization gap opens, similar to what has been observed in FeSi [189].

5.5.2 Reflectivity extrapolations

Before turning our attention to the complex optical response functions, we will discuss the method to extract them from the reflectivity data.The complex optical conductivity can be obtained from the reflectivity data using a Kramers-Kronig consistent variational routine [22] (see also Ch. 2). We obtain all relevant optical quantities such as the complex optical conductivity $\sigma(\omega) = \sigma_1(\omega) + i\sigma_2(\omega)$ and dielectric function $\epsilon(\omega) = \epsilon_1(\omega) + i\epsilon_2(\omega)$ from the resulting variational dielectric function model.

The traditional method for obtaining the complex optical conductivity or dielectric function from reflectivity data is to make use of a Kramers-Kronig transformation. In such an approach the phase angle of the complex reflection coefficient is calculated by making use of the Kramers-Kronig relation to the measured reflectivity.

In this case, extrapolations to low (zero) and high (infinite) frequency have to be made beyond the experimental range over which the reflectivity has been measured. Typical expressions for these extrapolations are the Hagen-Rubens approximation as discussed in section 5.5.1 for the low frequency extrapolation and these extrapolations always introduce some uncertainty in the resulting optical quantities. In our analysis we make use of a different approach that has been described in Ref. [22]. When applied to reflectivity data alone, this approach is equivalent to a Kramers-Kronig transformation, but with slightly different extrapolations for low and high frequency.

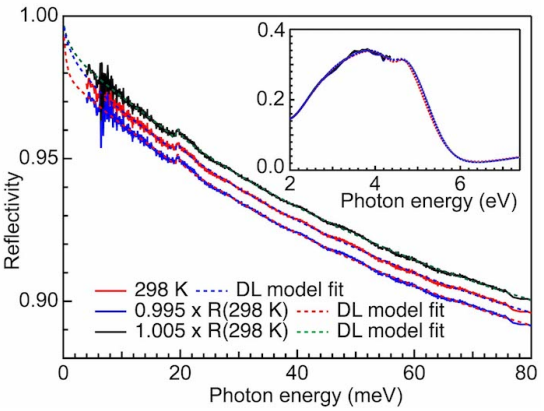

FIGURE 5.9: Room temperature reflectivity data and the fit (red line and blue dashed line respectively) calculated from the Drude-Lorentz model at 298 K. Also shown are the scaled reflectivity data and fits used to make the error bar estimate of the spectral weight transfer (see section 5.5.6). The inset shows the high frequency part of the spectrum and the extrapolation resulting from the Drude-Lorentz model.

The first step in this procedure is to fit the reflectivity spectrum at a given temperature with a Drude-Lorentz model. An example of a fit of the room temperature and the low and high frequency 'extrapolations' are shown in Fig. 5.9. The fitted curve shown is still without the variational function added on top of it. Note that the Drude-Lorentz model already provides a very accurate description of the reflectivity data.

5.5.3 Complex optical response functions of SmB_6

Figure 5.10 presents the real part of the optical constants of SmB_6 over the entire measured frequency range. In panel 5.10a we show the dielectric function $\varepsilon_1(\omega, T)$ and in panel 5.10b the optical conductivity $\sigma_1(\omega, T)$ for the same temperatures as the reflectivity data in Fig. 5.7. At room temperature, the dielectric function resembles that of a typical metal: negative at low energy and, with the exception of a structure around 125 meV, monotonically increasing as a function of energy. We observe a zero crossing around 1.7 eV at all temperatures, corresponding to the screened plasma frequency, $\omega^2_{\mathrm{p,scr}}(T) \equiv \omega^2_{\mathrm{p}}(T)/\varepsilon_\infty$. The inset of panel 5.10a shows that $\omega_{\mathrm{p,scr}}$ decreases with temperature. This decrease is gradual at higher temperatures, but it starts to accelerate below roughly 200 K. We note that at lower temperatures the dielectric function displays several additional zero crossings, which we will discuss further below.

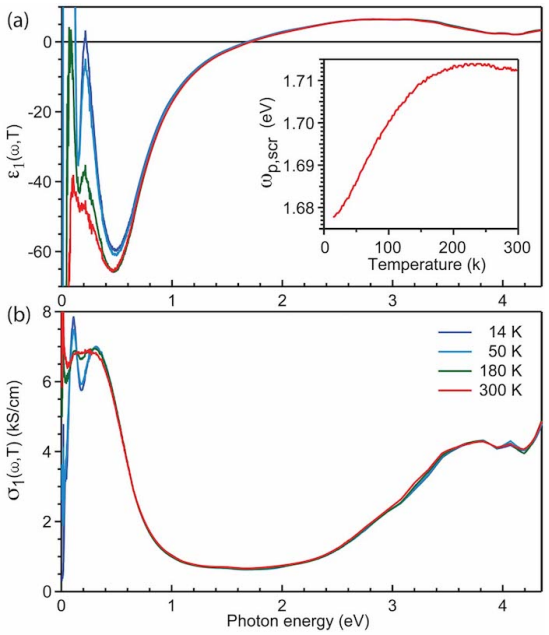

FIGURE 5.10: (a): Dielectric function for selected temperatures (indicated in panel (b)) over the entire frequency range. At room temperature (red) the dielectric function starts out negative, indicative of a free charge response. As temperature decreases interband transitions start to dominate the low energy response. A zero crossing around 1.7 eV, corresponding to a transverse plasma oscillation, is present at all temperatures. The inset shows the temperature dependence of this zero crossing. (b): Optical conductivity at temperatures indicated. The optical conductivity displays several low energy interband transitions as well as weak structures around 2 eV. Above 2 eV a prominent series of interband transitions appear.

At photon energies larger than $\omega_{\mathrm{p,scr}}$, $\varepsilon_1(\omega, T)$ remains positive with structures up until the highest measured frequencies. In this range (3 - 4 eV), the optical conductivity $\sigma_1(\omega, T)$ (Fig. 5.10b) shows a strong interband transition. The origin of this transition is not entirely clear. According to LSDA+U calculations it can have a different interpretation depending on the assumed Sm valence [113]. If a divalent Sm^{2+} configuration is assumed, the transition involves mostly B $2p \rightarrow$ Sm $5d$. Alternatively, it corresponds to a mixture of B $2p \rightarrow$ Sm $5d$ and Sm $5d \rightarrow$ Sm $4f$ transitions in the case of trivalent Sm^{3+}. We further observe two weak structures in the optical conductivity around 1.5 and 2 eV. These transitions are not explicitly described in Ref. [113], but the calculated optical conductivity for the Sm^{3+} configuration *does* show a sharp structure in this range. They seem to originate from

transitions between Sm $5d \rightarrow$ Sm $5d$-$4f_{7/2}$ states and are exclusive to the trivalent Sm^{3+} configuration. Our data therefore support the presence of some Sm^{3+} in the system.

Figure 5.11 presents a more detailed view on $\varepsilon_1(\omega, T)$ and $\sigma_1(\omega, T)$ at low photon energy, which allows for a more careful examination of the temperature dependence in this range. At room temperature the dielectric function in this photon energy range is always negative; however, as temperature is decreased below 180 K, a new zero-crossing appears, labeled $\omega_{p,1}$. If we decrease temperature further, $\varepsilon_1(\omega, T)$ becomes positive over an extended range. Figure 5.11b shows that for temperatures between room temperature and 180 K the main change in the optical conductivity is a reduction in the spectral weight of the Drude peak. We will discuss the detailed evolution of the Drude spectral weight in the next section. Here we would like to point out that the Drude peak has been completely suppressed at 14 K pointing to the formation of a gap in the energy spectrum at the Fermi level. Below 180 K two transitions become more prominently visible in $\sigma_1(\omega, T)$: one around 0.11 eV and another around 0.32 eV, and both increasing in spectral weight as temperature decreases. At much lower temperatures a third transition becomes evident in $\sigma_1(\omega, T)$ around 0.04 eV.

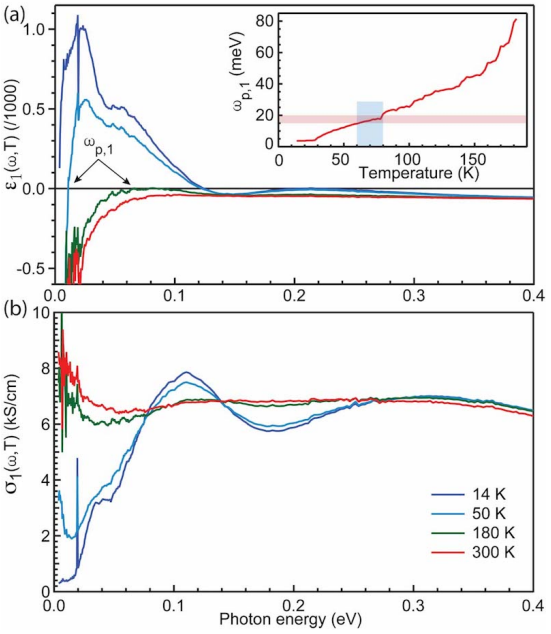

FIGURE 5.11: (a): $\varepsilon_1(\omega, T)$ at selected temperatures (note the rescaling of the vertical axis by a factor of 1000.). At high temperatures $\varepsilon(\omega, T)$ is negative over the entire range shown. At 180 K a new zero crossing, labelled $\omega_{p,1}$, occurs around 80 meV. As the inset shows, $\omega_{p,1}$ shifts to lower energy with decreasing temperature and $\varepsilon_1(\omega, T)$ becomes positive over an extended range of photon energies. The red shaded area indicates the approximate energy of the optical gap edge and the blue area indicates the temperature range where $\omega_{p,1}$ drops below this edge. (b): The corresponding $\sigma_1(\omega, T)$. We observe three distinct interband transitions (40, 120 and 300 meV) at the lowest temperatures. Note also the narrow Drude peak that is still clearly visible at 50 K.

There are several possible origins for these three peaks. The LSDA+U calculations of Ref. [113] again predict several interband transitions in the photon energy range below 1 eV, depending on the Sm valence. However, several aspects of this interpretation should be noted: First, the experimental transition around 0.3 eV seems to stem mostly from occupied, mixed d-$f \rightarrow 5d$-states for the Sm^{2+} configuration, but it may also contain a component related to Sm $5d \rightarrow 4f$ transitions for the Sm^{3+} configuration. Compared to the experimental data reported in Ref. [115], the centre of this transition is somewhat lower in energy in our case. If this

transition indeed has contributions from both Sm^{2+} and Sm^{3+}, this reduction in the centre of the transition could be understood as arising from a different average valence and indicating a larger Sm^{2+} component for our experiments. This hypothesis is further corroborated by the transition that we observe around 0.11 eV. This transition is also present in the experimental data of Refs. [170] and [115], but in those experiments the transition is much weaker relative to the transition at 0.3 eV, whereas in our case it is much more prominent. According to Ref. [113], this transition is between occupied, mixed $d-f$ states and unoccupied Sm $5d$ states that are exclusive to the Sm^{2+} configuration. The second aspect of note is that Antonov *et al.* predict that the lowest lying interband transitions occur around 50 meV and are between various hybridized Sm $5d$ bands exclusive to the Sm^{3+} configuration. This matches well with the structure that we see evolving with temperature just above the optical gap. As might be expected, the lowest energy transitions are most strongly affected as function of temperature as these bands involve transitions directly between hybridizing bands.

We conclude this section with some remarks concerning the appearance of the additional zero-crossings in $\epsilon_1(\omega, T)$ at low temperature, and in particular the low energy crossing labeled $\omega_{\mathrm{p},1}$. As the inset of panel 5.11a shows, this crossing first appears below 180 K and quickly shifts to lower energy with decreasing temperature. It disappears below the lower limit of our experimental range below $T \lesssim 25$ K, but we are still able to infer its approximate energy position from our Drude-Lorentz model. The low temperature value, $\omega_{\mathrm{p},1}(18\ \mathrm{K}) = 3.5$ meV, agrees reasonably well with the zero crossing reported in Gorshunov *et al.* (Ref. [170]). Although the temperature dependence of $\omega_{\mathrm{p},1}$ does not show signs of changes at a particular temperature, a specific temperature scale can be defined as follows. With decreasing temperature the low energy spectral weight starts to decrease and an optical gap begins to form. As Fig. 5.11b shows, the hybridization gap appears to have completely formed around 50 K (based on the appearance of the low energy peak around 0.04 eV). We estimate that the optical gap is approximately 15 to 20 meV wide, based on the 14 K spectrum and using the onset of absorption just below the phonon mode as a measure. In the inset of Fig. 5.11a we indicate the approximate size of the optical gap as the red shaded area and note that the zero crossing in $\varepsilon_1(\omega, T)$ falls below the gap edge at low temperature. The temperature range where this happens is indicated by the blue shaded area and spans the temperature range 60 - 80 K.

5.5.4 Spectral weight transfer

Having identified the main features of the optical response functions, we now turn our attention to the somewhat more subtle changes in their temperature evolution by presenting an analysis of spectral weight transfers associated with the destruction of the

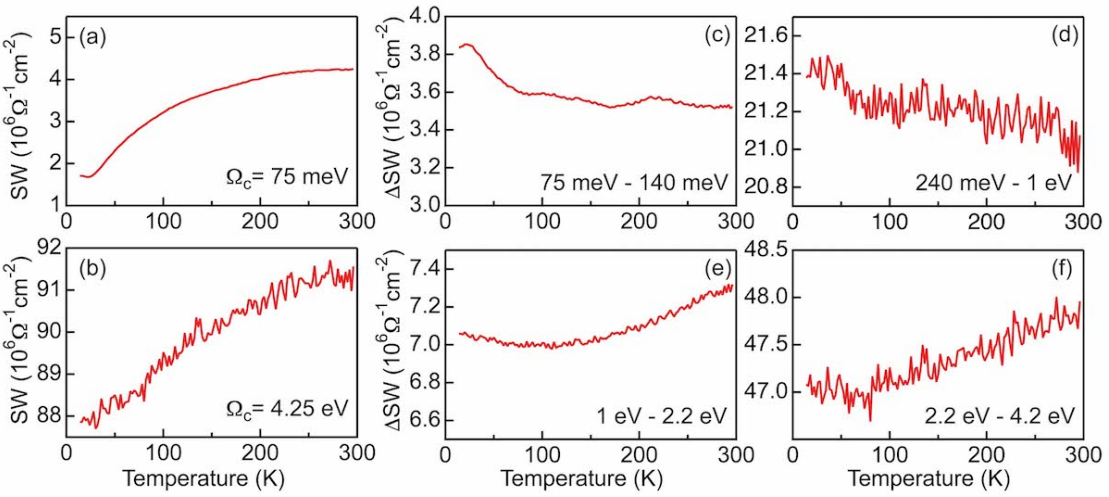

FIGURE 5.12: (a,b): Spectral weight as a function of temperature, integrated up to a cutoff Ω_c indicated in each panel. The spectral weight below 75 meV is lost, which is not recovered in the full measured experimental range. Note that the vertical axes of the two panels are chosen such that the relative change is the same for both ($4.5 \cdot 10^6$ Ω^{-1}cm^{-2}). (c-f): Integrated spectral weight as function of temperature between two cutoffs indicated in each panel. One thing to note is that in each panel a small amount of spectral weight increase occurs below approximately 70 K. Further details are discussed in the text.

metallic state and the formation of the hybridization gap. As temperature decreases the hybridization of the d and f states is expected to result in the formation of an energy gap near (or at) the Fermi level [8]. The formation of this state takes place at the cost of mobile d-electron states in favor of a larger occupation of f-electron states and a reduction of the Drude spectral weight results. This can be quantified by examining the partial integrated spectral weight,

$$\mathrm{SW}(\Omega_c, T) = \int_{\Omega_a}^{\Omega_b} \sigma_1(\omega, T) d\omega.$$

When applied to materials where the optical properties change as function of an external parameter, the integral is often restricted to finite frequency intervals in order to detect associated transfers of spectral weight. The energy range over which these transfers take place can provide information on the interactions involved in the transition [72, 190, 191].

Inspection of Fig. 5.10 and Fig. 5.11, allows us to anticipate approximately the relevant energy ranges. The low energy range is defined by $\Omega_a = 0$ meV and $\Omega_b \approx 75$ meV and the temperature dependence of the SW in this range is shown in Fig. 5.12a. The integrated spectral weight SW(75 meV, T) continuously decreases as the temperature is lowered. Assuming that this depletion can be ascribed entirely to a collapse of the Drude peak, we use $\Delta\mathrm{SW} = \mathrm{SW}(300\ \mathrm{K}) - \mathrm{SW}(14\ \mathrm{K})$ as an estimate of the free carrier density at room temperature. From Fig. 5.12a we obtain $\omega_\mathrm{p} \sim \sqrt{120\Delta\mathrm{SW}/\pi} \approx 9850$ cm^{-1}, which corresponds to $n_\mathrm{free} \approx 1.08 \pm 0.08 \cdot 10^{21}$ cm^{-3} assuming that there is no

mass renormalization (e.g. assuming $m_b \approx 1$ at room temperature). This value is in good agreement with early estimates of the room temperature carrier density [130]. The error bar on this number was determined using the method presented below in section 5.5.6. If we express this in terms of carriers per formula unit, we find that the loss of spectral weight with decreasing temperature corresponds to 0.076 carriers per SmB_6 unit. This reduction is in close agreement with a reduction of the Sm valence observed in temperature dependent x-ray absorption measurements [192], where the estimated average valence of the Sm ions changes from 2.58 at room temperature to 2.5 at low temperature.

One expects that the Drude weight decreases in a simple semiconductor with the chemical potential inside the band gap (or very close to the bottom/top of a band) as a result of changes in the available phase space for scattering and the thermal distribution of free carriers. In SmB_6 at intermediate temperatures the chemical potential sits very close to the hybridization zone between the mobile d band and the localized f-levels, while at low temperature the hybridization gap opens at the Fermi level as evidenced by the optical gap. The loss of spectral weight could therefore result from a similar kinematic effect as that occurring in semiconductors. To exclude this possibility, we calculate in the next section the optical conductivity for a highly simplified tight-binding model for SmB_6.

5.5.5 Spectral weight transfer in a simple tight-binding model.

In order to examine spectral weight transfer as a result of kinematic effects, we considered a simple two-band tight-binding model designed to reproduce the salient features of the SmB_6 optical spectra. The Hamiltonian considered here is:

$$\begin{aligned} H &= \sum_{\mathbf{k},n,\sigma} \epsilon_n(\mathbf{k}) c^\dagger_{n\mathbf{k}\sigma} c_{n\mathbf{k}\sigma} + \sum_{\mathbf{k},n,m,\sigma} t_{nm}(\mathbf{k}) c^\dagger_{n\mathbf{k}\sigma} c_{m\mathbf{k}\sigma} \\ &= \sum_{\mathbf{k},n,m,\sigma} c^\dagger_{n\mathbf{k}\sigma} H_{nm}(\mathbf{k}) c_{m\mathbf{k}\sigma}. \end{aligned} \tag{5.4}$$

Here, $\epsilon_n(\mathbf{k})$ is the band dispersion of the n^{th} band; $c^\dagger_{n\mathbf{k},\sigma}$ ($c_{n\mathbf{k},\sigma}$) is the electron creation (annihilation) operators for the n^{th} band; $t_{nm}(\mathbf{k})$ is the hybridization parameter between n^{th} and m^{th} bands; and σ is the spin of the electron. Our two-band model then consists of a dispersive band $\epsilon_1(\mathbf{k}) = -2t_d[\cos(k_x a) + \cos(k_y a) + \cos(k_z a)] - \mu_0$, and a dispersionless (localized) band $\epsilon_2(\mathbf{k}) = \epsilon_2$. The hybridization parameter between the two bands is momentum independent with $t_{12} = t_{21} = \Delta$. We then set $(t_d,\ \mu_0,\ \Delta) = (0.5,\ -1,\ -0.1)$ eV and ϵ_2 = -15 meV, such that the band structure mimics approximately the band dispersion around the X-point of the Brillouin zone [117]. These bands hybridize with a

hybridization parameter $\Delta = 0.1$ eV, resulting in a direct optical gap of 0.2 eV and an indirect gap of approximately 20 meV.

The optical conductivity $\sigma_{i,j}(\mathbf{q},\omega)$ is evaluated from the Kubo formula, in which the induced electric current density J is approximated to be linear to the external field E as $J_i(\mathbf{q},\omega) = \sum_j \sigma_{i,j}(\mathbf{q},\omega)E_j(\mathbf{q},\omega)$, where i,j are the cartesian directions, $\sigma_{i,j}(\mathbf{q},\omega)$ is the conductivity tensor; and $\mathbf{q}$ and ω are the wavevector and energy of the applied field [193]. For optics, we take the $\sigma_{ij}(\mathbf{q}\to 0,\omega) \equiv \sigma_{ij}(\omega)$ limit. The detailed derivation of $\sigma_{ij}(\omega)$, including multi-band effects, can be found in Ref. [194]. The real part of $\sigma_{ij}(\omega)$ is given by

$$\begin{aligned} \mathrm{Re}[\sigma_{ij}(\omega)] &= \frac{e^2\hbar}{2\pi V}\sum_{\mathbf{k}}\int_{-\infty}^{\infty} dz \frac{n_f(z)-n_f(z+\omega)}{\omega}dz \\ &\times \mathrm{Tr}[A(\mathbf{k},z)\eta_i(\mathbf{k})A(\mathbf{k},z+\omega)\eta_j(\mathbf{k})], \end{aligned} \tag{5.5}$$

where $A_{nm}(\mathbf{k},z)$ is the imaginary part of the electron Greens function $G^{-1}_{nm}(\mathbf{k},z) = (z + i\Gamma)\delta_{nm} - H_{nm}(\mathbf{k})$, $\eta_i(\mathbf{k}) = \frac{1}{\hbar}\frac{\partial}{\partial k_i}H_{nm}(\mathbf{k})$ is the vertex function, $n_f(z)$ is the Fermi-Dirac function, and V is the volume of the crystal. Here, $\Gamma = 2$ meV is a phenomenological broadening introduced by impurity scattering. The dielectric function is related to the conductivity by $\epsilon(\omega) = 1 + 4\pi i\sigma(\omega)/\omega$, where $\sigma(\omega)$ is the complex-valued optical conductivity with the imaginary part obtained from the Kramers-Kronig relations.

The calculated optical spectrum is shown in Fig. 5.13. Figure 5.13a shows the calculated dielectric function at selected temperatures. It captures the main features of the experimental spectrum: at low frequency there is a zero-crossing followed by an interband transition and then two more zero crossings (the zero crossing corresponding to the screened plasma frequency sits outside the calculated window).

The model also captures the main temperature dependencies of the experimental data with the exception of the disappearance of the low frequency zero-crossing ($\omega_{\mathrm{p},1}$ in the inset of Fig. 5.11a). Another difference is the broadening of the interband transitions with increasing temperature. This may be related to the temperature dependence of the scattering rate Γ, which we have neglected here. Figure 5.13a also shows the optical spectrum calculated with an impurity broadening $\Gamma = 30$ meV, providing a better agreement with the data at elevated temperature. Note that the increased broadening does not affect the energy of the zero-crossing.

The calculated optical conductivity is shown in Fig. 5.13b. At high temperatures the results display a clear Drude peak as expected. With decreasing temperature, the Drude peak is gradually suppressed, which is associated with larger occupation of the band bottom. This effect is large enough that the resistivity increases by an order of

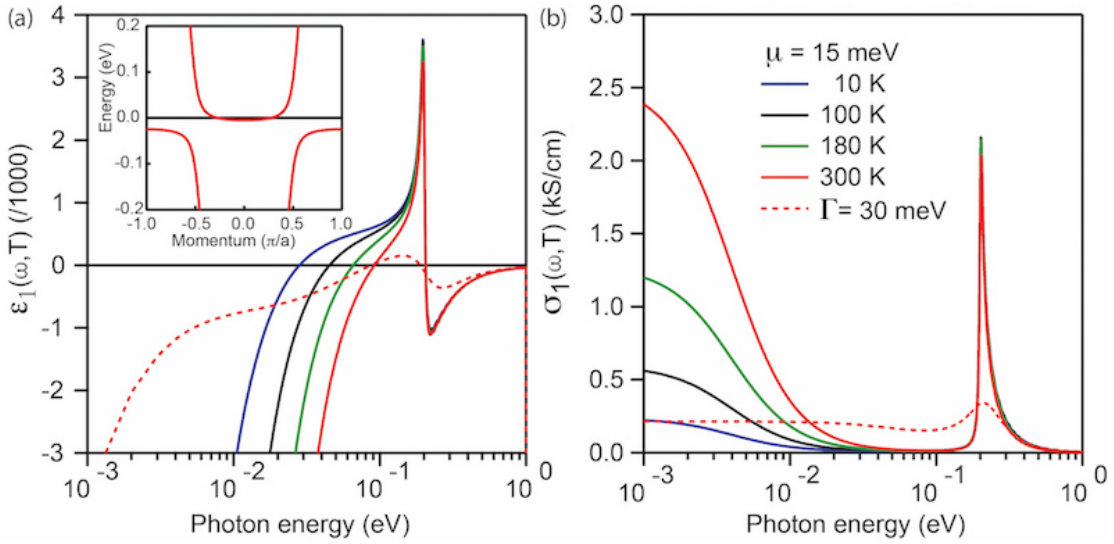

FIGURE 5.13: (a): Calculated real part of the dielectric function at selected temperatures, displaying two zero crossings (one at energy just above 1 eV). The inset shows the hybridized band model used in the calculation, plotted along the $\boldsymbol{k} = (k_x, 0, \pi/2)$ direction. The chemical potential sits 15 meV above the band bottom. (b): optical conductivity showing the reduction of the Drude peak with decreasing temperature. The spectral weight is transferred to the interband transition around 0.2 eV. The dashed curve in both panels shows the 300 K spectrum calculated with a large impurity scattering rate.

magnitude as temperature is reduced. It is obvious that the integrated spectral weight below 0.1 eV is significantly reduced at low temperature. Our calculations show that within the model, this spectral weight is redistributed to higher energies, and most of it is transferred to the interband transition centered at 0.2 eV. However, a few percent of the spectral weight is redistributed over a wider energy range comparable to the full bandwidth of the model.

Applying the same analysis of the spectral weight to the calculated optical conductivity shows that the Drude spectral weight is transferred in the energy range just above the optical gap such that the total spectral weight remains constant. This is not the case for SmB_6 as Fig. 5.12b shows. If we integrate the optical conductivity over the entire range measured, we find that the total integrated spectral weight decreases with about the same amount. This indicates that a significant amount of Drude spectral weight is being redistributed to energies well above $\sim$ 4.35 eV. Moreover, this effect is well beyond what is expected due to simple kinematic effects associated with the opening of the hybridization gap. This situation is somewhat reminiscent of spectral weight transfers taking place in the cuprate high T_c superconductors [72]. In the cuprates spectral weight is transferred from low energy to the scale of the effective Coulomb interaction ($\approx$ 2-3 eV in the cuprates) as the superconducting gap opens. For the case at hand, the on-site $4f$ Coulomb interaction was estimated to be $U_{eff} \approx 7$ eV [113]. This is beyond our experimental window; however, a previous optical experiment by

Kimura *et al.* [169] indeed shows interband transitions around 5 and 10 eV. To solidify this result we should however ensure that the observed transfer is not a result of some experimental error. In the next section we will therefore demonstrate the robustness of these results.

5.5.6 Error estimate of the observed spectral weight transfer

The accurate estimation of the absolute value of the integrated spectral weight is complicated and to some extent depends on choices made in the conversion of the experimental data (e.g. reflectivity) to the complex optical quantities. In chapter 3 and section 5.5.2 we have already discussed the method used to extract the complex optical quantities. The purpose of this section is to show that the main conclusions (i.e. a collapse of the Drude peak and the associated transfer of spectral weight over a large energy range to high energy) are a robust feature that do not depend significantly on the modeling choices made in our analysis. We will show that although the *absolute* value of the spectral weight is very sensitive to the specific model chosen, the *relative* value between different temperatures can be accurately determined.

As a result of the highly detailed temperature dependence used to measure the reflectivity data over a very wide energy range, we can make a reasonable estimate of the error bar on our reflectivity spectrum. Even in the noisiest part of the spectrum (between 4 and 12 meV) the noise is only 0.4 % of the total reflectivity. The systematic error bar on the data (0.2 %) can be estimated from the reproducibility of the many temperature sweeps performed (ranging from 2 cooling-warming cycles in the far infrared to up to 10 cycles in the UV range). To make an estimate of the error introduced in the determination of the spectral weight shifts we therefore follow the following procedure. We scale the reflectivity data up and down by 0.5 % (constant for all temperatures and well beyond the actual error) as shown in Fig. 5.9. We then perform the full analysis to determine the spectral weight based on these scaled datasets.

The results are summarized in Fig. 5.14. As expected, the Drude spectral weight (Fig. 5.14a) slightly increases if the reflectivity data is scaled upwards, while it decreases when the data is scaled downwards. The most important point however is that the *relative* change between room temperature is qualitatively unchanged and quantitatively very similar. The change amounts to an error of about 8 % on the absolute value of the Drude weight. The same holds true if we calculate the integrated spectral weight up to a cutoff frequency $\Omega_c = 4.25$ eV. The error bar on the relative change between low and high temperature is about 3%, but most importantly the total spectral weight decreases irrespective of the shift of the reflectivity data. Comparing panels (a) and (b) of Fig.

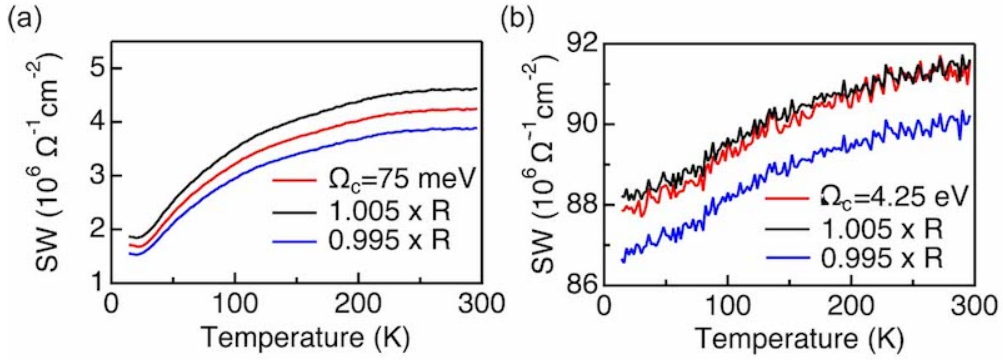

FIGURE 5.14: (a): integrated spectral weight for a cutoff frequency of $\Omega_c = 75$ meV. Shown are SW(T) as presented in Fig. 5.12 and SW(T) obtained when the data is scaled up (black) and down (blue) by 0.5 %. (b): the same as for panel (a), but now with the cutoff frequency $\Omega_c = 4.25$ eV.

5.14, we note that the redistribution of the additional Drude weight does not seem to result in an additional transfer of weight to energies beyond our experimental window. Instead, this weight is already recovered in the interband transition between 3-4 eV.

5.5.7 Concluding remarks and summary

Our spectral weight analysis suggests that the hybridization between d and f states involves energy scales on the order of the effective Coulomb interaction. Surprisingly, almost all of the Drude spectral weight lost in the formation of the Kondo insulating state is transferred to this high energy scale. The stark contrast between the spectral weight redistribution in the experiment and the tight-binding model perhaps serves as an illustration of the idea [8] that the Kondo insulator can be understood as the large U version of a hybridized band insulator. The effective Kondo interaction $J \propto \Delta^2/U$ becomes small in the large U limit. Transfers of spectral weight involving large energy ranges have been observed in several other Kondo insulators [195, 196], which therefore seems a generic feature associated with the formation of the Kondo insulating state. The loss of spectral weight can therefore be seen as a signature of strong electron-electron interactions and the energy scale over which it is recovered as a measure of the effective Coulomb interaction.

The remaining panels of Fig. 5.12 demonstrate that the overall reduction of spectral weight is masking more subtle shifts in spectral weight. For example, the spectral weight of the interband transition around 0.11 eV increases at low temperatures, as is clearly visible in Fig. 5.11b. To estimate if this is the pile-up of spectral weight just above the gap edge anticipated above, we calculate the partial sum rule, $\Delta\mathrm{SW}(T)$, integrated from 75 meV to 140 meV (Fig. 5.12c). Here we observe a different trend in spectral weight

as function of temperature: the spectral weight contained in this transition remains more or less constant as function of temperature down to approximately 60 - 70 K, where the spectral weight suddenly begins to increase. This temperature is close to the temperature where the reflectivity starts to deviate from Hagen-Rubens behavior (see Fig. 5.7a), suggesting that the enhancement of this transition is indeed related to the opening of the hybridization gap. Note, however, the difference in SW scales. The total Drude spectral weight lost is $2.55 \cdot 10^6\ \Omega^{-1}\mathrm{cm}^{-2}$, while the increase of spectral weight around 0.11 eV is of the order of $0.2 \cdot 10^6\ \Omega^{-1}\mathrm{cm}^{-2}$ (panel 5.12c). We find a similar increase in the range between 0.24 eV and 1 eV (panel 5.12d). $\Delta\mathrm{SW}(T)$ between 1 eV and 2.2 eV (Fig. 5.12e) is relatively weak, with a change in slope observed as function of temperature. Finally, panel, 5.12f, shows $\Delta\mathrm{SW}(T)$ in the range between 2.2 and 4.2 eV. The spectral weight in this transition mostly decreases with temperature, but a similar change in slope can be observed around 60 - 70 K, resulting in a small increase of spectral weight of again $0.2 \cdot 10^6\ \Omega^{-1}\mathrm{cm}^{-2}$. To summarize, the total spectral weight decreases, but we observe a small increase in spectral weight in all of the *interband* transitions as the Kondo insulating state forms.

As discussed above, the interband transitions at 0.11 eV and 0.32 eV contain a significant component originating from mixed $d-f \rightarrow 5d$ transitions. The increase in spectral weight below 60 - 70 K can therefore possibly be linked to changes taking place in the hybridization of the d and f states. In recent angle resolved photoemission (ARPES) works the temperature dependence of the $d-f$ hybridization was investigated in detail [161, 162]. It has been observed that one of the f-levels shifts from above (low temperature) to below (high temperature) the Fermi level. The temperature where this state crosses the Fermi level is approximately 60 K, very close to the temperature where we observe changes taking place in (i) the low energy reflectivity and (ii) the temperature dependence of the integrated spectral weight. It is possible that the small feature at 0.04 eV just above the gap edge (see Fig. 5.11b) arises from interband transitions between these occupied and unoccupied mixed $d-f$ states, as the energy matches reasonably well with the splitting observed in Ref. [162]. Comparing to our toy-model calculation, this then implies a hybridization parameter of approximately 20 meV. These authors also notice a second effect: namely a loss of the 'coherency' of the f-states with increasing temperature. This change in coherence (observed as changes in the $4f$ - amplitude and width in the ARPES spectra) is a gradual trend however and not particularly linked to an onset temperature [162]. It is likely that these changes in coherence are reflected in the smearing of spectral features in the optical spectra.

We have investigated the temperature dependent optical properties of SmB_6 in detail.

From the reflectivity data we estimate that the high temperature metallic state is destroyed below 60 - 70 K. A new feature observed in the reflectivity data is a phonon mode with an energy of 19.4 meV, which is related to the T_{1u} mode associated with the rattling of the Sm ion against the boron cages. An analysis of the optical spectra shows that the destruction of the metallic state is a gradual trend, with an approximate onset temperature around 200 K. A comparison of the measured interband transitions and LSDA+U calculations indicates the presence of ions with varying valence in this material. The destruction of the metallic state is accompanied by a loss of low energy (Drude) spectral weight that is not recovered in the experimental range measured. In contrast, a representative tight-binding model calculation shows that this spectral weight should be recovered on an energy scale corresponding to the hybridization strength of the d and f-states. Our analysis suggests that this spectral weight is instead shifted over an energy range involving the effective Coulomb interaction ($U_{\text{eff}} \approx 7$ eV). We suggest that this is a signature of the important role played by strong electron-electron interactions in this material.

Bibliography

[1] Emery, V. J. & Kivelson, S. A. Superconductivity in Bad Metals. *Phys. Rev. Lett.* **74**, 3253 (1995).

[2] Hussey, N. E., Takenaka, K. & Takagi, H. Universality of the Mott–Ioffe–Regel limit in metals. *Philos. Mag.* **84**, 2847 (2004).

[3] Basov, D. N., Averitt, R. D., van der Marel, D., Dressel, M. & Haule, K. Electrodynamics of Correlated Electron Materials. *Rev. Mod. Phys* **83**, 471 (2011).

[4] Dzero, M., Xia, J., Galitski, V. & Coleman, P. Topological Kondo Insulators. *Annu. Rev. Condens. Matter Phys.* **7**, 249 (2016).

[5] Rotter, M., Tegel, M. & Johrendt, D. Superconductivity at 38 K in the Iron Arsenide $(Ba_{1-x}K_x)Fe_2As_2$. *Phys. Rev. Lett.* **101**, 107006 (2008).

[6] van Heumen, E. *et al.* Optical properties of $BaFe_{2-x}Co_xAs_2$. *Europhys. Lett.* **90**, 37005 (2010).

[7] Benfatto, L., Cappelluti, E., Ortenzi, L. & Boeri, L. Extended Drude model and role of interband transitions in the midinfrared spectra of pnictides. *Phys. Rev. B* **83**, 224514 (2011).

[8] Martin, R. M. & Allen, J. W. Theory of mixed valence: Metals or small gap insulators. *J. Appl. Phys.* **50**, 7561 (1979).

[9] Tytarenko, A., Huang, Y., de Visser, A., Johnston, S. & van Heumen, E. Direct observation of a Fermi liquid-like normal state in an iron-pnictide superconductor. *Sci. Rep.* **5**, 12421 (2015).

[10] Tytarenko, A., Nakatsukasa, K., Huang, Y. K., Johnston, S. & van Heumen, E. From bad metal to Kondo insulator: temperature evolution of the optical properties of SmB_6. *New J. Phys* **18**, 123003 (2016).

[11] *VERTEX Series*. Bruker optics, Manual (2013).

[12] Smith, B. C. *Fundamentals of Fourier Transform Infrared Spectroscopy* (CRC Press, Taylor and Francis Group, 2011).

[13] Tkachenko, N. V. *Optical Spectroscopy: Methods and Instrumentations* (Elsevier science publisher, 2006).

[14] http://infrared.phy.bnl.gov/pdf/homes/fir.pdf.

[15] Naylor, D. A. & Tahic, M. K. Apodizing functions for Fourier transform spectroscopy. *J. Opt. Soc. Am. A* **24**, 3644 (2007).

[16] Filler, A. S. Apodization and Interpolation in Fourier-Transform Spectroscopy. *J. Opt. Soc. Am.* **54**, 762 (1964).

[17] Norton, R. H. & Beer, R. New apodizing functions for Fourier spectrometry. *J. Opt. Soc. Am.* **66**, 259 (1976).

[18] Harris, F. J. On the Use of Windows for Harmonic Analysis with the Discrete Fourier Transform. *Proc. IEEE* **66**, 51 (1978).

[19] Blackman, R. B. & Tukey, J. W. *The Measurement of Power Spectra, From the Point of View of Communications Engineering* (Dover, New York, 1959).

[20] Rohsenow, W. M. & Choi, H. *Heat Mass and Momentum Transfer* (Prentice Hal, New York, 1961).

[21] Dressel, M. & Gruner, G. *Electrodynamics of Solids* (Cambridge University Press, 2002).

[22] Kuzmenko, A. B. Kramers–Kronig constrained variational analysis of optical spectra. *Rev. Sci. Instrum.* **76**, 083108 (2005).

[23] http://optics.unige.ch/alexey/reffit.html.

[24] https://www.nobelprize.org/nobel_prizes/physics/laureates/1902/lorentz-lecture.html.

[25] Cini, M. *et al.* (eds.). *Quantum Physics of Light and Matter. A modern introduction to photons, atoms and many-body systems* (Springer International Publishing, 2014).

[26] Cardona, M. *et al.* (eds.). *Electronic structure of strongly correlated materials* (Springer-Verlag Berlin Heidelberg, 2010).

[27] Dreizier, R. M. & Gross, E. K. U. *Density functional theory. An approach to the quantum many-body problem* (Springer-Verlag Berlin Heidelberg, 1990).

[28] Wooten, F. *Optical properties of solids* (Academic press, New York, 1972).

[29] Parker, M. A. *Solid state and quantum theory for optoelectronics* (CRC Press Taylor & Francis Group, 2010).

[30] Berry, M. V. Quantal Phase Factors Accompanying Adiabatic Changes. *Proc. R. Soc. Lond. A* **392**, 45 (1984).

[31] Wilson, K. The renormalization group: Critical phenomena and the Kondo problem. *Rev. Mod. Phys.* **47**, 773 (1975).

[32] Kondo, J. Resistance Minimum in Dilute Magnetic Alloys. *Prog. Theor. Phys.* **32**, 37 (1964).

[33] Klitzing, K., Dorda, G. & Pepper, M. New method for High-Accuracy Determination of the Fine–Structure Constant Based on Quantized Hall Resistance . *Phys. Rev. Lett.* **45**, 494 (1980).

[34] Thouless, D. J., Kohmoto, M., Nightingale, M. P. & den Nijs, M. Quantized Hall Conductance in a Two-Dimensional Periodic Potential. *Phys. Rev. Lett.* **49**, 405 (1982).

[35] Yennie, D. R. Integral quantum Hall effect for nonspecialists. *Rev. Mod. Phys.* **59**, 781 (1987).

[36] Pruisken, A. M. M. Super universality of the quantum Hall effect and the "large N picture" of the θ angle. *Int. J. Theor. Phys.* **48**, 1736 (2009).

[37] Laughlin, R. Quantized Hall conductivity in two dimensions. *Phys. Rev. B* **23**, 5632 (1981).

[38] Haldane, F. D. M. Model for a Quantum Hall Effect without Landau Levels: Condensed-Matter Realization of the "Parity Anomaly". *Phys. Rev. Lett.* **61**, 2015 (1988).

[39] Novoselov, K. S. *et al.* Electric Field Effect in Atomically Thin Carbon Films. *Science* **306**, 666 (2004).

[40] Zhang, Y., Tan, Y.-W., Stormer, H. L. & Kim, P. Experimental observation of the quantum Hall effect and Berry's phase in graphene. *Nature* **438**, 201 (2005).

[41] Kane, C. L. & Mele, E. J. Quantum Spin Hall Effect in Graphene. *Phys. Rev. Lett.* **95**, 226801 (2005).

[42] Kane, C. L. & Mele, E. J. $\mathbb{Z}_2$ Topological Order and the Quantum Spin Hall Effect. *Phys. Rev. Lett.* **95**, 146802 (2005).

[43] Fu, L. & Kane, C. L. Time reversal polarization and a $\mathbb{Z}_2$ adiabatic spin pump. *Phys. Rev. B* **74**, 195312 (2006).

[44] Moore, J. E. & Balents, L. Topological invariants of time-reversal-invariant band structures. *Phys. Rev. B* **75**, 121306 (2007).

[45] Roy, R. Integer Quantum Hall Effect on a Square Lattice with Zero Net Magnetic Field. *arXiv:0603271* (2006).

[46] Fu, L., Kane, C. L. & Mele, E. J. Topological Insulators in Three Dimensions. *Phys. Rev. Lett.* **98**, 106803 (2007).

[47] Fu, L. & Kane, C. L. Topological insulators with inversion symmetry. *Phys. Rev. B* **76**, 045302 (2007).

[48] Bernevig, B. A., Hughes, T. L. & Zhang, S.-C. Quantum Spin Hall Effect and Topological Phase Transition in HgTe Quantum Wells. *Science* **314**, 1757 (2006).

[49] Konig, M. *et al.* Quantum Spin Hall Insulator State in HgTe Quantum Wells. *Science* **318**, 766 (2007).

[50] Hsieh, D. *et al.* A topological Dirac insulator in a quantum spin Hall phase. *Nature* **452**, 970 (2008).

[51] Suzuura, H. & Ando, T. Crossover from Symplectic to Orthogonal Class in a Two-Dimensional Honeycomb Lattice. *Phys. Rev. Lett.* **89**, 266603 (2002).

[52] Hikami, S., Larkin, A. I. & Nagaoka, Y. Spin-Orbit Interaction and Magnetoresistance in the Two Dimensional Random System. *Rep. Prog. Phys* **63**, 707 (1980).

[53] Dzero, M., Sun, K., Galitski, V. & Coleman, P. Topological Kondo Insulators. *Phys. Rev. Lett.* **104**, 106408 (2010).

[54] Frantzeskakis, E. *et al.* Dirac states with knobs on: Interplay of external parameters and the surface electronic properties of three-dimensional topological insulators. *Phys. Rev. B* **91**, 205134 (2015).

[55] Bahramy, M. S. *et al.* Emergent quantum confinement at topological insulator surfaces. *Nature Comm.* **3**, 1159 (2012).

[56] Qi, X., Li, R., Zang, J. & Zhang, S. Inducing a magnetic monopole with topological surface states. *Science* **323**, 1184 (2009).

[57] Peng, H. *et al.* Topological insulator nanostructures for near-infrared transparent flexible electrodes. *Nature Chemistry* **4**, 281 (2012).

[58] McIver, J. W., Hsieh, D., Steinberg, H., Jarillo-Herrero, P. & Gedik, N. Control over topological insulator photocurrents with light polarization. *Nature Nanotech.* **7**, 96 (2012).

[59] Appelbaum, I., Drew, H. D. & Fuhrer, M. S. Proposal for a topological plasmon spin rectifier. *App. Phys. Lett.* **98**, 023103 (2011).

[60] Garate, I. & Franz, M. Inverse Spin-Galvanic Effect in the Interface between a Topological Insulator and a Ferromagnet. *Phys. Rev. Lett.* **104**, 146802 (2010).

[61] Laforge, A. D. *et al.* Optical characterization of Bi_2Se_3 in a magnetic field: Infrared evidence for magnetoelectric coupling in a topological insulator material. *Phys. Rev. B* **81**, 125120 (2010).

[62] Schafgans, A. *et al.* Landau level spectroscopy of surface states in the topological insulator $Bi_{0.91}Sb_{0.09}$ via magneto-optics. *Phys. Rev. B* **85**, 195440 (2012).

[63] Reijnders, A. A. *et al.* Optical evidence of surface state suppression in Bi-based topological insulators. *Phys. Rev. B* **89**, 075138 (2014).

[64] Post, K. W. *et al.* Sum-Rule Constraints on the Surface State Conductance of Topological Insulators. *Phys. Rev. Lett.* **115**, 116804 (2015).

[65] Aguilar, R. V. *et al.* Terahertz Response and Colossal Kerr Rotation from the Surface States of the Topological Insulator Bi_2Se_3. *Phys. Rev. Lett.* **108**, 087403 (2012).

[66] Cava, R. J., Ji, H., Fuccillo, M. K., Gibson, Q. D. & Hor, Y. S. Crystal Structure and Chemistry of Topological Insulators. *J. Mater. Chem. C* **1**, 3176 (2013).

[67] Zhang, Y. *et al.* Crossover of the three-dimensional topological insulator Bi_2Se_3 to the two-dimensional limit. *Nature Physics* **6**, 584 (2010).

[68] Dai, J. *et al.* Restoring pristine Bi_2Se_3 surfaces with an effective Se decapping process. *Nano Research* **8**, 1222 (2015).

[69] Götze, W. & Wölfle, P. Homogeneous Dynamical Conductivity of Simple Metals. *Phys. Rev. B* **6**, 1226 (1972).

[70] R E Glover, I. & Tinkham, M. Transmission of Superconducting Films at Millimeter-Microwave and Far Infrared Frequencies. *Phys. Rev.* **104**, 844 (1956).

[71] Tinkham, M. & Ferrell, R. Determination of the superconducting skin depth from the energy gap and sum rule. *Phys. Rev. Lett.* **2**, 331 (1959).

[72] Molegraaf, H. J. A., Presura, C., van der Marel, D., Kes, P. H. & Li, M. Superconductivity-Induced Transfer of In-Plane Spectral Weight in $Bi_2Sr_2CaCu_2O_{8+\delta}$. *Science* **295**, 2239 (2002).

[73] Van Heumen, E., Lortz, R., Kuzmenko, A. B. & Carbone, F. Optical and thermodynamic properties of the high-temperature superconductor $HgBa_2CuO_{4+\delta}$. *Phys. Rev. B* **75**, 054522 (2007).

[74] Lee, P. A., Nagaosa, N. & Wen, X.-G. Doping a Mott insulator: Physics of high-temperature superconductivity. *Rev. Mod. Phys.* **78**, 17 (2006).

[75] Georges, A., de'Medici, L. & J, M. Strong Correlations from Hund's Coupling. *Annu. Rev. Condens.* **4**, 137 (2013).

[76] Qazilbash, M. M. *et al.* Electronic correlations in the iron pnictides. *Nature Physics* **5**, 647 (2009).

[77] Haule, K. & Kotliar, G. Coherence–incoherence crossover in the normal state of iron oxypnictides and importance of Hund's rule coupling. *New J. Phys.* **11**, 025021 (2009).

[78] Yin, Z. P., Haule, K. & Kotliar, G. Kinetic frustration and the nature of the magnetic and paramagnetic states in iron pnictides and iron chalcogenides. *Nature Materials* **10**, 932 (2011).

[79] de'Medici, L., Giovannetti, G. & Capone, M. Selective Mott Physics as a Key to Iron Superconductors. *Phys. Rev. Lett.* **112**, 177001 (2014).

[80] Werner, P. *et al.* Satellites and large doping and temperature dependence of electronic properties in hole-doped $BaFe_2As_2$. *Nature Physics* **8**, 331 (2012).

[81] Douglass, D. H. (ed.). *p. 17 in Superconductivity in d- and f-Band Metals* (AIP, New York, 1972).

[82] Dolgov, O. & Maksimov, E. Transition temperature of strong-coupling superconductors. *Sov. Phys. Usp.* **25**, 688 (1982).

[83] Bednorz, J. G. & Müller, K. A. Possible high T_c superconductivity in the BaLaCuO system. *Z. Phys. B: Cond. Matt.* **64**, 189 (1986).

[84] Wu, M. K. *et al.* Superconductivity at 93 K in a new mixed-phase Y-Ba-Cu-O compound system at ambient pressure. *Phys. Rev. Lett.* **58**, 908 (1987).

[85] Kamihara, Y., Watanabe, T., Hirano, M. & Hosono, H. Iron-Based Layered Superconductor $La[O_{1-x}F_x]FeAs$ (x= 0.05-0.12) with $T_c = 26$ K. *J. Am. Chem. Soc* **130**, 3296 (2008).

[86] Paglione, J. & Greene, R. L. High-temperature superconductivity in iron-based materials. *Nature Physics* **6**, 645 (2010).

[87] https://esc.fnwi.uva.nl/thesis/centraal/files/f620957118.pdf.

[88] Norman, M. High-temperature superconductivity in the iron pnictides. *Physics* **1**, 21 (2008).

[89] Zaanen, J., Sawatzky, G. & Allen, J. Band-gaps and electronic structure of transition-metal compounds. *Phys. Rev. Lett.* **55**, 418 (1985).

[90] Sawatzky, G., Elfimov, I., van den Brink, J. & Zaanen, J. Heavy-anion solvation of polarity fluctuations in pnictides. *Europhys. Lett.* **86**, 17006 (2009).

[91] Fink, J., Thirupathaiah, S., Ovsyannikov, R. & Dürr, H. Electronic structure studies of $BaFe_2As_2$ by angle-resolved photoemission spectroscopy. *Phys. Rev. B* **79**, 155118 (2009).

[92] Mazin, I. I., Singh, D. J., Johannes, M. D. & Du, M. H. Unconventional Superconductivity with a Sign Reversal in the Order Parameter of $LaFeAsO_{1-x}F_x$. *Phys. Rev. Lett.* **101**, 057003 (2008).

[93] Eschrig, H. & Koepernik, K. Tight-binding models for the iron-based superconductors. *Phys. Rev. B* **80**, 104503 (2009).

[94] Lu, D. H. *et al.* Electronic structure of the iron-based superconductor LaOFeP. *Nature* **455**, 81 (2008).

[95] Massee, F. *et al.* Cleavage surfaces of the $BaFe_{2-x}Co_xAs_2$ and $Fe_ySe_{1-x}Te_x$ superconductors: A combined STM plus LEED study. *Phys. Rev. B* **80**, 140507 (2009).

[96] van Heumen, E. *et al.* Existence, character and origin of surface-related bands in the high temperature iron pnictide superconductor $BaFe_{2-x}Co_xAs_2$. *Phys. Rev. Lett.* **106**, 027002 (2010).

[97] Liu, C. *et al.* Surface-driven electronic structure in LaFeAsO studied by angle-resolved photoemission spectroscopy. *Phys. Rev. B* **82**, 075135 (2010).

[98] Borisenko, S. V. *et al.* Superconductivity without Nesting in LiFeAs. *Phys. Rev. Lett.* **105**, 067002 (2010).

[99] Lankau, A. *et al.* Absence of surface states for LiFeAs investigated using density functional calculations. *Phys. Rev. B* **82**, 184518 (2010).

[100] Allen, P. B. Electron-Phonon Effects in the Infrared Properties of Metals. *Phys. Rev. B* **3**, 305 (1971).

[101] Maslov, D. L. & Chubukov, A. V. First-Matsubara-frequency rule in a Fermi liquid. II. Optical conductivity and comparison to experiment. *Phys. Rev. B* **86**, 155137 (2012).

[102] Berthod, C. *et al.* Non-Drude universal scaling laws for the optical response of local Fermi liquids. *Phys. Rev. B* **87**, 115109 (2013).

[103] Mirzaei, S. I. *et al.* Spectroscopic evidence for Fermi liquid-like energy and temperature dependence of the relaxation rate in the pseudogap phase of the cuprates. *Proc. Natl. Acad. Sci.* **110**, 5774 (2013).

[104] Yang, J., Hwang, J., Timusk, T., Sefat, A. S. & Greedan, J. E. Temperature-dependent optical spectroscopy studies of $Nd_{1-x}TiO_3$. *Phys. Rev. B* **73**, 195125 (2006).

[105] Katsufuji, T. & Tokura, Y. Frequency and temperature dependence of conductivity for perovskite titanates. *Phys. Rev. B* **60**, 7673 (1999).

[106] Nagel, U. *et al.* Optical spectroscopy shows that the normal state of URu_2Si_2 is an anomalous Fermi liquid. *Proc. Natl. Acad. Sci.* **109**, 19161 (2012).

[107] Dressel, M. Quantum criticality in organic conductors? Fermi liquid versus non-Fermi-liquid behaviour. *J. Phys. Condens. Matter* **23**, 293201 (2011).

[108] Stricker, D. *et al.* Optical Response of Sr_2RuO_4 Reveals Universal Fermi-Liquid Scaling and Quasiparticles Beyond Landau Theory. *Phys. Rev. Lett.* **113**, 087404 (2014).

[109] Gofryk, K. *et al.* Effect of annealing on the specific heat of $Ba(Fe_{1-x}Co_x)_2As_2$. *Phys. Rev. B* **83**, 064513 (2011).

[110] Marsik, P. *et al.* Low-energy interband transitions in the infrared response of $Ba(Fe_{1-x}Co_x)_2As_2$. *Phys. Rev. B* **88**, 180508 (2013).

[111] Calderon, M. J., de'Medici, L., Valenzuela, B. & Bascones, E. Correlation, doping, and interband effects on the optical conductivity of iron superconductors. *Phys. Rev. B* **90**, 115128 (2014).

[112] Ning, F. *et al.* ^{59}Co and ^{75}As NMR Investigation of Electron-Doped High T_c Superconductor $BaFe_{1.8}Co_{0.2}As_2$(Tc= 22 K). *J. Phys. Soc. Jpn.* **77**, 103705 (2008).

[113] Antonov, V. N., Harmon, B. N. & Yaresko, A. N. Electronic structure of mixed-valence semiconductors in the LSDA+U approximation. II. SmB_6 and YbB_{12}. *Phys. Rev. B* **66**, 165209 (2002).

[114] Utsumi, Y. *et al.* Bulk and surface electronic properties of SmB_6: a hard x-ray photoelectron spectroscopy study. *arXiv:1705.03459* (2017).

[115] Nanba, T. *et al.* Gap state of SmB_6. *Physica B* **186**, 440 (1993).

[116] Takimoto, T. SmB_6: A Promising Candidate for a Topological Insulator. *J. Phys. Soc. Jpn.* **80**, 123710 (2011).

[117] Lu, F., Zhao, J. Z., Weng, H., Fang, Z. & Dai, X. Correlated Topological Insulators with Mixed Valence. *Phys. Rev. Lett.* **110**, 096401 (2013).

[118] Kim, J. *et al.* Termination-dependent surface in-gap states in a potential mixed-valent topological insulator: SmB_6. *Phys. Rev. B* **90**, 075131 (2014).

[119] Doniach, S. The Kondo lattice and weak antiferromagnetism. *Phys. B* **91**, 231 (1977).

[120] Wachter, P. Intermediate valence and heavy fermions. In *Handbook on the Physics and Chemistry of Rare Earths* (eds. Gschneidner, K. A., Jr, Eyring, L., Lander, G. H. & Choppin, G. R.), vol. 19, 177 (Elsevier Science, Amsterdam, 1994).

[121] Maciejko, J., Qi, X.-l., Karch, A. & Zhang, S.-C. Fractional Topological Insulators in Three Dimensions. *Phys. Rev. Lett.* **105**, 246809 (2010).

[122] Mong, R. S. K., Essin, A. M. & Moore, J. E. Antiferromagnetic topological insulators. *Phys. Rev. B* **81**, 245209 (2010).

[123] Stern, A. Fractional Topological Insulators: A Pedagogical Review. *Annu. Rev. Condens. Matt. Phys.* **7**, 349 (2016).

[124] Pesin, D. & Balents, L. Mott physics and band topology in materials with strong spin–orbit interaction. *Nature Physics* **6**, 376 (2010).

[125] Li, J., Chu, R.-L., Jain, J. K. & Shen, S.-Q. Topological Anderson Insulator. *Phys. Rev. Lett.* **102**, 136806 (2009).

[126] Dzero, M. O. Symplectic large-N theory of topological heavy-fermion semiconductors. *Eur. Phys. J. B* **85**, 297 (2012).

[127] Alexandrov, V., Dzero, M. & Coleman, P. Cubic Topological Kondo Insulators. *Phys. Rev. Lett.* **111**, 226403 (2013).

[128] Menth, A., Buehler, E. & Geballe, T. H. Magnetic and semiconducting properties of SmB_6. *Phys. Rev. Lett.* **22**, 295 (1969).

[129] Paderno, Y. B., Novikov, V. I. & Garf, E. S. Electrical properties of hexaborides of the alkaline - and rare - earth metals at low temperatures. *Sov. Powder Metall. Met. Ceram.* **8**, 921 (1969).

[130] Allen, J. W., Batlogg, B. & Wachter, F. Large low-temperature Hall effect and resistivity in mixed-valent SmB_6. *Phys. Rev. B* **20**, 4807 (1979).

[131] Cooley, J. C., Aronson, M. C., Fisk, Z. & Canfield, P. C. SmB_6: Kondo Insulator or Exotic Metal? *Phys. Rev. Lett.* **74**, 1629 (1995).

[132] Hatnean, M. C., Lees, M. R., Paul, D. M. K. & Balakrishnan, G. Large, high quality single-crystals of the new Topological Kondo Insulator, SmB_6. *Sci. Rep* **3**, 3071 (2013).

[133] Wolgast, S. *et al.* Low-temperature surface conduction in the Kondo insulator SmB_6. *Phys. Rev. B* **88**, 180405 (2013).

[134] Kim, D. J. *et al.* Surface Hall Effect and Nonlocal Transport in SmB_6: Evidence for Surface Conduction. *Sci. Rep* **3**, 3150 (2013).

[135] Zhang, X. *et al.* Hybridization, Inter-Ion Correlation, and Surface States in the Kondo Insulator SmB_6. *Phys. Rev. X* **3**, 011011 (2013).

[136] Rossler, S. *et al.* Hybridization gap and Fano resonance in SmB_6. *Proc. Natl. Acad. Sci. USA* **111**, 4798 (2014).

[137] Tan, B. S. *et al.* Unconventional Fermi surface in an insulating state. *Science* **349**, 287 (2015).

[138] Luo, Y., Chen, H., Dai, J., Xu, Z. & Thompson, J. D. Heavy surface state in a possible topological Kondo insulator: Magnetothermoelectric transport on the (011) plane of SmB_6. *Phys. Rev. B* **91**, 075130 (2015).

[139] Syers, P., Kim, D., Fuhrer, M. S. & Paglione, J. Tuning Bulk and Surface Conduction in the Proposed Topological Kondo Insulator SmB_6. *Phys. Rev. Lett.* **114**, 096601 (2015).

[140] Chen, F. *et al.* Magnetoresistance evidence of a surface state and a field-dependent insulating state in the Kondo insulator SmB_6. *Phys. Rev. B* **91**, 205133 (2015).

[141] Phelan, W. A. *et al.* On the Chemistry and Physical Properties of Flux and Floating Zone Grown SmB_6. *Sci. Rep.* **6**, 20860 (2016).

[142] Gabáni, S. *et al.* Transport properties of variously doped SmB_6. *Philos. Mag.* **96**, 3274 (2016).

[143] Wakeham, N. *et al.* Low-temperature conducting state in two candidate topological Kondo insulators: SmB_6 and $Ce_3Bi_4Pt_3$. *Phys. Rev. B* **94**, 035127 (2016).

[144] Frantzeskakis, E. *et al.* Kondo Hybridization and the Origin of Metallic States at the (001) Surface of SmB_6. *Phys. Rev. X* **3**, 041024 (2013).

[145] Bao, L. H., Tegus, O., Zhang, J. X., Zhang, X. & Huang, Y. K. Large emission current density of $La_xCe_{1-x}B_6$ high quality single crystals grown by floating zone technique. *J. Alloy. Comp.* **558**, 39 (2013).

[146] Shoenberg, D. *Magnetic Oscillations in Metals* (Cambridge Univ. Press, Cambridge, 1984).

[147] Zhu, Z. H. *et al.* Polarity-Driven Surface Metallicity in SmB_6. *Phys. Rev. Lett.* **111**, 216402 (2013).

[148] Ramankutty, S. V. *et al.* Comparative study of rare earth hexaborides using high resolution angle-resolved photoemission. *J. Electron Spectrosc. Relat. Phenom.* **208**, 43 (2016).

[149] Yee, M. M. *et al.* Imaging the Kondo Insulating Gap on SmB_6. *arXiv:1308.1085v2* (2013).

[150] Rossler, S. *et al.* Surface and electronic structure of SmB_6 through scanning tunneling microscopy. *Philos. Mag.* **96**, 3262 (2016).

[151] Xu, N. *et al.* Direct observation of the spin texture in SmB_6 as evidence of the topological Kondo insulator. *Nat. Commun.* **5**, 4566 (2014).

[152] Ruan, W. *et al.* Emergence of a Coherent In-Gap State in the SmB_6 Kondo Insulator Revealed by Scanning Tunneling Spectroscopy. *Phys. Rev. Lett.* **112**, 136401 (2014).

[153] Frantzeskakis, E. *et al.* Insights from angle-resolved photoemission spectroscopy on the metallic states of YbB_6 (001): $E(k)$ dispersion, temporal changes, and spatial variation. *Phys. Rev. B* **90**, 235116 (2014).

[154] Beaurepaire, E., Bulou, H., Scheurer, F. & Kappler, J. P. Magnetism: A Synchrotron Radiation Approach *Lect. Notes Phys.*, vol. 697, chap. Spin-Polarized Photoemission, 94 (Springer, Berlin, 2006).

[155] Chen, Y. L. *et al.* Experimental Realization of a Three-Dimensional Topological Insulator, Bi_2Te_3. *Science* **325**, 178 (2009).

[156] Xia, Y. *et al.* Observation of a large-gap topological-insulator class with a single Dirac cone on the surface. *Nature Physics* **5**, 398 (2009).

[157] Jiang, J. *et al.* Observation of possible topological in-gap surface states in the Kondo insulator SmB_6. *Nature Comm.* **4**, 3010 (2013).

[158] Neupane, M. *et al.* Surface electronic structure of the topological Kondo-insulator candidate correlated electron system SmB_6. *Nature Comm.* **4**, 2991 (2013).

[159] Xu, N. *et al.* Surface and bulk electronic structure of the strongly correlated system SmB_6 and implications for a topological Kondo insulator. *Phys. Rev. B* **88**, 121102 (2013).

[160] Xu, N. *et al.* Exotic Kondo crossover in a wide temperature region in the topological Kondo insulator SmB_6 revealed by high-resolution ARPES. *Phys. Rev. B* **90**, 085148 (2014).

[161] Min, C.-H. *et al.* Importance of Charge Fluctuations for the Topological Phase in SmB_6. *Phys. Rev. Lett.* **112**, 226402 (2014).

[162] Denlinger, J. D. *et al.* Temperature Dependence of Linked Gap and Surface State Evolution in the Mixed Valent Topological Insulator SmB_6 . *arXiv:1312.6637v2* (2013).

[163] Denlinger, J. D. *et al.* SmB_6 Photoemission: Past and Present. *JPS Conf. Proc.* **3**, 017038 (2014).

[164] Hlawenka, P. *et al.* Samarium hexaboride: A trivial surface conductor. *arXiv:1502.01542* (2015).

[165] Li, G. *et al.* Two-dimensional Fermi surfaces in Kondo insulator SmB_6. *Science* **346**, 1208 (2014).

[166] Denlinger, J. D. *et al.* Consistency of Photoemission and Quantum Oscillations for Surface States of SmB_6. *arXiv:1601.07408v1* (2016).

[167] Kierzek-Pecold, E. Plasma Reflection Edge in Crystalline MB_6 Compounds. *Phys. Stat. Sol. (B)* **33**, 523 (1969).

[168] Allen, J. W., Martin, R. M., Batlogg, B. & Wachter, P. Mixed valent SmB_6 and gold-SmS: Metals or insulators? *J. Appl. Phys.* **49**, 2078 (1978).

[169] Kimura, S. I., Nanba, T., Kunii, S. & Kasuya, T. Low-energy optical excitation in rare-earth hexaborides. *Phys. Rev. B* **50**, 1406 (1994).

[170] Gorshunov, B. *et al.* Low-energy electrodynamics of SmB_6. *Phys. Rev. B* **59**, 1808 (1999).

[171] Ohta, H., Tanaka, R., Motokawa, M., Kunii, S. & Kasuya, T. Far-infrared transmission spectra of SmB_6. *J. Phys. Soc. Jpn* **60**, 1361 (1990).

[172] Hudáková, N., Farkašovský, P., Flachbart, K., Paderno, Y. & Shitsevalova, N. Temperature dependence of the infrared properties of SmB_6. *Czech. J. Phys.* **54**, 339 (2004).

[173] Travaglini, G. & Wachter, P. Intermediate-valent SmB_6 and the hybridization model: An optical study. *Phys. Rev. B* **29**, 893 (1984).

[174] Laurita, N. J. *et al.* Anomalous three-dimensional bulk ac conduction within the Kondo gap of SmB_6 single crystals. *Phys. Rev. B* **94**, 165154 (2016).

[175] Jingdi, Z., Yong, J., Takeuchi, I., Greene, R. L. & Averitt, R. D. Ultrafast terahertz spectroscopy study of Kondo insulating thin film SmB_6: evidence for an emergent surface state. *arXiv:1509.04688* (2015).

[176] Wu, L. *et al.* A sudden collapse in the transport lifetime across the topological phase transition in $(Bi_{1-x}In_x)_2Se_3$. *Nature Physics* **9**, 410 (2013).

[177] Caldwell, T. *et al.* High-field suppression of in-gap states in the Kondo insulator SmB_6. *Phys. Rev. B* **75**, 075106 (2007).

[178] Kimura, S.-I., Nanba, T., Kunii, S. & Kasuya, T. Low energy electronic state and optical phonon in YbB_6. *J. Phys. Soc. Jpn.* **61**, 371 (1992).

[179] Gürel, T. & Eryiğit, R. Ab-initio lattice dynamics and thermodynamics of rare-earth hexaborides LaB_6 and CeB_6. *Phys. Rev. B* **82**, 104302 (2010).

[180] Schell, G., Winter, H., Rietschel, H. & Gompf, F. Electronic structure and superconductivity in metal hexaborides. *Phys. Rev. B* **25**, 1589 (1982).

[181] Degiorgi, L., Felder, E., Ott, H. R., Sarrao, J. L. & Fisk, Z. Low-Temperature Anomalies and Ferromagnetism of EuB_6. *Phys. Rev. B* **79**, 5134 (1997).

[182] Perucchi, A. *et al.* Optical Evidence for a Spin-Filter Effect in the Charge Transport of $Eu_{0.6}Ca_{0.4}B_6$. *Phys. Rev. Lett.* **92**, 067401 (2004).

[183] Kim, J.-H. *et al.* Optical spectroscopy study of the electronic structure of $Eu_{1-x}Ca_xB_6$. *Phys. Rev. B* **71**, 075105 (2005).

[184] Vonlanthen, P. *et al.* Electronic transport and thermal and optical properties of $Ca_{1-x}La_xB_6$. *Phys. Rev. B* **62**, 10076 (2000).

[185] Cho, B. K. *et al.* Formation of midgap states and ferromagnetism in semiconducting CaB_6. *Phys. Rev. B* **69**, 113202 (2004).

[186] Werheit, H., Au, T., Schmechel, R., Paderno, Y. B. & Konovalova, E. S. Interband Transitions, IR-Active Phonons, and Plasma Vibrations of Some Metal Hexaborides. *J. Solid State Chem* **154**, 87 (2000).

[187] Ott, H. R. *et al.* Structure and low temperature properties of SrB_6. *Z. Phys. B* **102**, 337 (1997).

[188] Valentine, M. E. *et al.* Breakdown of the Kondo insulating state in SmB_6 by introducing Sm vacancies. *Phys. Rev. B* **94**, 075102 (2016).

[189] Damascelli, A., Schulte, K., van der Marel, D. & Menovsky, A. Infrared spectroscopic study of phonons coupled to charge excitations in FeSi. *Phys. Rev. B* **55**, R4863 (1997).

[190] Katsufuji, T., Okimoto, Y. & Tokura, Y. Spectral Weight Transfer of the Optical Conductivity in Doped Mott Insulators. *Phys. Rev. Lett.* **75**, 3497 (1995).

[191] Rozenberg, M. J., Kotliar, G. & Kajueter, H. Transfer of spectral weight in spectroscopies of correlated electron systems. *Phys. Rev. B* **54**, 8452 (1996).

[192] Mizumaki, M., Tsutsui, S. & Iga, F. Temperature dependence of Sm valence in SmB_6 studied by X-ray absorption spectroscopy. *J. Phys.: Conf. Ser.* **176**, 012034 (2009).

[193] Mahan, G. D. *Many-particle physics* (Plenum Press, New York, 1990).

[194] Atkinson, W. A. & Carbotte, J. P. Effect of proximity coupling of chains and planes on the penetration-depth anisotropy in $YBa_2Cu_3O_7$. *Phys. Rev. B* **52**, 10601 (1995).

[195] Bucher, B., Schlesinger, Z., Canfield, P. C. & Fisk, Z. Kondo Coupling Induced Charge Gap in $Ce_3Bi_4Pt_3$. *Phys. Rev. Lett.* **72**, 522 (1994).

[196] Schlesinger, Z. *et al.* Unconventional charge gap formation in FeSi. *Phys. Rev. Lett.* **71**, 1748 (1993).

Acknowledgement

At the end of my PhD I would like to thank a lot of people who helped me during this four year period. It has been a long and challenging journey, during which I experienced what it means to be part of the international scientific world.

First of all, I would like to thank my supervisor, Erik van Heumen, who gave me the opportunity to come to his lab and introduced me to the scientific community. You are a prime example of an experimental physicist, with a lot of ideas and an enthusiastic attitude towards science. From your example, I learned how to perform clean experiments, be critical, and to strive for perfect results. Your criticism strengthened me a lot, helped me improve myself and developed new skills. Thank you a lot for giving me chance to participate in international conferences and for giving me an opportunity to improve my English by providing a language course. I also learned a lot from you about how to be a good teacher while I was attending your classes of Condensed Matter II. I saw how you kept the attention of the students and made every lecture interesting.

Dear Mark Golden, thank you for your professionalism and support. I will always admire your professional attitude in science and in solving versatile problems. You can find encouraging words for every situation. Countless times you have given me courage for a presentation or a meeting, sometimes with as little as one kind sentence. Dear Anne de Viser, thank you for helping me with the susceptibility measurements in my first year. Also thanks for always being willing to answer my questions, and for the nice conversations during lunchtime. Moreover, I would like to thank, Yingkai Huang for high-quality samples and help with Laue measurements. Also, I would like to acknowledge Huib Luigjes and Hugo Schlatter for their help and advices.

Additionally, I'm thankful to all former and current PhDs who I was lucky to work with. Thank you Artem for meeting me when I just arrived in Amsterdam and helping me a lot to start this journey. Nick, thank you for introducing me to the Dutch culture. My first Kings day and the Dutch festivals we attended were great fun and something I'll always remember. Thanks to Bay and Bo for a good time at the begging of my first year of PhD, I was lucky to try your homemade Chinese and Vietnams dishes. Dear

Emmanouil Frantzeskakis, thank you for explanations and discussions during beamtime at the PSI and very interesting talks. Dear Yu Pan, thank you for being so unusual, your comments over the lunch always made me smile. Dear Shyama, I'm thankful for your valuable support, fun and serious talks. Dear Dona, thank you for encouragement and nice conversations. Dear George, Maarten and Lewis, thank you for interesting discussions and new knowledge about your cultures.

Furthermore, I would like to acknowledge the members of the Technology Centre of the University of Amsterdam: Hans Ellermeijer, Gerrit Hardeman, Johan Mozes, thank you for providing technical and electronic support. Tjeerd Weijers, Daan Giesen and Tijs van Roon thank you for visiting Ukraine, it was fun to have you there. I am thankful for the administrative assistance of the IoP secretariat Rita Vinig, Anne-Marieke Crommentuijn, Natalie Wells and Klaartje Wartenbergh. Also, I would like to express my gratitude to Joost van Mameren for his support and encouragement. Dear Katerina Newell, I appreciate our conversations very much. I hope that some day I can attend your painting exhibition.

Also, I would like to express my gratitude to all committee members for your valuable time that you spent on my thesis.

Additionally, I would like to thank people who I met at the University and who made this journey more colorful. Tijs, your support helped me went through a lot of difficulties, you encouraged me and helped me to remain strong. Noor, I am really happy that you chose our lab to do your bachelor project and that became my close friend. Music festivals would be less fun without you Jans, thanks for a great time. Also, I would like to thank Steef, Xhanta, Rajah and Dominique, it was always a great pleasure to talk to you at the University and it was a really fun time that we spent outside of it. Tim, thanks for fun karaoke parties, where I could pretend that I can sing. Max and Bram thank you for the interesting talks and fun board game nights. Joris, your warm words, and positive energy have always been strengthening and helping me, I am thankful for our valuable discussions and your support.

Also, I would like to thank, Jiu-Jitsu trainers Henk van der Jagt and Edwin Hiense and Jiu-Jitsu crew (above mentioned Nick, Noor, Joris, Xhanta, Dominique, and Tim), the training always helped me to regain some energy during this journey.

Хочу также поблагодарить своих Киевских научных руководителей Романа Михайловича, Андрея Григоровича и Дмитрия Анатолевича. Спасибо, что дали мне возможность приобрести научный опыт в вашей лаборатории, спасибо, что отнеслись с пониманием и поддержали меня в моем решении переехать в другую страну. Коля Исаев, спасибо за то, что обучал меня во время моего прибывания в КНУ и всячески поддерживал.

Так же хочу сказать спасибо русскоязычным ребятам с которыми я познакомилась в Нидерландах: Инна Медведева, Сережа Безрукавников, Давид Давтян, Глеб Полевой, Илья Марков. Спасибо за интересные беседы и веселые вечеринки. Аня Погребная, я искренне рада, что ты приехала на постдок в Нидерланды и добавила красок в мое прибывания тут. Дима Коменский, спасибо за интересные беседы, знакомство с HFML и помощь во время эксперимента. Даша, спасибо, что скрашивала мои 4 года путешествиями в Швейцарию и Францию. Огромное спасибо моим друзьям которые поддержали меня в момент переезда в Нидерланды. Ксюша, Иванка, Андрей, Миля и Катерина спасибо за теплые встречи на родине и за ее пределами.

Хочу высказать огромную благодарность своей семье. Моя любимая мамочка! Спасибо тебе за веру в меня, за бесконечные фотографии со Звездочкой, они всегда поднимают мне настроения. Папочка, спасибо за поддержку и килограммы меда и варенья которые я получала с твоим приездом в Амстердам. Спасибо тебе Леся, за то, что всегда мне помогала. Также хочу выразить свою благодарность брату Вадиму и двоюродной сестре Оле за наши встречи и беседы в Киеве. Моя любимая бабушка, спасибо за теплоту с которой ты меня всегда встречаешь. Дианувка, спасибо тебе за поддержку, за наши путешествия, за коррекцию английского и за то что всегда готова мне помочь.